

# On the Myelination of GABAergic Interneurons



**J. Stedehouder**

# **On the Myelination of GABAergic Interneurons**

J. Stedehouder

---

Copyright © 2019 J. Stedehouder

All rights reserved. No part of this *Thesis* may be reproduced, stored or transmitted in any way or by any means without the prior permission of the author, or when applicable, of the publishers of the scientific papers.

---

---

**On the Myelination of GABAergic Interneurons**

Over de myelinisatie van GABAerge interneuronen

**Thesis**

to obtain the degree of Doctor from the Erasmus University Rotterdam  
by command of the rector magnificus

Prof.dr. R.C.M.E. Engels

and in accordance with the decision of the Doctorate Board.

The public defence shall be held on 23 January 2019 at 15:30 hrs

by

**Jeffrey Stedehouder**

born in Gouda

---

## Doctoral Committee

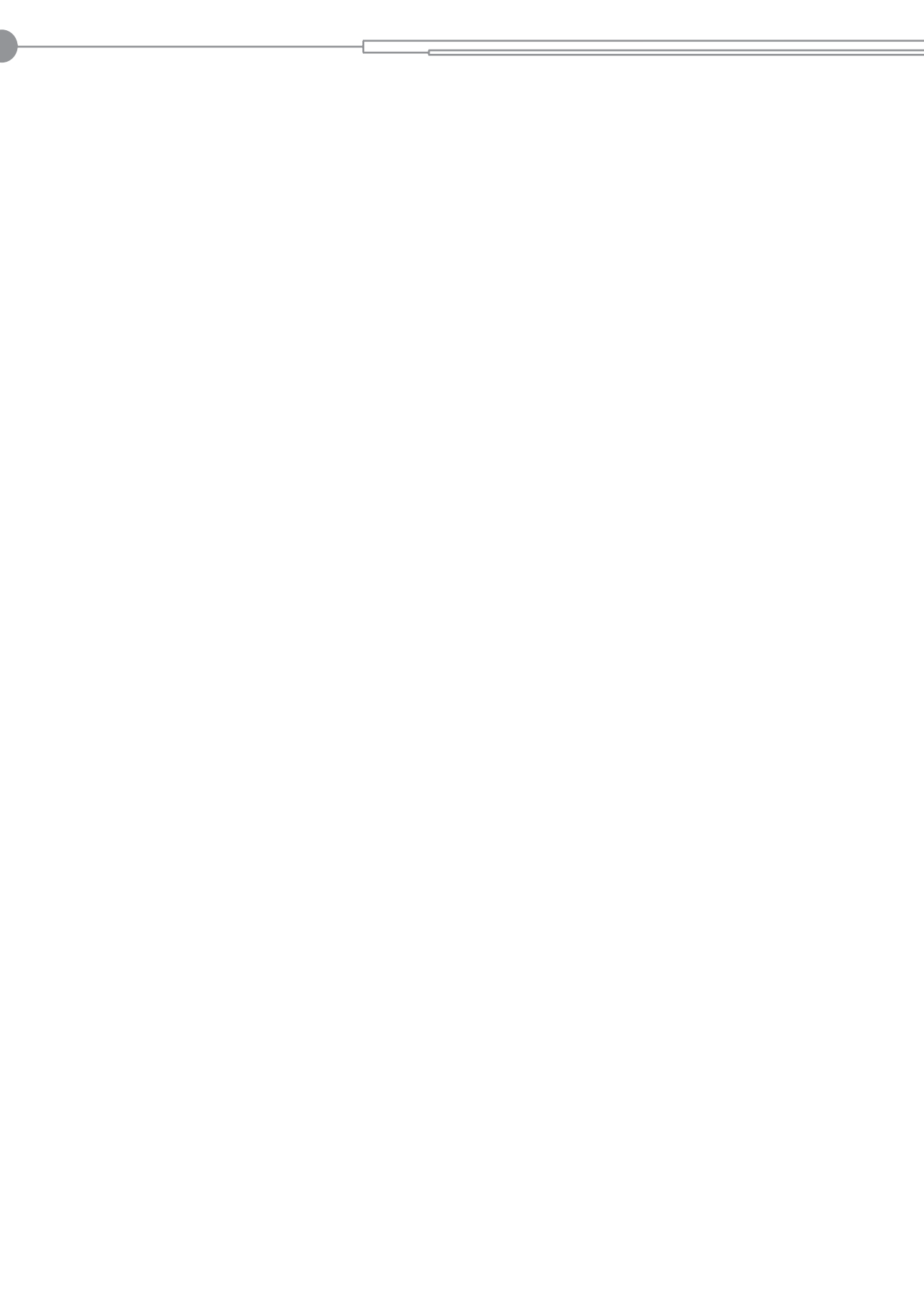
Promotor: Prof.dr. S.A. Kushner

Other Members: Prof.dr. J.G.G. Borst  
Prof.dr. M.H.P. Kole  
Prof.dr. A.B. Houtsmuller

---

---

For my parents



---

---

# Table of Contents

Chapter 1. Introduction	10
Chapter 2. Myelination of parvalbumin interneurons: a parsimonious locus of pathophysiological convergence in schizophrenia	22
Chapter 3. Fast-spiking parvalbumin interneurons are frequently myelinated in the cerebral cortex of mice and humans	38
Chapter 4. Activity-dependent myelination of parvalbumin interneurons mediated by axonal morphological plasticity	74
Chapter 5. Local axon morphology predicts segmental myelination of cortical interneurons	96
Chapter 6. General Discussion	134
References	150
Addenda	168
Summary / Samenvatting	
Curriculum Vitae	
Acknowledgements	
Publications	



# Chapter 1

## Introduction



## Introduction

Science is for everyone, and neuroscience – the study of the brain – is no different. Through the detailed study of our skull's grey mass, through the uncovering of its intricate underlying mechanisms, we can amass more and more interest for this magnificent organ. We can share with the world how truly wonderful this organ really is, which makes us who we are from the moment of conception till shortly after the moment of our death. But as with any organ, our brains can also break, they can become diseased, disordered. And here, too, neuroscience is for the benefit of all. The detailed study of brain disorders can help uncover novel medications or therapies, and improve diagnoses of a whole range of brain problems, from a burn-out to schizophrenia, from stroke to epilepsy.

What follows, is a general introduction of the topics under discussion in the present *Thesis*, an attempt to make digestible for the general public, for all, exactly what is studied, and why it is important that these topics are under investigation in the first place.

## On white matter and myelination

The human brain consists of approximately ~50% white matter, with the remainder being grey matter.<sup>1</sup> While the grey matter contains the neuronal cells, the white matter contains the outgoing connections between the cell bodies, ensuring proper communication between various regions of the brain. Predominantly working on rodent models, we often forget that such a large proportion of the human brain is devoted to mere connections between brain areas. Imagine for a second that only half of a populated urban area consists of houses and companies, and that the remaining half consists of asphalted, 5-lane highways connecting everything! There must surely be a remarkable amount of ongoing traffic in the brain to justify such proportions.

These remarkable numbers aside, the white matter of the brain predominantly consists of myelinated axons. The prototypical brain cell, the neuron, consists of three compartments<sup>2,3</sup>: a soma, dendrites and axons (Fig. 1.1). The soma is the neuronal cell body, which contains the nucleus with all genetic information, our genetic blueprint, as well as other important organelles important for survival of the cell. The dendrites are the receiving extensions, that interpret and forward incoming information originating from other cells in the direction of the soma. Finally, the axons, most important for the present *Thesis*, are the thin outgoing processes through which neurons transmit information to other neurons, or target organs (e.g., muscles). The axons come in a variety of shapes and sizes.<sup>4,5</sup> Analogous to branching patterns of various species of trees, axons can feature only few branches – palm tree – or be widely and intricately branched – oak tree. Similarly, axons can range from a few millimeters in length to as long as ~1 meter or even more. In contrast to their length, axons are remarkably thin, ranging from ~0.1  $\mu\text{m}$  in diameter to several tens of micrometers.

In the brain, signaling speed is a crucially important factor. Proper speed allows us to respond aptly to threats from outside, and evolutionarily could make the difference between life and death. One way to increase the speed of the signal traveling down the axon would be to simply increase the diameter of the axon (e.g. larger drain pipe can transport more water). This is why in general rapidly conducting axons tend to be larger than slowly conducting ones, and why some species have evolved giant diameter axons (as thick as ~1 mm!).<sup>6</sup> Another strategy is to insulate the axon, so reduced amounts of signal are lost leaking through sides of the axon. Indeed, myelination is this insulating ensheathment of axons to ensure higher speed communication.<sup>7,8</sup> The ensheathment itself is termed myelin, after the Greek word for marrow, and consists of up to 160 layers of concentrically wrapped membrane.<sup>9</sup> A nice analogy can be drawn with heating pipes, that maintain their heat better when insulated. Or, in another traffic reference, layers of asphalt upon a road to allow for increased traffic speed. So, whereas unmyelinated axons can be

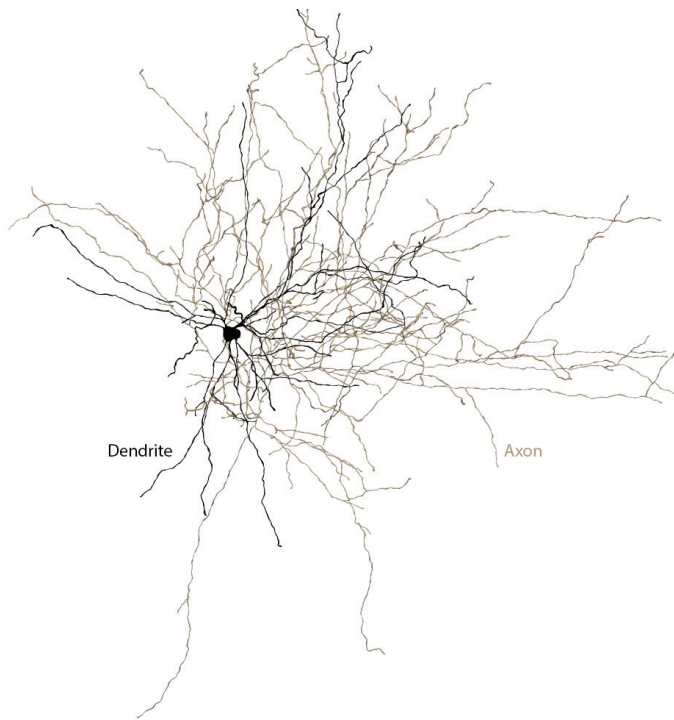


**Figure 1.1.** A neuron. The circular cell body (soma; black), along with its extensions. The dendrites (in black) convey incoming signals, whereas the highly branched axon (brown) will transfer information along to other cells.

imagined as a dusty road on which a horse-wagon could traverse, myelinated axons give rise to asphalted highways for Ferrari-style trafficking. Importantly, an additional advantage of myelination over simply increasing axon diameter is space. Namely, equivalent speeds can be attained by a smaller diameter myelinated axon or a larger diameter unmyelinated axon. Thus, as with many other mechanisms in the brain, the process of myelination results in a continuous trade-off between costs and benefits: In the case of myelin, an efficient trade-off between space occupation and speed increases.

Myelinated segments of axons, also termed internodes, are interrupted occasionally by short domains ( $\sim 1 \mu\text{m}$ ) termed nodes of Ranvier<sup>10</sup>. These nodes are highly excitable, meaning they can continuously and reliably regenerate the signal traveling down the axon, while within myelinated internodes, the signal flows passively along the axon with minimal loss in the outward direction. This peculiar jumping of the signal from node to node is known as “saltatory conduction”.<sup>7,8</sup> Think of these nodal domains as places where you press the car gas pedal in really hard, and then take your foot off the gas again for a few seconds and just let the car roll. In traffic, this would obviously seem very odd. In the brain, this saltatory jumping of signals ensures energy-efficient, highly reliable propagation of signals.

Axons are commonly myelinated, but this is not ubiquitously observed around each and every axon throughout the brain. In white matter, regions dense in axonal fibers, estimates are that ~30% of axons still remain unmyelinated.<sup>11</sup> The exact reasons why some axons in the brain show myelination while others do not remain unknown.<sup>12</sup> Whether or not an axon becomes myelinated is at least in part explained by axonal morphology: In the peripheral nervous system, a clear relation has been shown between axon diameter and myelin status<sup>13</sup>, where axons with a diameter >1  $\mu\text{m}$  show myelination, whereas thinner axons do not. To understand why this could be, a traffic analogy again helps out: It makes no sense to pave small walking paths in a particular forest with asphalt, so people can walk a bit faster. However, the moment a road becomes broad enough for a car, asphalt may start to have an advantage. Whereas in the peripheral nervous system this relationship between axonal morphology and myelin has been well-supported, in the central nervous system, however, this relation is less clear. Here, the diameter threshold lies somewhere between ~0.2  $\mu\text{m}$  and ~0.8  $\mu\text{m}$ <sup>13</sup>. Thus, a more complex interplay likely exists in the brain between axonal morphology, molecular cues, and neuronal activity.

Myelination in the central nervous system is produced by cells known as oligodendrocytes.<sup>14</sup> Although approximately one-third of total cells in cortical grey matter is oligodendrocytes<sup>15</sup>, they constitute approximately ~70% of cells in human white matter regions.<sup>16</sup> The predominant generation of myelin takes place during early postnatal development<sup>16</sup>, but more recent studies have shown that oligodendrocyte formation and *de novo* myelination continues to occur in adulthood.<sup>16-18</sup> This continued maintenance of myelin can be affected by neuronal activity<sup>19,20</sup> and experience<sup>18,21,22</sup> and has given rise to a concept of myelin(ation) plasticity.<sup>23-31</sup> This *de novo* myelination may even be required for learning new motor skills!<sup>32,33</sup> Oligodendrocytes originate from oligodendrocyte precursor cells, a self-renewing cell that constitutes the predominant population of dividing and renewing cells in the adult brain.<sup>34</sup> These cells continuously scout the environment as well as self-repulsed to form a generally homogeneous distribution across the cortex.<sup>35</sup> These facts in themselves are more hints that an optimal upkeep of myelin, by speedy replacement of mature oligodendrocytes, is important for continued functioning of the brain. Here, we could find another nice analogy in the maintenance of highway asphalt, without which serious potholes will arise and traffic can be severely affected.

Besides increasing the speed of communication between distant brain areas, myelination has more recently been suggested to support axonal metabolic demand.<sup>36-38</sup> In particular, oligodendrocytes provide axons – which travel over long distances – with important energy substrates through their myelinated ensheathments.<sup>36-38</sup> Consequently, loss of white matter myelin not only causes decreases in speed with which signals travel, but could actually directly induce axonal death from energy insufficiencies.<sup>36-38</sup> Thus, it is imaginable that through the

mechanism of metabolic support, myelination is actually simply crucial for survival. Indeed, patients suffering from diseases involving severe loss of myelin, for example in the disease known as ‘vanishing white matter disorder’, generally fail to survive beyond several years after disease onset.<sup>322</sup> Although the metabolic function of myelination is drawing increased interest in the field, many questions are still left unanswered.

Thus, myelinated axons constitute a large proportion of our brain volume, which rudimentarily induces speed advantages, but is much more than just speed. In addition, myelination is never done, but continuously updated, continuously changed. Importantly, with myelination playing a key role in the brain, in addition to severe changes in myelin having potentially severe effects, it is becoming more and more appreciated that subtle changes in myelination could actually play a prominent role in more ‘subtle’ diseases of the brain, such as psychiatric disorders.

### **On inhibitory, GABAergic interneurons**

In the brain, a continuous balance exists between the generation and stimulation of signals and putting a break on – inhibiting – these signals, a process generally known as the balance between excitation and inhibition. Only an optimal balance between excitation and inhibition can ensure proper functioning of our brains. Indeed, a disbalance between excitation and inhibition can potentially result in a wide range of neurological problems. On one hand, too much excitation, too much activation without sufficient braking, can lead to epilepsy.<sup>39</sup> On the other hand, too much braking, too much inhibition, without proper activation, can have sedating effects<sup>40</sup> (actually, when the doctor prescribes a regular sleeping pill, it increases these inhibiting effects). Conversely, either too little inhibition or too little excitation, respectively, can result in similar outcomes as too much excitation or too much inhibition!

This balance between inhibition and excitation, braking and speeding up, is carefully and continuously managed in the brain.<sup>41</sup> In the cortex, approximately ~80% of the neurons are excitatory, while the remaining ~20% are inhibitory.<sup>42</sup> These inhibitory cells make use of the neurotransmitter GABA, and thus are often referred to as GABAergic interneurons. Interestingly, these GABAergic inhibitory cells come in various shapes and sizes (Fig. 1.2)<sup>43,44</sup>, and it appears the brain has various ways of sculpting the inhibitory signals to balance out excitatory signals. An analogy can again be drawn with driving a car, where you generally have one single gas pedal, but various ways of braking. There is the foot-operated brake pedal, as well as the hand brake, and if that too fails the car can ultimately brake by making a sudden arboreal (tree-mediated) stop. So intricate is this inhibitory system in the brain, that inhibitory cells exist to inhibit other inhibitory cells!<sup>45</sup> Activation of these particular

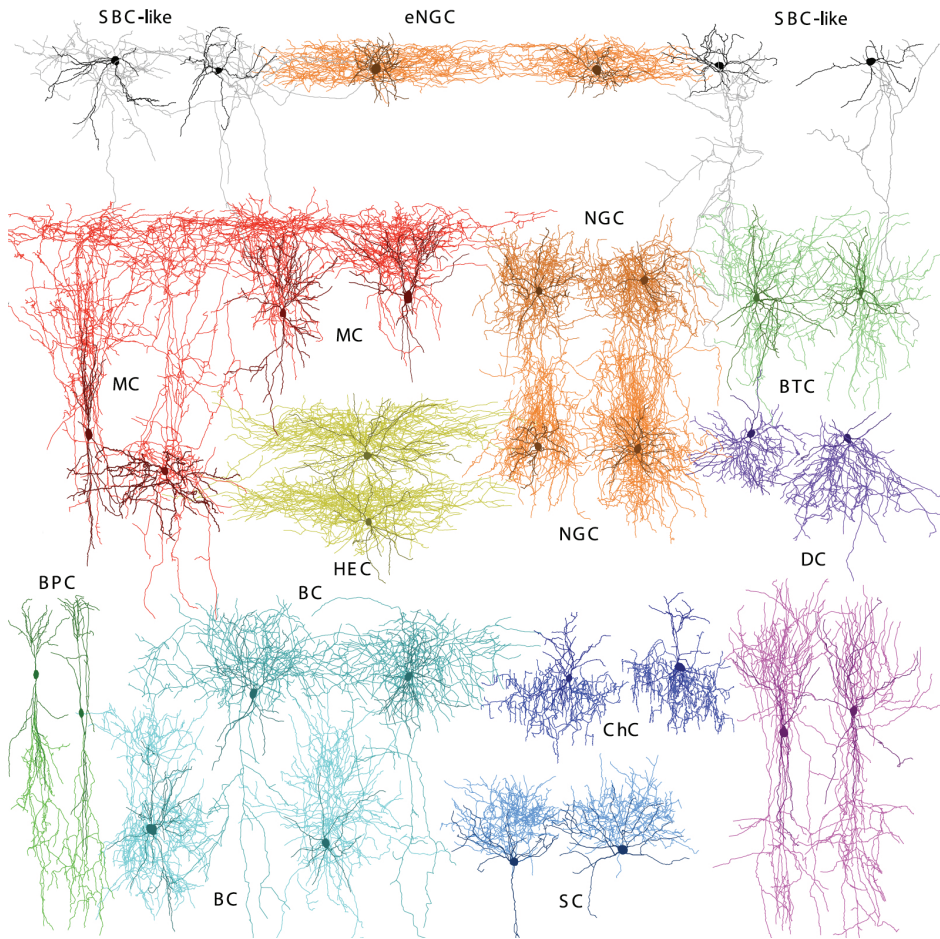


**Figure 1.2.** The colourful plethora of GABAergic interneurons. Each colour represents a different morphological cell type. Soma and dendrites are dark-shaded and axons are light-shaded. Abbreviations: SBC-like small basket-cell-like; eNGC elongated neurogliaform cell; MC Martinotti cell; NGC neurogliaform cell; HEC horizontal elongated cell; BTC bitufted cell; DC deep-projecting cells; BPC bipolar cells; BC basket cells; ChC Chandelier cell; SC shrub cell. Adapted from Jiang *et al.*<sup>43</sup>

cells will reduce the signaling of other inhibitory cells, ultimately causing primary pyramidal cells to signal at higher rates.<sup>45</sup> Imagine someone forcefully holding back your arm when you are trying to pull the hand brake, or forcefully holding back your leg reaching for the brake pedal. Complicated as this may seem, this process is actually thought to play a crucial role in the brain in health<sup>45</sup> and disease.<sup>46</sup>

One of the interneuron subclasses that are of particular interest in this *Thesis* are the fast-spiking, parvalbumin-positive interneurons.<sup>47</sup> These cells account for approximately ~30% of interneurons, making them about ~5-10% of the total population of neurons in the cerebral cortex<sup>48</sup>. The fast-spiking interneurons are

called fast-spiking because they are capable of signaling very rapid series of action potentials. Indeed, under certain behaviors these cells have the capability to signal at 200 Hz - once every 5 milliseconds.<sup>47</sup> In addition, through their direct strong inhibition on cell bodies of primary cells, where action potentials are generated, as well as their large, unbiased connectivity<sup>49</sup>, fast-spiking interneurons are key regulators of neuronal circuits. In other words, activity of a fast-spiking interneuron can inhibit the activity of many surrounding cells. Imagine packed rush-hour traffic where all cars would be controlled by a single person handling a hand brake, at times fully stopping all cars. Provided all cars drive roughly at the same speed, this single-person braking would induce highly synchronous car movements. Now imagine that this single-person braking and subsequent car-autonomous accelerating is happening at intervals of 200 Hz, and we have just modelled the fastest brain waves observable during an electroencephalogram (EEG)! Indeed, fast-spiking interneurons play an important role in synchronizing large groups of cells at higher frequency ranges (~40-200 Hz), known as the gamma range.<sup>50,51</sup>

Altogether, inhibitory interneurons are crucial for brain functioning. They are highly diverse, but nonetheless equally important for optimal network functioning. Analogous to the impairments in myelination/white matter in the brain leading to brain disorders, abnormalities in inhibitory interneurons have been suggested to lead to all sorts of neurological or psychiatric problems.<sup>52-54</sup> I have already mentioned epilepsy above, but more subtle problems in inhibitory cells have been linked to various other disorders of the brain, including, but not limited to, autism spectrum disorders, depression, bipolar disorder and schizophrenia.<sup>52-55</sup> Exactly how GABAergic interneuron dysfunction contributes to each of these diseases, is currently still heavily under investigation.

## **On schizophrenia**

What the brain ultimately does is to try to make sense of the world. Contrary to the notion that the brain simply responds to outside events (stimulus-response)<sup>56</sup>, it is not so much continuously receiving, but it continuously interprets, it continuously predicts.<sup>56,57</sup> The brain creates a reality based on predictions of what may likely happen, and then uses this predicted reality to maneuver our body through the world. Obviously, the ultimate goal of all this is simply to ensure survival of the body, against any means necessary. A particular disease in which this paragon of brain functioning is specifically impaired, is schizophrenia.

Schizophrenia is a major psychiatric disorder that is quite common. The lifetime prevalence lies just under 1%<sup>58</sup>. Following diagnostic guidelines, schizophrenia entails what are known as positive, negative and cognitive symptoms. Positive symptoms, termed as such because they in general cannot be found in the healthy population,

include hallucinations and delusions. Negative symptoms, again termed as such because they tend to exemplify a reduction in functioning compared to healthy individuals, including a wide variety of symptoms ranging from reduced motivation, reduced feelings, and reductions in social interactions. The last group of cognitive symptoms affect working memory, attention, and executive functioning; crucial mental processes quite important for everyday functioning. Together, although each of these symptoms can be present in varying degrees, as well as change over time, a picture emerges of a disease that affects perception of reality, as well as conscious testing of reality.

Schizophrenia is a profound burden for society, which stems from several factors. First, clinical onset of schizophrenia is situated relatively early in life around late adolescence/early adulthood, roughly occurring somewhere between ~18 and 25 years of age.<sup>58</sup> Following onset, schizophrenia generally follows a chronic course. Although severity of symptoms can wax and wane, spontaneous remission – the resolving of all symptoms – only happens rarely. Second, patients suffering from schizophrenia generally have reduced quality of life, higher unemployment levels, and reduced numbers of successful relationships, and well as a higher range of co-morbid problems.<sup>58</sup> Finally, no curative treatment yet exists for this disease, and current treatment options are mainly focused on alleviating the most prominent – positive – symptoms. Together, this combination of early onset, chronic course, and few truly successful treatment options make schizophrenia a significant burden for society.

Although schizophrenia was coined over a century ago<sup>59</sup>, the underlying brain pathology is still unknown. On one hand this is surprising, as schizophrenia is one of the most studied disorders of the brain: A quick search on PubMed for the term ‘schizophrenia’ results in ~135.000 hits (!), a number higher than for Alzheimer’s disease (~100.000), Parkinson’s disease (~84.000), or autism (~45.000). On the other hand, if schizophrenia really evolves around the continuous interpretation and assessment of our individual environments, on questioning what is real and what is not, what is likely to happen and what is not – the apex functions of the human brain – it is not surprising that we still have not figured this disease out. It could be that neuroscientific techniques are currently still insufficient to start unravelling schizophrenia neurobiology. Or, we just have not been looking in the right place.

Nevertheless, what we do know, is that schizophrenia has something to do with dopamine.<sup>60</sup> Dopamine is one of the main neurotransmitters of the brain – a chemical released by neurons to signal to other cells.<sup>61</sup> In popular media, dopamine is often referred to as the ‘happiness hormone’, as activation of dopaminergic cells and release of dopamine is related to rewarding behavior. In schizophrenia, various lines of evidence have shown that overactivation of dopaminergic signaling leads to (at least the positive) symptoms of the disease.<sup>62</sup> First, all known antipsychotics block dopamine signaling at the D2 receptor, and their clinical efficacy is related to

---

their binding to this receptor. Next, dopaminergic agonism can lead to psychotic symptoms in healthy controls, and greatly exacerbates symptoms in patients with schizophrenia. Finally, PET imaging studies have directly shown elevated dopamine signaling in patients. Exactly how aberrant signaling leads to schizophrenia symptoms, is widely debated.<sup>63</sup> Beside dopamine dysfunction, various other pathways have been implicated in schizophrenia pathophysiology<sup>64-66</sup>, but the dopamine system has remained the most widely supported theory. Overall, it appears nature has a particularly cruel sense of irony that such a major debilitating psychiatric disorder can arise from increased signaling of a happiness hormone.

However, it may come to pass, to study schizophrenia, some would say<sup>67</sup>, is to study what makes us human. To study schizophrenia means to study perception, thought, testing of reality, consciousness and awareness, social interaction, motivation. Thus, to study schizophrenia means to study the entirety of what the brain is made for, every cell, every molecule, every brain region. So, if we study schizophrenia, and study it thoroughly, whatever we uncover, will keep advancing our understanding of the brain in a significant manner. This is very much in line with the saying "shoot for the moon, even if you miss, ~~you will still be among the stars~~ *holy shit you're in space.*"

---

## Scope of this Thesis

The present *Thesis* brings the various topics introduced earlier – myelination, inhibitory interneurons, and schizophrenia – together in a single *Thesis*. I will describe how the former two (myelin, interneurons) quite unexpectedly come together in a single phenomenon termed GABAergic interneuron myelination, a phenomenon remarkably understudied, and one that potentially has a key role to play in the pathophysiology of the latter (schizophrenia).

*Chapter 2* describes a review on schizophrenia, where dysfunction in both GABAergic inhibitory interneurons as well as dysfunctional myelination independently have previously been implicated. I combine these findings to put forward the hypothesis that GABAergic interneuron myelination could play a pivotal role in schizophrenia pathophysiology.

*Chapter 3* examines the extent of interneuron myelination in the cerebral cortex of mouse and human. I find that a large proportion of cerebral cortex myelin encompasses GABAergic interneurons and that nearly every PV<sup>+</sup> interneuron shows a proximal pattern of sparse myelination.

*Chapter 4* examines the role of neuronal activity in myelination of PV<sup>+</sup> interneurons. I find that chronic chemogenetic activation in adult prefrontal PV<sup>+</sup> cells leads to more extensive myelination, which appears mediated by changes in axonal branching.

*Chapter 5* examines the role of axonal morphology in governing interneuron myelination. I find that PV<sup>+</sup> interneuron myelination is strongly associated with axonal morphology. Bi-directional axonal manipulations coordinately change myelination, while manipulations of normally unmyelinated SOM<sup>+</sup> interneurons lead to their *de novo* myelination. Across both interneuron subclasses and cell size-varying genetic manipulations, the same set of model parameters retains high predictive validity.

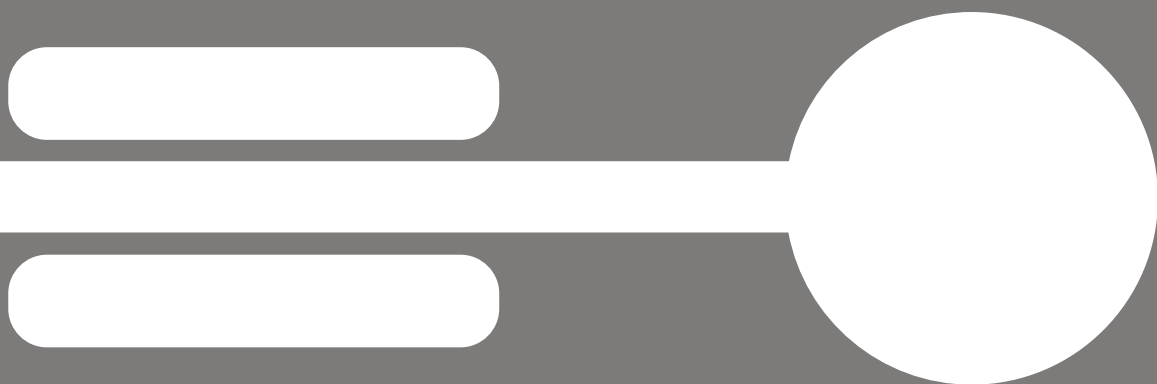


# **Myelination of Parvalbumin Interneurons: A Parsimonious Locus of Pathophysiological Convergence in Schizophrenia**

Jeffrey Stedehouder<sup>1</sup> and Steven A. Kushner<sup>1</sup>

1. Department of Psychiatry, Erasmus MC Rotterdam, The Netherlands

## **Chapter 2**



## Abstract

Schizophrenia is a debilitating psychiatric disorder characterized by positive, negative and cognitive symptoms. Despite more than a century of research, the neurobiological mechanism underlying schizophrenia remains elusive. White matter abnormalities and interneuron dysfunction are the most widely replicated cellular neuropathological alterations in patients with schizophrenia. However, a unifying model incorporating these findings has not yet been established. Here, we propose that myelination of fast-spiking parvalbumin (PV) interneurons could be an important locus of pathophysiological convergence in schizophrenia. Myelination of interneurons has been demonstrated across a wide diversity of brain regions and appears highly specific for the PV+ interneuron subclass. Given the critical influence of fast-spiking PV+ interneurons for mediating oscillations in the gamma frequency range (~30-120 Hz), PV+ myelination is well positioned to optimize action potential fidelity and metabolic homeostasis. We discuss this hypothesis with consideration of data from human postmortem studies, *in vivo* brain imaging and electrophysiology, and molecular genetics, as well as fundamental and translational studies in rodent models. Together, the parvalbumin interneuron myelination hypothesis provides a falsifiable model for guiding future studies of schizophrenia pathophysiology.

## Introduction

Schizophrenia is a chronically debilitating psychiatric disorder with a lifetime prevalence of ~1%.<sup>68</sup> Patients with schizophrenia classically exhibit a constellation of positive, negative, and cognitive symptoms.<sup>64</sup> Although many theories have been proposed, the precise neurobiological mechanism underlying schizophrenia has remained elusive. The most widely described models have been the dopamine<sup>60</sup> and glutamate hypotheses<sup>69</sup>, although in recent years models regarding interneuron dysfunction<sup>70</sup> and myelination abnormalities<sup>71</sup> have gained increasing support.

In this review, we hypothesize that previous observations of interneuron dysfunction and myelination abnormalities in schizophrenia might converge on the altered myelination of fast-spiking parvalbumin-positive (PV) interneurons. First, we summarize the major evidence supporting interneuron dysfunction and myelination abnormalities in schizophrenia. Next, we summarize electron microscopy and immunofluorescence studies that convincingly demonstrate interneuron myelination, which frequently occurs on fast-spiking PV+ interneurons. Finally, we discuss how impairments in myelination of PV+ interneurons could lead to consequent abnormalities in gamma synchronization and ultimately give rise to the symptoms which define schizophrenia.

## Parvalbumin interneuron dysfunction in schizophrenia

Deficits in GABAergic signaling have been widely proposed as a fundamental pathophysiological mechanism underlying schizophrenia.<sup>72</sup> More specifically, several recent lines of evidence from human post mortem studies, genetics, and *in vivo* electrophysiological recordings in patients and translational mouse models have identified fast-spiking PV+ interneurons as the major interneuron cell type affected in schizophrenia (Table 2.1).

Expression of GAD67 – the predominant GABA synthesizing enzyme – has consistently been found to be reduced at both the mRNA and protein levels in several brain regions of patients with schizophrenia, a finding that has been well controlled for confounding factors.<sup>73–79</sup> Downregulation of GAD67 mRNA levels have been reported in ~30% of dorsolateral prefrontal cortex interneurons<sup>80,81</sup> and entirely undetectable in ~50% of PV interneurons.<sup>82</sup> Expression of PV mRNA<sup>83–85</sup> and protein<sup>86</sup> is also reduced in schizophrenia, while the neuronal density of cortical PV+ interneurons is unchanged.<sup>(87–90, but see also 52)</sup> Since the expression of both PV and GAD67 are experience-dependent<sup>91</sup> – and GAD67 and PV expression are highly correlated<sup>91</sup> – their shared downregulation suggests a functional impairment of fast-spiking interneurons.<sup>92</sup> Morphologically, PV+ cell inputs onto pyramidal neurons have no discernible alterations<sup>86</sup>, suggesting a primary functional abnormality of

	<b>Interneuron Dysfunction</b>	<b>Myelination Abnormalities</b>
Schizophrenia Age of Onset	Maturation of PV+ cells <sup>64</sup>	Peak of myelination <sup>126</sup>
	Emergence of high frequency oscillations <sup>98</sup>	Development of frontal grey matter oligodendrocytes <sup>16</sup>
Post Mortem Findings	PV mRNA and protein decreased <sup>82-86</sup>	Abnormal myelin/oligodendrocyte gene expression <sup>127-134</sup>
	GAD67 mRNA and protein decreased <sup>73-82</sup>	Lower oligodendrocyte numbers <sup>136-153</sup>
	Transcriptional changes in PV+ cells <sup>320</sup>	Ultrastructural abnormalities <sup>152-153</sup> Transcriptional changes in oligodendrocytes <sup>138</sup>
Human <i>In Vivo</i> Findings	Activity-dependent EEG abnormalities <sup>70*</sup>	Lower FA values on DTI <sup>108-121*</sup>
	MRS-based GABA impairments <sup>93</sup>	
Genetic Findings	CNVs in GABAergic signaling <sup>99</sup>	GWAS common variants myelin/oligodendrocyte gene sets <sup>155-158</sup>
		GWAS common variants enriched in mature oligodendrocytes <sup>159</sup>

**Table 2.1.** Comparison of interneuron and myelination data for schizophrenia. \*Present in first-episode, drug-naïve patients. Abbreviations: CNV, copy number variation; DTI, diffusion tensor imaging; EEG, electroencephalography; FA, fractional anisotropy; GABA, gammaaminobutyric acid; GWAS, genome-wide association study; mRNA, messenger RNA; MRS, magnetic resonance spectroscopy; PV, parvalbumin.

PV+ interneurons. Consistent with these neuropathological findings, *in vivo* PET imaging has demonstrated widespread alterations of cortical GABA transmission in schizophrenia, a finding that was most prominent in the subset of patients who were antipsychotic-naïve.<sup>93</sup> Together, these results provide compelling evidence of cortical PV+ interneuron dysfunction in schizophrenia.

PV+ interneurons are essential in generating cortical oscillations in the gamma range (~30-120 Hz), mediated by synchronized inhibition of large pyramidal cell ensembles.<sup>50,51</sup> Through rhythmic perisomatic inhibition onto surrounding pyramidal cells, synchronous ensembles of PV+ cells evoke high-frequency gamma oscillations in the cerebral cortex.<sup>94-96</sup> Gamma synchrony has been shown to function critically across a range of cognitive functions, including working memory and attention<sup>97</sup>, with well-replicated abnormalities in schizophrenia.<sup>35,5</sup> Abnormalities in other frequency bands such as theta and alpha have also been reported in schizophrenia, but the neural mechanisms underlying these frequencies remain less well understood.<sup>35</sup>

Electroencephalographic (EEG) studies in schizophrenia have shown a reduced amplitude and impaired phase locking of gamma band activity over frontal areas while assessing working memory and executive functioning tasks.<sup>35</sup> Although some

studies have observed concurrent increases in gamma band activity at rest, this finding has been less well replicated.<sup>35</sup> Taken together, impairments of *in vivo* gamma oscillations in patients with schizophrenia are highly consistent with the PV+ interneuron abnormalities observed by postmortem histopathology.

The classical onset of schizophrenia occurs within a relatively narrow window of neurodevelopment, between approximately 18 and 25 years of age.<sup>64</sup> This late adolescent age of onset has often been attributed to the ongoing functional maturation of the brain during this neurodevelopmental critical period.<sup>64</sup> Specifically in late adolescence, rates of synaptic pruning and myelination become asymptotic for which impairments in these processes have been linked to the disease onset.<sup>64</sup> Notably, maturation of gamma band synchrony also occurs during late adolescence<sup>98</sup> which coincides developmentally with the clinical onset of schizophrenia.

In addition to *in vivo* brain imaging, EEG recordings, and postmortem histopathology, molecular genetic studies of schizophrenia have also revealed an important contribution of interneuron dysfunction to the pathophysiology of schizophrenia. A recent genetic study of copy number variation (CNV) has now provided causal evidence for GABAergic dysfunction in the etiology of schizophrenia.<sup>99</sup> In this study, Pocklington *et al.* (2015) performed a functional gene set analysis for enriched biological mechanisms using the largest schizophrenia case-control CNV dataset thus far reported and found that case CNVs were significantly enriched for genes responsible for inhibitory neurotransmission (in particular the GABA<sub>A</sub> receptor complex), glutamatergic neurotransmission, long-term synaptic plasticity, and associative learning. The genetic variant with the highest known risk for schizophrenia is the 22q11 microdeletion which has a penetrance of ~40% penetrance<sup>100,101</sup>. Transgenic mouse models have been generated to investigate the underlying neurobiology conferred by 22q11 microdeletion. Df(16)A mice harboring a 27-gene microdeletion syntenic to a 1.5 Mb region of human 22q11.2 exhibit similar brain abnormalities as found in human 22q11 microdeletion carriers, including cortico-cerebellar, cortico-striatal and cortico-limbic circuits.<sup>102</sup> Moreover, multiple different mouse models of 22q11 microdeletion have replicated a cell-type specific impairment in PV+ interneurons and disrupted local synchrony of neural activity, consistent with the deficit in gamma oscillations observed in schizophrenia.<sup>103–105</sup>

Evidence for interneuron dysfunction in schizophrenia has also been supported by a wide variety of non-genetic rodent models.<sup>106</sup> The major examples include pharmacological NMDA receptor antagonism and neurodevelopmental immunological challenge, both of which consistently exhibit synaptic and network abnormalities reminiscent of schizophrenia pathophysiology. Specifically, these studies have identified electrophysiological changes in local microcircuit connectivity and synaptic plasticity, with alterations in excitation/inhibition balance and gamma band synchronization.

Taken together, the combination of genetic, post mortem, and *in vivo* electrophysiological and functional imaging results from human clinical studies of schizophrenia converge with translational rodent modeling to identify fast-spiking PV+ interneuron dysfunction as a major pathophysiological mechanism underlying schizophrenia etiology.

## **Myelination abnormalities in schizophrenia**

Independent of PV+ interneuron alterations, myelination abnormalities have also been extensively implicated in schizophrenia through both *IN VIVO* brain imaging and postmortem assessments (Table 2.1). Numerous diffusion tensor imaging (DTI) studies have been published for schizophrenia (reviewed in <sup>71</sup>), of which the overwhelming consensus has been the association of schizophrenia with globally decreased fractional anisotropy (FA). Notably, the decrease in FA appears to become more severe with increasing age and illness duration.<sup>107</sup> Many of the early brain imaging studies of schizophrenia were performed in cohorts with extensive histories of psychotropic medication, inpatient hospitalization, smoking, and medical comorbidities, which could have a confounding deleterious influence on white matter integrity. Thus, an important question has been whether myelination abnormalities are already present in drug-naïve patients with first-episode schizophrenia who have never received psychotropic medication. Recently, several DTI studies have been performed in such cohorts,<sup>108–121</sup> holding the potential to directly evaluate these potential confounders. Indeed, across a range of different methodologies, studies of drug-naïve first-episode schizophrenia have consistently demonstrated similar, albeit less severe, myelination abnormalities as observed in chronic illness. Importantly, these studies confirm that a global impairment of myelin integrity is already present at the time of the initial clinical onset of psychotic symptoms in schizophrenia. Accordingly, these findings support a model by which myelination abnormalities function critically in the pathophysiology of schizophrenia.

The late adolescent age of onset for schizophrenia closely overlaps with the maturation of prefrontal cortex myelination.<sup>122</sup> The time course of myelination in humans has been elegantly detailed through longitudinal *in vivo* imaging and postmortem cross-sectional studies demonstrating rapid early postnatal white matter development in the first 12 months<sup>123</sup>, followed by a slower but steady increase until late adolescence.<sup>124,125</sup> Comparative mammalian evolutionary studies have demonstrated that humans exhibit a particularly extended neurodevelopmental time course of neocortical myelination.<sup>126</sup> While myelination in humans peaks in late adolescence, for non-human primates and rodents the peak of myelination occurs significantly earlier in development.<sup>126</sup> Together, the current best evidence demonstrates that the onset of schizophrenia closely coincides with the peak of myelination in human brain development.

In addition to the well-replicated finding of *in vivo* white matter abnormalities in schizophrenia, postmortem gene expression analyses have also identified alterations in myelination regulatory pathways. Several studies have reported a broad reduction in the expression of genes with demonstrated function in the oligodendrocyte lineage.<sup>127–134</sup> Using microarray-based transcriptome analysis with qPCR validation, abnormalities in oligodendrocyte lineage genes have been found in both frontal white and grey matter<sup>127,128,131</sup>, subcortical regions<sup>129,132</sup>, occipital cortex<sup>133</sup>, and temporal cortex<sup>134</sup>. The alignment between *in vivo* brain imaging findings and postmortem gene expression analyses is highly consistent with the central importance of myelination abnormalities in schizophrenia pathophysiology. Notably, many of the same oligodendrocyte and myelination genes found to be altered in schizophrenia also exhibit consistent increases during normal brain development precisely during adolescence,<sup>135</sup> again consistent with the association between the late adolescent age of onset in schizophrenia and the peak of myelination.

Compared to the abundance of brain imaging and gene expression studies of myelination and oligodendrocytes, post mortem stereological analysis of oligodendrocyte lineage cell types are scarce. From the few studies that have been performed, stereological quantification of myelinating oligodendrocytes have revealed widespread reductions in schizophrenia (Table 2.1).<sup>136–146</sup> Reductions in oligodendrocyte numbers have been shown in the white and grey matter of BA9,<sup>136–140</sup> white and grey matter of BA10,<sup>141,142</sup> posterior hippocampal subregion CA4,<sup>143</sup> internal capsule,<sup>144</sup> nucleus basalis,<sup>145</sup> and anterior thalamic nucleus<sup>146</sup>. In contrast, oligodendrocyte numbers appear unchanged within the substantia nigra,<sup>147</sup> callosal genu,<sup>148</sup> and subgenual cingulum.<sup>148</sup> Furthermore, one study failed to find differences in oligodendrocyte number within any subregion of the hippocampus.<sup>149</sup> In addition, a few studies have reported seemingly paradoxical increases in the number of myelinating oligodendrocytes in frontal white matter<sup>150</sup> and basolateral amygdala.<sup>151</sup> Although caution is warranted given the limited number of studies and differences in methodology, the emerging picture is one of small but consistent reductions of myelinating oligodendrocytes in schizophrenia (~14% reduction<sup>136,137,139–146</sup>). However, an important unanswered question is whether the observed reduction of myelinating oligodendrocytes is cell-type specific or also extends to other less differentiated cell types within the oligodendrocyte lineage.

A very recent study is the first to report a stereological analysis of oligodendrocyte precursors cells (OPCs)<sup>138</sup>, also known as NG2 cells due to their high expression of the neuron-glia antigen 2 (NG2) protein. The number of frontal white matter OPCs were unchanged while the total population of oligodendrocyte lineage cells was reduced, thereby suggesting that the reduction in oligodendrocyte lineage cells occurs predominantly in more differentiated cell types. Furthermore, oligodendrocyte cell type-specific transcriptome analysis and immunohistochemical labeling independently suggests an impairment of OPC differentiation towards

mature oligodendrocytes. Given that OPCs are the exclusive progenitor cell population of myelinating oligodendrocytes, more knowledge of the regulation and function of OPCs in schizophrenia would better clarify whether the observed reductions in myelinating oligodendrocytes are a consequence of abnormalities that have occurred upstream in the myelination lineage or the consequence of a cell-type specific loss of myelinating oligodendrocytes.

Two studies have examined myelination at the ultrastructural level in schizophrenia. The major findings involved myelinated axons and oligodendrocytes, in frontal cortex white and grey matter.<sup>152,153</sup> The observed pathological features included alterations in the morphology of the myelin sheath and the frequency of axonal degeneration within morphologically-intact myelin segments. Notably, the effect sizes were larger in grey matter compared to white matter regions.<sup>152,153</sup> With regard to *in vivo* and postmortem findings, the possibility remains that the observed myelination abnormalities in schizophrenia could result from primary and/or secondary disturbances of neuronal signaling.<sup>154</sup> Therefore, genetic studies provide a unique opportunity to investigate etiological mechanisms of schizophrenia while avoiding the potential confounds of antipsychotic medication and secondary disease effects. Notably, recent studies have shown using genome-wide association study (GWAS) data that myelination/oligodendrocyte genes sets are significantly associated with both the risk of schizophrenia<sup>155–157</sup> and the severity of deficits in white matter integrity.<sup>158</sup> Moreover, the most recent GWAS results for schizophrenia exhibited a significant enrichment of genes expressed in mature oligodendrocytes,<sup>159</sup> together suggesting a convergence of common variant risk on myelination.

Although important questions remain unanswered, GWAS results implicating myelination as an etiological mechanism, *in vivo* imaging demonstrating well-replicated myelination abnormalities, human postmortem histopathology showing replicated decreases in the number and ultrastructure of oligodendrocytes, and gene profiling studies demonstrating replicated changes in oligodendrocyte expression, together provide compelling support for myelination as a major pathophysiological mechanism in schizophrenia.

## **Myelination of parvalbumin interneurons**

An increasing number of studies has revealed the unexpectedly extensive myelination of interneurons (Table 2.2), predominantly fast-spiking PV+ basket cells, in cortical grey matter and other regions throughout the brain<sup>160–186</sup> (Table 2.3). Myelination of cortical GABAergic basket cells was first reported over 30 years ago in the cat visual cortex by electron microscopy.<sup>161,172,180</sup> In non-human primates, GABAergic axons in layers III-V are myelinated in sensorimotor<sup>162,163,186</sup> and temporal<sup>182</sup> cortices, a finding that had already been hinted at several years

Study	Species	Region	Technique	Conclusion
Somogyi <i>et al.</i> <sup>180</sup>	Cat	Visual Cortex	EM	Presence of single myelinated GAD+ cells
Mize <i>et al.</i> <sup>174</sup>	Cat	Superior Colliculus	EM	Presence of myelinated GABAergic neurons
Ong <i>et al.</i> <sup>182</sup>	Human	Frontal cortex	EM	Presence of several myelinated GAT-I axons
Ong <i>et al.</i> <sup>182</sup>	Monkey	Temporal cortex	EM	Presence of several myelinated GAT-I axons
Hendry <i>et al.</i> <sup>106</sup>	Monkey	Sensorymotor cortex	EM	Presence of several myelinated layer III–V GABAergic neurons
DeFelipe <i>et al.</i> <sup>107</sup>	Monkey	Somatosensory cortex	EM; [3H] GABA tracing	Presence of several myelinated GABAergic neurons
DeFelipe <i>et al.</i> <sup>108</sup>	Monkey	Sensorymotor cortex	EM	Presence of several myelinated layer III–V GABAergic neurons
Takasu <i>et al.</i> <sup>109</sup>	Monkey	Hypoglossal nucleus	EM	Presence of several myelinated GABAergic neurons
Ralston <i>et al.</i> <sup>110</sup>	Monkey	Red nucleus	EM	Presence of several myelinated GABAergic neurons
Jinno <i>et al.</i> <sup>111</sup>	Rat	Hippocampus	SCT; IF	Presence of several myelinated GABAergic projection neurons
De Biasi <i>et al.</i> <sup>113</sup>	Rat	Thalamus	EM	Presence of a few myelinated GABAergic axons
Conti <i>et al.</i> <sup>114</sup>	Rat	Cortex	EM	Presence of several myelinated GAT-2 positive axons
Roberts <i>et al.</i> <sup>121</sup>	Rat	Inferior colliculus	EM	Presence of several myelinated GABAergic neurons
Sawyer <i>et al.</i> <sup>120</sup>	Monkey	Thalamus	EM; LM	Presence of several myelinated GABAergic neurons

**Table 2.2.** Studies reporting myelination of GABAergic neurons. Abbreviations: EM, electron microscopy; GABA, gamma-aminobutyric acid; GAD, glutamic acid decarboxylase; GAT, GABA transporter; IF, immunofluorescence; LM, light microscopy; SCT, single-cell tracing.

earlier.<sup>185</sup> Myelinated GABAergic interneurons were subsequently identified in the cat superior colliculus<sup>174</sup>, as well as in the red nucleus<sup>165</sup> and hypoglossal nucleus<sup>164</sup> of the monkey. Although the relative distribution of myelination across interneuron subtypes has not yet been quantitatively determined, a consistent qualitative observation has been that a high proportion of the GABA-labeled terminals of myelinated axons exhibit localized somatic targeting suggestive of basket cells.<sup>106</sup> Moreover, direct ultrastructural evidence for basket cell myelination has also been demonstrated in visual cortex of cat<sup>98,99</sup> and rat<sup>112</sup>.

PV-positive myelinated fibers in the adolescent mouse visual cortex were reported to be abundantly present by fluorescence confocal microscopy.<sup>160</sup> Basket cells have been reported to be myelinated in occipital<sup>167</sup> and somatosensory<sup>169</sup> cortex of the rat. PV-immunoreactive myelinated neurons have been identified in the rat entorhinal cortex<sup>175</sup>, hippocampus<sup>178</sup> and striatum.<sup>179</sup> In the rat entorhinal cortex, myelinated PV+ axons were found extensively across all cortical layers, interspersed

Study	Species	Region	Technique	Conclusion
Micheva <i>et al.</i> <sup>216</sup>	Mouse	Somatosensory cortex	Array tomography; EM	~25–50% of myelinated axons in the neocortex are GABAergic, of which nearly all are PV+
McGee <i>et al.</i> <sup>160</sup>	Mouse	Visual cortex	IF	~ One-third of myelinated axons are PV+
Somogyi <i>et al.</i> <sup>161</sup>	Cat	Visual cortex	EM	Presence of several myelinated basket cells
Somogyi <i>et al.</i> <sup>172</sup>	Cat	Visual cortex	EM	Presence of two myelinated basket cells
Chung <i>et al.</i> <sup>181</sup>	Human	Frontal cortex	IF; CLARITY	Single figure of myelinated PV+ axons
Seress <i>et al.</i> <sup>183</sup>	Human	Hippocampus	EM	Presence of a few myelinated PV+ axons
Hinova-Palova <i>et al.</i> <sup>184</sup>	Human	Clastrum	EM; IF	Presence of several myelinated PV+ axons
Peters <i>et al.</i> <sup>167</sup>	Rat	Visual cortex	EM	Presence of several myelinated basket cells
Wouterlood <i>et al.</i> <sup>175</sup>	Rat	Entorhinal cortex	EM	Extensive presence of myelinated PV+ axons throughout all cortical layers
Gartner <i>et al.</i> <sup>170</sup> Brauer <i>et al.</i> <sup>187</sup>	Rat	Hippocampus	IF; EM	Majority of septohippocampal PV+ fibers show myelination, but not cholinergic ones
Kita <i>et al.</i> <sup>179</sup>	Rat	Neostriatum	EM; LM	Presence of several myelinated PV+ neurons
Freeman <i>et al.</i> <sup>173</sup>	Rat	Hippocampus ( <i>in vitro</i> )	Hippocampal Cultures; IF	Myelination of PV+ neurons <i>in vitro</i>
Katsumaru <i>et al.</i> <sup>178</sup>	Rat	Hippocampus	EM	Presence of myelinated PV+ neurons
Hu <i>et al.</i> <sup>223</sup>	Rat	Hippocampal dentate gyrus	IF	No myelinated PV+ fibers present

**Table 2.3.** Studies reporting myelination of PV+ interneurons. Abbreviations: EM, electron microscopy; IF, immunofluorescence; LM, light microscopy.

with unmyelinated axonal segments.<sup>175</sup> Furthermore, myelinated GABAergic neurons have been identified in the rodent hippocampus<sup>166,173</sup>, thalamus<sup>168,176</sup>, and inferior colliculus<sup>177</sup>, although these studies were performed largely without interneuron subtype-specific labeling.<sup>175</sup> However in one notable exception, myelinated rat hippocampal GABAergic neurons were confirmed as PV+ interneurons<sup>173</sup>. Moreover, the vast majority of septohippocampal PV, but not cholinergic, fibers are myelinated.<sup>170,171,187</sup>

Few studies have reported attempts to examine myelination of interneurons in human cortex. Myelination of PV+ cells in the human hippocampus<sup>183</sup> and claustrum<sup>184</sup> has been confirmed by electron microscopy. Furthermore, myelinated GABAergic<sup>182</sup> interneurons have been incidentally observed in the human frontal cortex, including with PV+ interneuron subtype specification<sup>181</sup>. Thus, although sparsely documented, PV+ interneuron myelination appears to be widespread throughout the brain and evolutionarily conserved among mammals. More detailed and comprehensive studies are required to quantify the relative proportion of myelinated PV+ interneurons, their developmental time course of myelination compared to pyramidal neurons,

subcellular distribution of segmental myelination, and brain region distribution, as well as the functional neurophysiological implications of interneuron myelination.

Notably, we have not found any report demonstrating myelination of cortical somatostatin (SOM) or neuropeptide Y (NPY) interneurons, despite numerous electron microscopic studies in a variety of mammalian species<sup>188-191</sup>, thereby suggesting a high specificity for the PV+ subclass of GABAergic interneurons. In contrast, non-PV interneuron myelination has been sporadically reported in subcortical regions, for example in sparse small-diameter axons of the rat internal capsule<sup>192</sup> and in the cat claustrum.<sup>193</sup> This suggests that at least within the cerebral cortex, PV cells are the predominant myelinated interneuron subtype while in subcortical brain regions the cell-type distribution of myelinated interneurons may be less strict.

Recently, it has been shown that PV+ interneurons establish direct functional soma-targeted contacts with OPCs in cortical layer V.<sup>194</sup> Synaptic input from local GABAergic interneurons has been shown to dynamically regulate OPC differentiation to oligodendrocytes.<sup>195</sup> OPCs receive strong GABAergic synaptic input from PV+, and to a lesser extent from non-PV+, interneurons.<sup>194</sup> Notably, the peak neurodevelopmental period of interneuron-OPC connectivity (p10 - p14) would thus position interneuron myelination precisely in the window following the initial onset of GABAergic burst firing, but prior to maturation of high-frequency gamma oscillations.<sup>196</sup> This also closely aligns with the timing of human frontal cortex oligodendrocyte development which plateaus in early adulthood<sup>16</sup> and is highly distinct from white matter development in which oligodendrocytes have already reached their maximum number by approximately five years of age.<sup>16</sup> Moreover, in further contrast to white matter, frontal cortex grey matter exhibits a substantial turnover of oligodendrocytes and myelin that persists throughout adulthood.<sup>16</sup> Analogously, rodent studies have demonstrated that OPCs exhibit important distinctions in their physiology, proliferation, and differentiation between grey and white matter in rodents.<sup>197</sup> Therefore, regional differences in human OPCs are also not unlikely.

Interestingly, direct contacts of interneurons onto OPCs<sup>198</sup> are only locally distributed, reaching a typical maximum distance of ~50-70  $\mu\text{m}$ <sup>194</sup>, which is notably highly similar to the estimate for the maximal length of OPC processes. An interesting question remains why interneurons have such a restricted spatial localization of their connectivity onto OPCs, since PV+ cells establish synaptic contacts with pyramidal cells across a distance approximately six times larger.<sup>199</sup> One possibility is that OPCs utilize reciprocal synaptic input to regulate their proliferative drive. Alternatively, it may be that myelination preferentially occurs on proximal axonal segments, in close apposition to the observed localization of OPCs and allowing for rapid differentiation to oligodendrocytes with enhanced myelination plasticity.

## Potential functions of interneuron myelination

PV+ interneurons function to synchronize pyramidal cell ensembles, and thereby generate high-frequency oscillations.<sup>200</sup> Since cortical PV+ axonal arborization is widely ramified and distributed over distances up to 300  $\mu\text{m}$ <sup>199</sup>, there might be considerable benefits of myelination for optimizing the fidelity of fast action potential transmission. Indeed, computational modeling has suggested a unique contribution of (interneuron) conductance delays in the dynamics of gamma frequency oscillations.<sup>201</sup> Evidence exists that nodes of Ranvier begin forming prior to the onset of myelination<sup>173</sup>, a mechanism specific for GABAergic neurons, which enhances axonal conduction of action potentials without myelin. Thus, in addition to simply increasing the speed of action potential propagation, myelin could function to ensure the integrity of precisely timed action potentials, as has been proposed for myelinated excitatory axons.<sup>202</sup> Myelin plasticity would then have the potential to support the local synchronization of action potentials necessary for generating high-frequency oscillations.<sup>203</sup> Indeed, myelinated axons exhibit both higher conduction velocities and enhanced long-range coherence.<sup>204</sup> Although non-PV+ cortical interneuron subtypes (e.g. SOM, VIP) exhibit synaptic connectivity across similar distances<sup>199</sup>, their lack of influence in maintaining high-frequency oscillations is consistent with their absence of myelination. Furthermore, the activity-dependence of myelination<sup>25</sup> might permit dynamically-regulated influences on the fidelity of fast action potential transmission and high-frequency oscillations.

Furthermore, myelin could provide metabolic and trophic support for energetically-costly PV+ cells. PV+ cell characteristics, including high-frequency spiking and rapid action potential kinetics, require a particularly high energy utilization through predominantly mitochondrial oxidative phosphorylation.<sup>205</sup> Gamma band synchrony, closely linked to cognition, is highly sensitive to metabolic disruption. Furthermore, compared to pyramidal cells, PV+ cells exhibit high densities of mitochondria and expression of cytochrome c and cytochrome c oxidase, proteins crucial for the electron transport chain. Moreover, PV+ cell-specific disruption of cytochrome oxidase assembly leads to changes in PV+ cell intrinsic excitability, afferent synaptic input, and gamma/theta oscillations, as well as schizophrenia-related behavioral impairments in sensory gating and social behavior.<sup>206</sup> During gamma oscillations, peak oxygen consumption approaches the demand observed during seizures and mitochondrial oxidative capacity operates near its functional limit.<sup>205</sup> Metabolic and trophic support conferred by myelination<sup>36,37</sup> might therefore allow PV+ axons to optimize their energy utilization. Consistent with the importance of myelination in regulating axonal energy metabolism is the considerable discrepancy of mitochondria content (30-fold) in myelinated versus unmyelinated pyramidal cell axons<sup>207</sup> which is also paralleled in PV+ interneuron axons. Myelin has been proposed to regulate axonal energy metabolism via the monocarboxylate transporter 1 (MCT1) channel<sup>143</sup>. Furthermore, the high peak oxygen consumption of PV+ cells

---

during gamma band synchrony could require the additional lactate provided by oligodendrocytes.

Taken together, the electrophysiological dynamics of fast-spiking PV+ interneurons, their dense branching onto pyramidal neurons requiring finely-tuned temporally-synchronized inhibition, and their high energy consumption are likely interdependent mechanisms governed by PV+ interneuron myelination.

## **Implications for Schizophrenia**

Both interneuron dysfunction and myelination abnormalities have been independently proposed as important contributors to the underlying pathophysiology of schizophrenia. These mechanisms have each amassed convincing support from post mortem histopathology, *in vivo* imaging and electrophysiology, genetics, and neurodevelopment (Table 2.1). However, neither hypothesis is capable of accounting for the full set of clinical research findings in schizophrenia. In contrast, interneuron myelination brings together both of these models, explains a more comprehensive portion of the existing data, and offers a well-defined falsifiable model.

Impairments of PV+ interneuron myelination could directly contribute to schizophrenia through several mechanisms. Impaired action potential fidelity, energy restrictions during highly-demanding cognitive tasks, aberrant axonal branching, and a higher occurrence of ectopic action potentials could each independently, or in combination, disrupt inhibitory network function. Such changes to PV+ interneurons would likely result in abnormalities of local gamma synchronization, with a potential further impact on the integrity of long-range thalamocortical and corticostriatal circuits, and striatal dopamine signaling, ultimately giving rise to schizophrenia symptoms.

In this review, we have proposed the novel hypothesis that altered myelination of PV+ interneurons might function prominently in the pathophysiology of schizophrenia. However, many questions remain to be answered. At what point during development does interneuron myelination occur and to what extent does this coincide with the clinical symptoms of schizophrenia? Does interneuron myelination vary across brain regions? Is cortical interneuron myelination truly reserved for fast-spiking PV+ interneurons, or are non-fast-spiking interneurons (e.g., SOM, VIP) myelinated as well? How does the plasticity of PV+ interneuron myelination compare to that of glutamatergic axons? And perhaps most importantly, to what extent might PV+ interneuron myelination represent an etiological pathophysiology and therapeutic target for schizophrenia?

---

Future studies to examine the parvalbumin interneuron myelination hypothesis could be approached through a variety of methods. In particular, the most important experiments would include: a) detailed histological assessment of subtype-specific interneuron axonal myelination in post mortem brain tissue from patients with schizophrenia, b) corresponding functional studies in rodent models of schizophrenia to directly assess the causality of alterations in myelination on behavioral and electrophysiological phenotypes, c) electrophysiological studies of rodent models with temporally and spatially-restricted disruption of myelination, and d) functional genomic studies on the effect of schizophrenia risk variants on (interneuron) myelination, for example by utilizing human induced pluripotent stem cells (iPSCs) and genetically-modified mice.





# Fast-Spiking Parvalbumin Interneurons are Frequently Myelinated in the Cerebral Cortex of Mice and Humans

## Chapter 3

J. Stedehouder<sup>1</sup>, J. J. Couey<sup>1</sup>, D. Brizee<sup>1</sup>, B. Hosseini<sup>1</sup>,  
J. A. Slotman<sup>2</sup>, C. M. F. Dirven<sup>3</sup>, G. Shpak<sup>1</sup>, A. B. Houtsmuller<sup>2</sup>, S. A. Kushner<sup>1</sup>

1. Department of Psychiatry, Erasmus MC Rotterdam, The Netherlands
2. Optical Imaging Center, Department of Pathology, Erasmus MC Rotterdam, The Netherlands
3. Department of Neurosurgery, Erasmus MC Rotterdam, The Netherlands

## Abstract

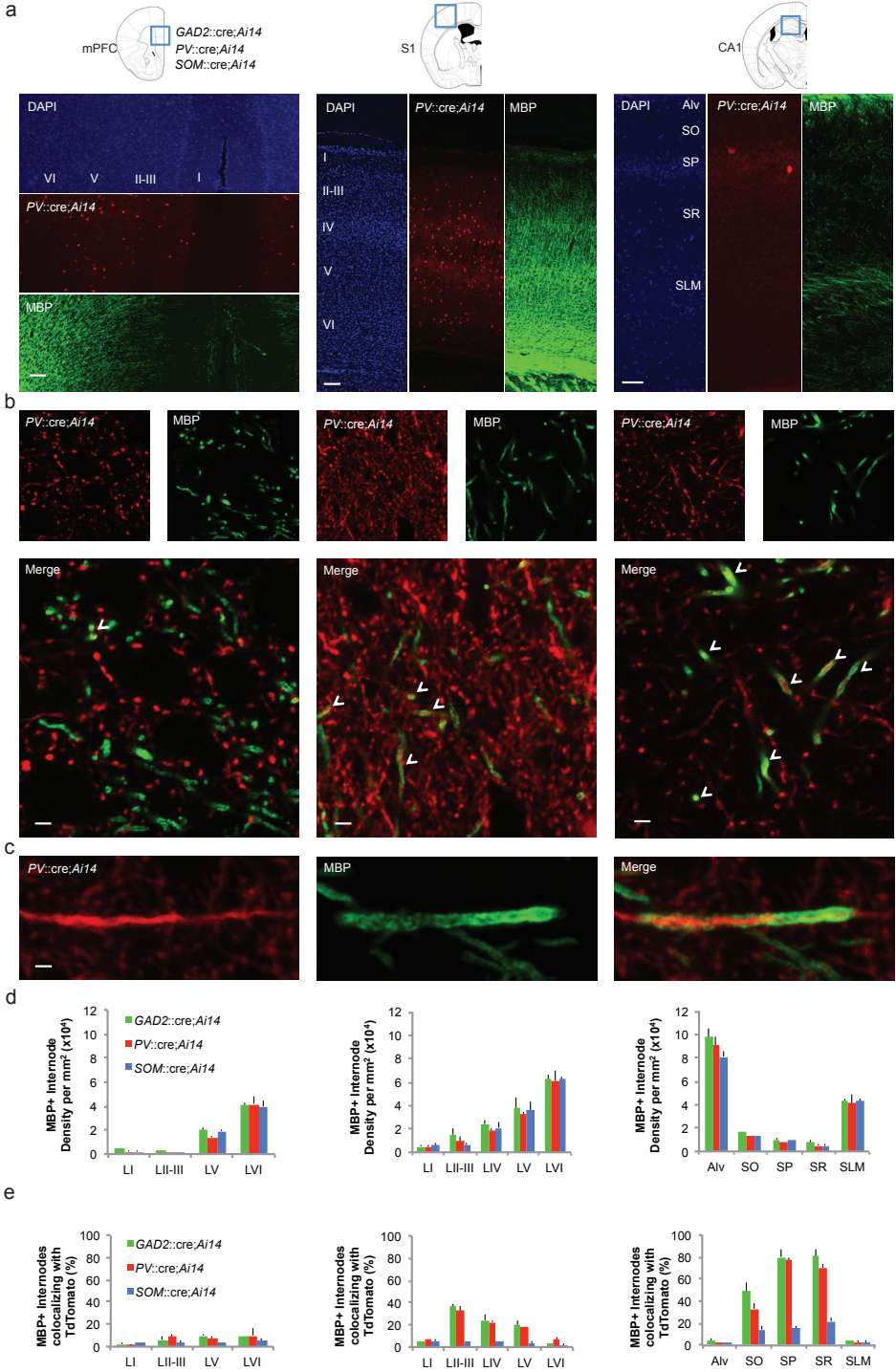
Myelination, the insulating ensheathment of axons by oligodendrocytes, is thought to both optimize signal propagation and provide metabolic support. Despite the well-established physiological importance of myelination to neuronal function, relatively little is known about the myelination of GABAergic interneurons in the cerebral cortex. Here, we report that a large fraction of myelin in mouse cerebral cortex ensheaths GABAergic interneurons, reaching up to 80% in hippocampal subregions. Moreover, we find that a very high proportion of neocortical and hippocampal parvalbumin (PV) interneurons exhibit axonal myelination. Using a combination of intracellular recordings and biocytin labeling of *ex vivo* human neocortex, we also confirm that axons of fast-spiking PV<sup>+</sup> interneurons are extensively myelinated in the human brain. PV<sup>+</sup> interneuron myelination in both mice and humans exhibits a stereotyped topography with a bias towards proximal axonal segments and relatively short internodes (~27  $\mu\text{m}$ ) interspersed with branch points. Interestingly, myelin-deficient *Shiverer* mice exhibit an increased density and more proximal location of en-passant boutons, suggesting that myelination might function in part to regulate synapse formation along PV<sup>+</sup> interneuron axons. Taken together, fast-spiking interneuron myelination is likely to have broad implications for cerebral cortex function in health and disease.

## Introduction

Myelination is the insulating ensheathment of axons by oligodendrocytes, demonstrated to optimize action potential propagation and metabolic demands.<sup>9,36,38</sup> Axonal myelination has recently been shown to be modulated by neuronal activity<sup>208</sup> and social experience<sup>209,210</sup>, and impaired in several psychiatric disorders including schizophrenia, bipolar disorder, and autism spectrum disorder.<sup>211–214</sup>

In the cerebral cortex, the myelination of pyramidal neurons has been extensively investigated<sup>215</sup>, but comparatively little is known about myelination of GABAergic interneurons. Several studies have reported myelination of local GABAergic interneurons throughout the brain.<sup>160,216,217</sup> However, the ubiquity of cerebral cortex parvalbumin-positive (PV+) interneuron myelination remains largely unexplored in mice, and has rarely been investigated in humans. GABAergic interneurons exert a powerful modulation on local cerebral cortex network activity and brain oscillations. In particular, the fast-spiking, PV+ subclass of interneurons function crucially in governing feedforward and feedback inhibition in cortical microcircuits, as well as tightly regulating fast network oscillations.<sup>47</sup> Dysfunction of PV+ interneuron function has been strongly linked to multiple psychiatric disorders.<sup>53</sup>

In the current study, we examined the myelination of GABAergic interneurons in the cerebral cortex of mice and humans. Using cell-type specific fluorescent reporter lines, we found that a substantial fraction of myelin in the cortex and hippocampus belongs to GABAergic interneurons, in particular fast-spiking PV+ interneurons. Using viral labeling, the vast majority of PV+ interneurons we examined in the cortex and hippocampus exhibited myelinated axons. Furthermore, we independently replicated this finding in both mouse and human cerebral cortex using intracellular biocytin labeling during patch-clamp recordings followed by axonal reconstructions. PV+ interneuron myelination exhibited a topography biased towards proximal axonal segments interspersed by unmyelinated branch points. Local axonal morphology was correlated with myelination status, in which inter-branch point distances were shorter when the corresponding axonal segment was unmyelinated. Additionally, myelin-deficient *Shiverer* mice exhibited an increased density of proximal en-passant boutons, suggesting that myelination functions to regulate the axonal morphology of PV+ interneurons in the cerebral cortex.



## Results

### A substantial fraction of cerebral cortex myelin ensheaths PV+ interneurons

To examine the extent to which GABAergic axons are myelinated in the mouse brain, we utilized the Ai14 cre-dependent fluorescence reporter strain in combination with cre driver lines for either parvalbumin (PV) or somatostatin (SOM) interneuron subclasses, or broadly among GABAergic interneurons (Glutamate Decarboxylase 2; GAD65; GAD2). Specifically, we quantified axonal co-localization between the interneuron subclass-specific expression of tdTomato (Ai14) and myelin basic protein (MBP) in the medial prefrontal cortex (mPFC), primary somatosensory cortex (SI), and hippocampal CA1 subregion (CA1) using confocal microscopy (Fig. 3.1a-c, Supplementary Fig. 3.1) and structured illumination microscopy (SIM; Supplementary Fig. 3.2). We observed a systematic gradient of overall myelination across cell layers (Fig. 3.1d; all regions  $P < 0.001$ ), but importantly without variability of internode density across cre driver lines ( $P = 0.101$ ). Similar to the recent finding of Micheva *et al.*<sup>216</sup>, a sizeable fraction of SI myelination was attributable to PV+ axons (32.6% in SI layer II-III) with only a minimal contribution of SOM+ axons or other GAD65+ interneuron subclasses (Fig. 3.1e). The contribution of PV+ interneuron myelination varied across brain regions ( $P = 0.005$ ), for which the hippocampal CA1 contribution was significantly higher (76.9% in stratum pyramidale) and the mPFC significantly lower (10.1% in layer VI) than in SI (32.6% in layer II/III). Together, these data confirm that a substantial fraction of cerebral cortex myelin is contributed by PV+ interneurons, albeit with regional variation.

**Figure 3.1.** Interneuron myelination is cell-type and region-dependent. (a) Representative low magnification images of PV::cre;Ai14 (red), MBP (green) and DAPI (blue) in the medial prefrontal cortex (mPFC), somatosensory cortex (SI) and hippocampal dorsal CA1 region (CA1). Cell layers are annotated in the DAPI channel. Scale bars for mPFC, SI and CA1 are 80  $\mu\text{m}$ , 80  $\mu\text{m}$ , and 30  $\mu\text{m}$ , respectively. (b) Representative confocal co-localization (arrowheads) between tdTomato (red) and MBP (green) in each respective brain region. Scale bars are 5  $\mu\text{m}$ . (c) Representative co-localization between tdTomato+ axon (red) and MBP (green), demonstrating a myelinated axonal segment. Scale bar, 5  $\mu\text{m}$ . (d) MBP+ internode density varied significantly across cell layers in each brain region examined ( $P < 0.001$  for mPFC, SI and CA1; one-way analyses of variance). In contrast, as expected there were no differences in internode density between PV::cre;Ai14, SOM::cre;Ai14, and GAD2::cre;Ai14 reporter lines (repeated measures analysis of variance, Region  $\times$  Genotype interaction,  $P = 0.101$ ). (e) Co localization of PV::cre;Ai14, SOM::cre;Ai14, and GAD2::cre;Ai14 with MBP across cell layers and between regions. Interneuron myelination exhibited a significant Region  $\times$  Genotype interaction ( $P = 0.002$ ), with main effects of both Region ( $P = 0.005$ ) and Genotype ( $P = 0.010$ ). *Post hoc* Tukey's test revealed significant differences between PV and SOM myelination in SI ( $P < 0.001$ ) and CA1 ( $P = 0.002$ ), but not mPFC ( $P = 0.722$ ).  $n = 3$  mice per genotype per region. Alv Alveus; SO Stratum oriens; SP Stratum pyramidale; SR Stratum radiatum; SLM Stratum lacunosum-moleculare.

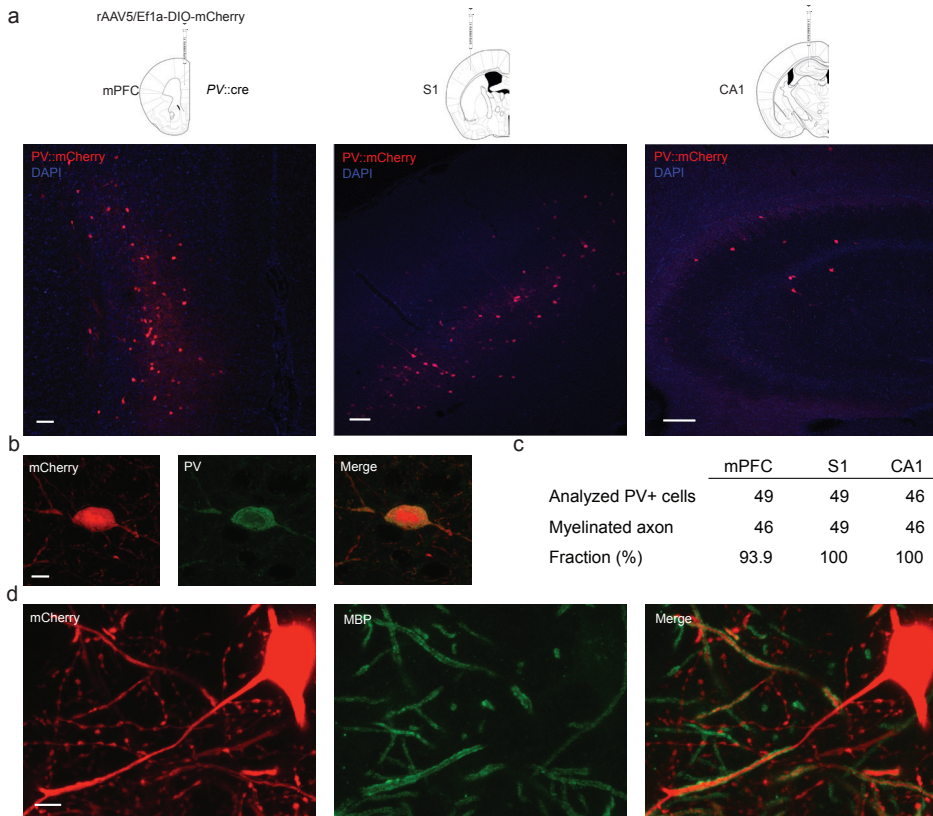


**Figure 3.2.** PV+ interneurons frequently exhibit axonal myelination. (a) PV::cre mice were injected with rAAV5/Ef1a-DIO-mCherry virus for PV-specific labeling, and sacrificed four weeks later. Low-magnification confocal images of PV::cre mice (representative images of  $n = 7$  mice) with virally-labelled PV+ cells (mCherry; red) in mPFC, S1 and hippocampal CA1. DAPI (blue) is shown for orientation. Scale bars, 100  $\mu\text{m}$ . (b) Representative co-localization between mCherry (red) and PV (green) in S1. Scale bar, 10  $\mu\text{m}$ . (c) The overwhelming majority of PV+ cells in the cerebral cortex have myelinated axons. (d) Representative co-localization between an mCherry-filled axon (red) and MBP (green), demonstrating a myelinated axonal segment. Scale bar, 5  $\mu\text{m}$ .

## A high proportion of PV+ interneurons exhibit myelinated axons

We next asked whether cortical PV+ interneuron myelination is limited to a subset of cells or is more broadly distributed. Sparse labeling of PV+ interneurons was performed using the PV::cre driver line in combination with stereotactic injections of reduced-titer rAAV5/Ef1a-DIO-mCherry virus into mPFC, S1, or CA1 (Fig. 3.2a). Axons originating from PV+ somata randomly sampled across different layers ( $n = 144$ ; Fig. 3.2a,b) were examined for MBP immunofluorescence (Fig. 3.2d). Of the 144 PV+ interneurons examined, 141 (97.9%) exhibited axonal myelination (Fig. 3.2c). This suggests that cerebral cortex PV+ interneurons are frequently myelinated, independent of cell layer or brain region.

## Fast-spiking PV+ cells exhibit region-dependent proximal myelination

Next, we addressed the topography of PV+ axonal myelination in order to examine whether internodes are spatially biased along PV+ axons or randomly distributed. We performed whole-cell electrophysiological recordings and intracellular biocytin-labeling of fast-spiking interneurons ( $n = 31$ ; Supplementary Fig. 3.3a,b; Supplementary Table 3.1) with *post hoc* morphological reconstruction and PV/MBP immunofluorescence labeling in mPFC, SI, and CA1 (Fig. 3.3a,b). Consistent with the results obtained with sparse viral labeling, we found that 30 of the 31 reconstructed fast-spiking PV+ cells exhibited myelination (total: 96.8%; mPFC: 10/11 cells [90.9%], SI: 11/11 cells [100%], CA1: 9/9 cells [100%]; Fig. 3.3c,d). Notably, PV+ interneurons were myelinated irrespective of whether their axons originated from the soma or primary dendrite.

Reconstruction of biocytin-labeled cells allowed for classification by axonal and dendritic morphology (Supplementary Fig. 3.4a,b). In mPFC, 11 out of 11 PV+ cells were morphologically identified as basket cells (100%). Of the 11 reconstructed cells in SI, seven cells had a basket cell morphology (63.6%), one had a basket cell morphology with large horizontally extending axons and dendrites (horizontally-elongated cell;<sup>43</sup> 9.1%), and three had a shrub cell morphology<sup>43</sup> (27.3%). In CA1, we found three distinct morphological subtypes of PV+ cells: four of the nine reconstructed cells had a bistratified morphology with an axon predominantly innervating stratum oriens and radiatum (44.4%), while another four cells had a perisomatic morphology primarily innervating the pyramidal cell layer (44.4%). The final cell had chandelier morphology (11.1%), with distinct axo-axonic bouton cartridges originating in stratum oriens and directed orthogonally towards the pyramidal cell layer. These findings suggest that PV+ interneuron myelination extends beyond the classical basket cell to include a variety of morphological subtypes.

Detailed axonal reconstructions including myelination (Fig. 3.3c,d; Supplementary Fig. 3.4c, Supplementary Fig. 3.5) revealed that PV+ interneuron myelination was disproportionately located on proximal axonal segments. The proximal beginning of the first internode was found an average distance of 31.4  $\mu\text{m}$  from the origin of the axon (mPFC:  $31.1 \pm 2.1 \mu\text{m}$ ; SI:  $27.2 \pm 1.9 \mu\text{m}$ ; CA1:  $38.1 \pm 4.4 \mu\text{m}$ ), and typically occurred before the first axonal branch point (mPFC: 81.8%; SI: 90.9%; CA1: 56.6%) located at an average distance of 49.8  $\mu\text{m}$  from the soma (mPFC:  $45.7 \pm 4.4 \mu\text{m}$ ; SI:  $48.8 \pm 4.8 \mu\text{m}$ ; CA1:  $56.2 \pm 8.0 \mu\text{m}$ ). One cell in the mPFC had an atypical topography of myelination, in which no internodes were found until immediately distal to the secondary axonal branch points (Supplementary Fig. 3.6). Overall, internodes of PV+ interneurons had an average length of 27.2  $\mu\text{m}$ , which varied significantly between regions (mPFC:  $23.3 \pm 1.5 \mu\text{m}$ ,  $n = 54$  internodes; SI:  $26.0 \pm 1.1 \mu\text{m}$ ,  $n = 141$ ; CA1:  $33.7 \pm 2.4 \mu\text{m}$ ,  $n = 44$ ;  $P = 0.008$ ), with similarly right-skewed distributions (Fig.

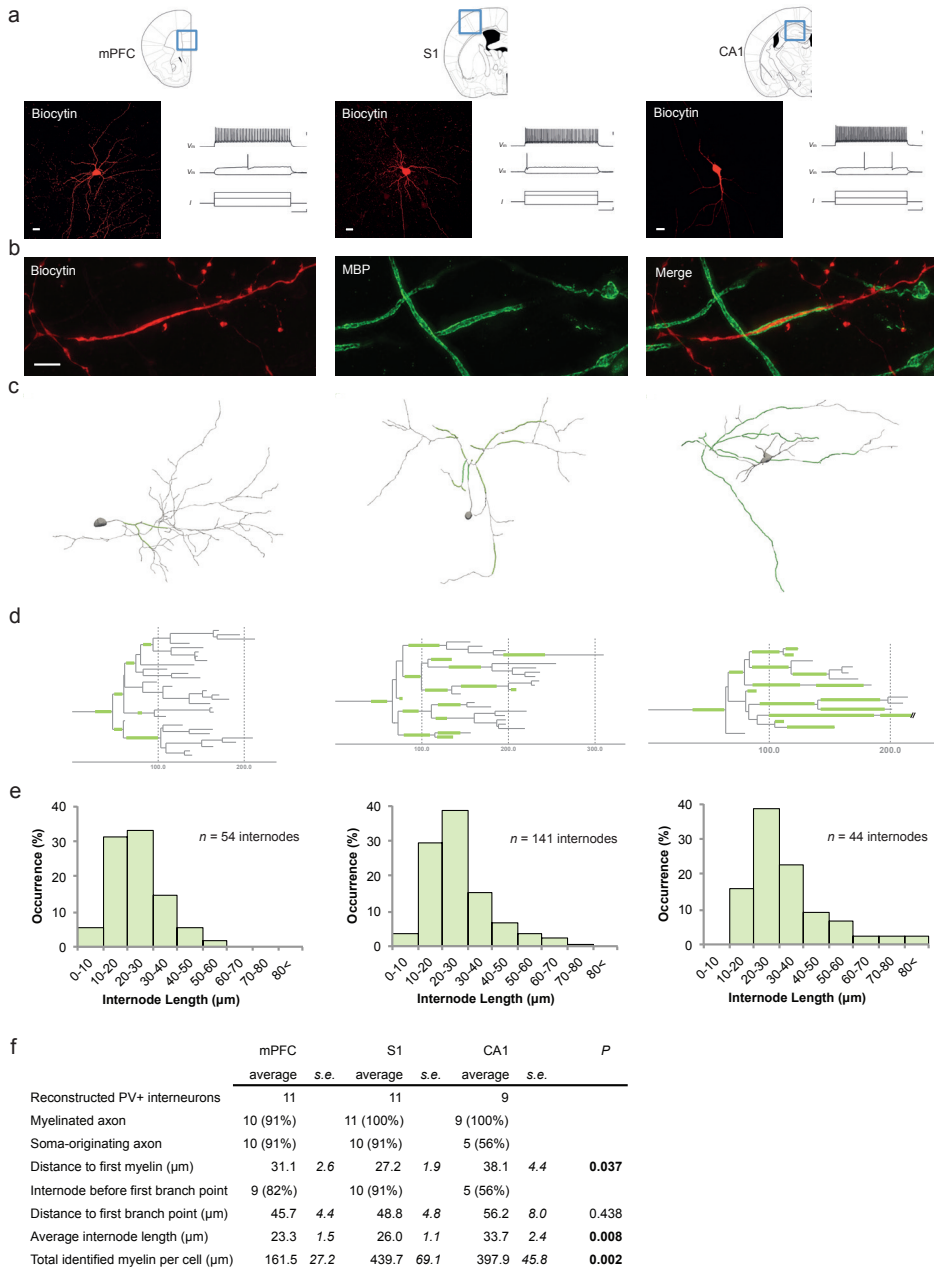


**Figure 3.3.** Topography and regional variation of PV+ interneuron myelination. (a) Maximum projection confocal images of representative biocytin-filled PV+ cells (red) with a corresponding fast-spiking AP train in mPFC (left), S1 (center) and CA1 (right). Scale bars for electrophysiological traces are 20 mV, 100 ms, and 100 pA from top to bottom, respectively. (b) High-resolution SIM co-localization between a biocytin-labelled axon (red) and MBP (green), demonstrating a myelinated axonal segment. Scale bar, 10 μm. (c) Partial reconstructions of representative PV+ cells in mPFC, S1 and CA1. Soma and axon are shown in grey, and myelinated internodes are shown in green. Note the proximal onset and interspersed branch points between internodes. Dendrites have been removed to facilitate axonal visualization. Note the dendrite-originating axon in the right panel. (d) Axonal dendrograms showing the schematic myelin localization for each cell in (c). Axon in grey, myelin in green. Horizontal axis, μm. (e) Histogram of internode length per region (mPFC:  $n = 54$  internodes, 10 cells; S1:  $n = 141$  internodes, 11 cells; CA1:  $n = 44$  internodes, 9 cells). (f) Regional characteristics of PV+ axonal myelination. *P*-values are based on a one-way analysis of variance.

3.3e). The mean total identified length of axonal myelination was 332.2  $\mu\text{m}$  per cell, which varied significantly across brain regions (mPFC:  $161.5 \pm 27.2 \mu\text{m}$ ; SI:  $439.7 \pm 69.1 \mu\text{m}$ ; CA1:  $397.9 \pm 45.8 \mu\text{m}$ ;  $P = 0.002$ , Fig. 3.3f). On average, we identified  $\sim 12$  internodes per cell (mPFC:  $6.6 \pm 0.7$  internodes per cell; SI:  $14.7 \pm 2.2$  internodes per cell; CA1:  $13.0 \pm 1.6$  internodes per cell). Similar to earlier findings<sup>218</sup>, we almost never observed myelination of branch points (Supplementary Fig. 3.3c).

To confirm whether myelin integrity may have been compromised during the whole-cell patch-clamp tissue preparation, we compared internodes from the *in vivo* viral labeling experiments (Fig. 3.2) with those obtained from the reconstructions following intracellular biocytin labeling (Fig. 3.3). No differences in any region were observed between methods (Supplementary Table 3.2), thereby providing an independent replication of the results and a validation of the two distinct methodologies for quantifying internodal segments.

### **PV+ axons are frequently myelinated in the human brain**

Next, we examined whether myelination of fast-spiking PV+ interneurons extends to humans. *Ex vivo* whole-cell patch clamp recording and intracellular biocytin labeling was performed in acutely resected neocortex obtained from patients undergoing surgery for subcortical tumors ( $n = 13$  cells, 3 donors; Fig. 3.4). Interneurons were readily categorized as fast-spiking ( $n = 10$ ) or non-fast-spiking ( $n = 3$ ) based on their electrophysiological profile (Fig. 3.4a,b; Supplementary Table 3.3). Human fast-spiking interneurons exhibited two distinct electrophysiological characteristics not observed in mouse – pronounced sag at hyperpolarizing levels and near-threshold ‘humps’, both of which have been previously reported in *ex vivo* recordings from acute non-human primate tissue.<sup>219-220</sup>

All of the human fast-spiking interneurons we examined (10/10 cells; 100%), but none of the non-fast-spiking cells (0/3 cells), exhibited myelinated axons ( $P = 0.003$ ; Fig. 3.4e-g). Notably, eight of the 10 fast-spiking cells (80%) but none of the non-fast-spiking cells (0/3 cells; 0%) were PV+ ( $P = 0.035$ ; Fig. 3.4c,d). Among the eight fast-spiking PV+ cells, all had a basket cell morphology. The two fast-spiking PV– cells included a basket cell and a double-bouquet cell. Although the absence of PV labeling in these two fast-spiking cells could have resulted from washout during whole cell recordings, it is notable that a small subset of fast-spiking cells in the mouse neocortex has recently been confirmed to lack PV expression, in particular double-bouquet cells.<sup>43</sup> Moreover, a subset of basket cells in the neocortex of non-human primates has also been demonstrated to lack PV expression.<sup>220</sup>

Similar to our findings in mice, fast-spiking interneuron myelination in the human neocortex was biased towards proximal axonal segments, beginning on average at

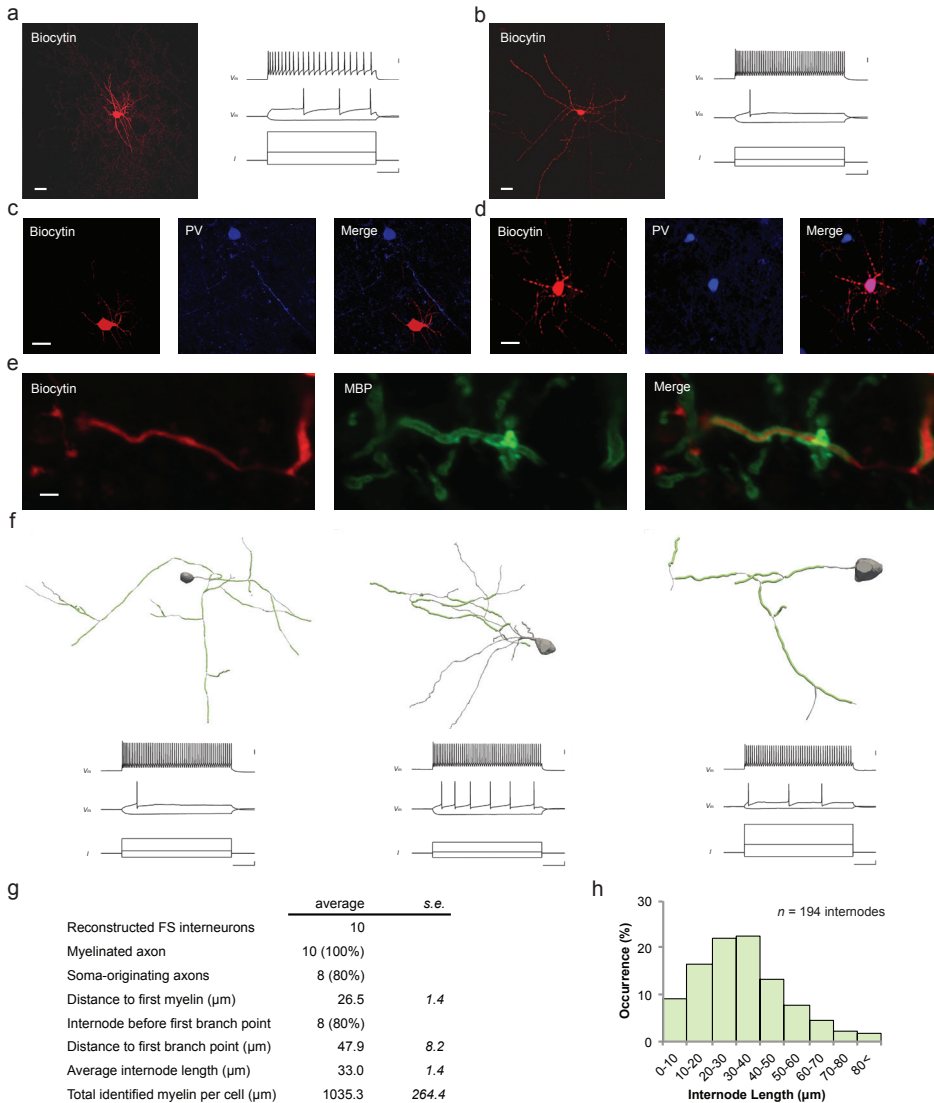


**Figure 3.4.** Fast-spiking PV+ interneurons are frequently myelinated in human brain. **(a,b)** Maximum projection confocal images of **(a)** non-fast-spiking and **(b)** fast-spiking biocytin-filled cells (red) from resected human surgical tissue. Scale bars, 15  $\mu\text{m}$ . Representative voltage responses to depolarizing and hyperpolarizing current injections. Fast-spiking cells exhibited a typical suprathreshold high frequency non-adapting firing pattern. **(c,d)** Biocytin-labelled cells (red) were classified as PV- **(c)** or PV+ **(d)** on the basis of the absence or presence of co-localization with PV (blue). Scale bars, 20  $\mu\text{m}$ . **(e)** Representative co-localization between biocytin-filled axons (red) and MBP (green), showing a myelinated axonal segment. Scale bar, 5  $\mu\text{m}$ . **(f)** Representative examples of partially reconstructed PV+ interneurons. Soma and axon are shown in grey, and myelinated internodes are shown in green. Note the proximal onset and interspersed branch points between internodes. Dendrites were removed from the left and right panels to facilitate axonal visualization. Note the dendrite-originating axon in the middle panel. Corresponding fast-spiking electrophysiological profiles are shown directly below each morphological reconstruction. **(g)** Characteristics of human fast-spiking interneuron axonal myelination. FS, fast-spiking. **(h)** Histogram of internode lengths ( $n = 194$  internodes, 10 cells). Scale bars for electrophysiological traces in **a**, **b** and **f** are 20 mV, 100 pA and 100 ms from top to bottom, respectively.

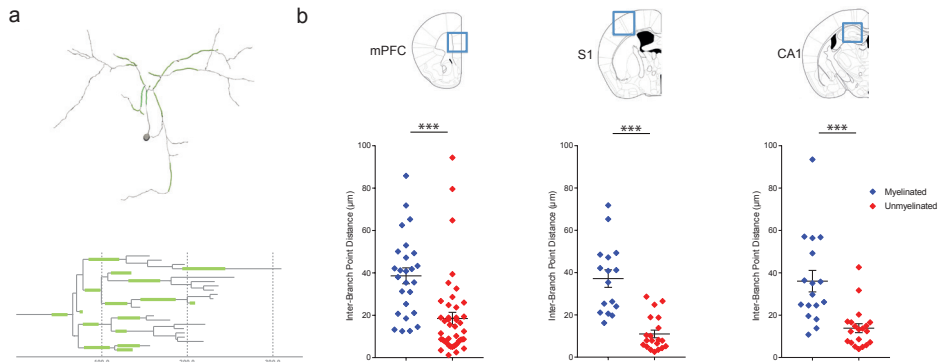


**Figure 3.5.** Axonal morphology predicts segmental myelination. (a) Representative PV+ interneuron reconstruction (top) from S1, along with its axonal dendrogram (bottom) with myelinated segments shown in green. Horizontal axis,  $\mu\text{m}$ . (b) Quantification of inter-branch point distances (2nd to 5th-order axonal branches) for myelinated versus unmyelinated segments in mPFC (left), S1 (middle), and CA1 (right). Myelinated axonal segments (blue) are significantly longer than unmyelinated segments (red) in all three regions.  $n = 4$  cells per region. \*\*\*  $P < 0.001$ ; Unpaired two-tailed Student's  $t$ -test.

$26.5 \pm 1.4 \mu\text{m}$  from the soma (Fig. 3.4f,g; Supplementary Fig. 3.7) and most commonly occurring before the first branch point (80%) located  $47.9 \pm 8.2 \mu\text{m}$  from the soma. Internodes had an average length of  $33.0 \pm 1.4 \mu\text{m}$  ( $n = 194$ ; Fig. 3.4h). The total length of identified axonal myelination per cell was  $1035.3 \pm 264.4 \mu\text{m}$ , which was notably longer than we observed in mice. On average, we identified  $31.6 \pm 2.5$  internodes per human fast-spiking interneuron. Together, these data suggest that myelination of neocortical fast-spiking interneurons is a conserved feature of both the mouse and human brain.

### PV+ axonal branch morphology predicts segmental myelination

Internodes along PV+ axons often ensheathed the full distance between branch points. However, inter-branch segments were frequently unmyelinated, particularly those of shorter distance (Fig. 3.3c,d). Given the relatively small proportion of internodes  $< 10 \mu\text{m}$  (Fig. 3.3e), we hypothesized that segmental myelination status might be correlated with inter-branch distance. To examine this directly, we quantified inter-branch point distances up to fifth-order axonal segments and whether each of these segments contained an internode (Fig. 3.5a). In line with our hypothesis, we found that unmyelinated inter-branch point segments were consistently shorter than corresponding myelinated segments ( $P < 0.001$  for mPFC, S1, and CA1; Fig. 3.5b). Overall, the majority of inter-branch segments  $\geq 15 \mu\text{m}$  showed myelination (66.7%), while inter-branch segments  $< 15 \mu\text{m}$  tended to be unmyelinated (90.8%). An analogous dichotomy was evident also in the location of the first axonal branch point, which was located closer to the soma when it arose before, compared to

after, the first internode ( $P = 0.010$ ). Together, this suggests that the likelihood of segmental myelination might be governed by spatial limitations imposed by axonal morphology.

### **Myelination regulates the density of PV+ axonal *en passant* boutons**

We observed that the most proximal *en passant* boutons were frequently positioned just a short distance beyond the distal end of myelination. Moreover, the one unmyelinated mPFC basket cell that we identified previously using confocal imaging showed a higher density and proximally shifted topography of *en passant* boutons (Supplementary Fig. 3.8). Consequently, we hypothesized that *en passant* bouton formation might be constrained by myelination. To examine this possibility directly, we quantified the density of proximal *en passant* boutons along PV+ interneuron axons in mPFC of myelin-deficient *Shiverer* mice (Fig. 3.6a, Supplementary Fig. 3.9). Using intracellular biocytin-labeling of fast-spiking PV+ interneurons and SIM (Fig. 3.6b,c), we observed a more proximal onset ( $P < 0.001$ ; *Shiverer*:  $47.4 \pm 5.7 \mu\text{m}$  from soma; WT:  $111.1 \mu\text{m} \pm 7.7$  from soma; Fig. 3.6d) and higher density ( $P = 0.013$ ; *Shiverer*:  $3.3 \pm 0.7$  boutons per  $100 \mu\text{m}$ ; WT:  $0.7 \pm 0.5$  boutons per  $100 \mu\text{m}$ ; Fig. 3.6e) of *en passant* boutons in the absence of myelination. However, axonal length was unchanged ( $P = 0.827$ ; *Shiverer*:  $137.8 \pm 6.9 \mu\text{m}$ ; WT:  $139.9 \pm 5.5 \mu\text{m}$ ; Fig. 3.6f). Together, these findings suggest that myelination regulates the density of PV+ axonal *en passant* boutons and offer additional support for a broad inter-relationship between axonal morphology and myelination.

### **Discussion**

In the present paper, we report that a substantial fraction of myelin in the cerebral cortex ensheaths axons of GABAergic interneurons, a finding predominately attributable to the fast-spiking PV+ subclass of interneurons. Moreover, utilizing two independent methodologies, we find that a high proportion of fast-spiking PV+ interneurons in mouse cerebral cortex exhibit axonal myelination. In addition, using *ex vivo* whole-cell recordings and intracellular biocytin labeling of human neocortex, we confirm that fast-spiking PV+ cells in the human brain are also frequently myelinated. PV+ interneuron myelination most commonly involves the proximal axon, consists of small internodes interspersed by axonal branch points, and occurs predominantly on longer inter-branch segments. Finally, and suggestive of a causal functional influence of myelination on PV+ axonal morphology, we find that myelin-deficient *Shiverer* mice exhibit an increased density and ectopic localization of *en passant* boutons.

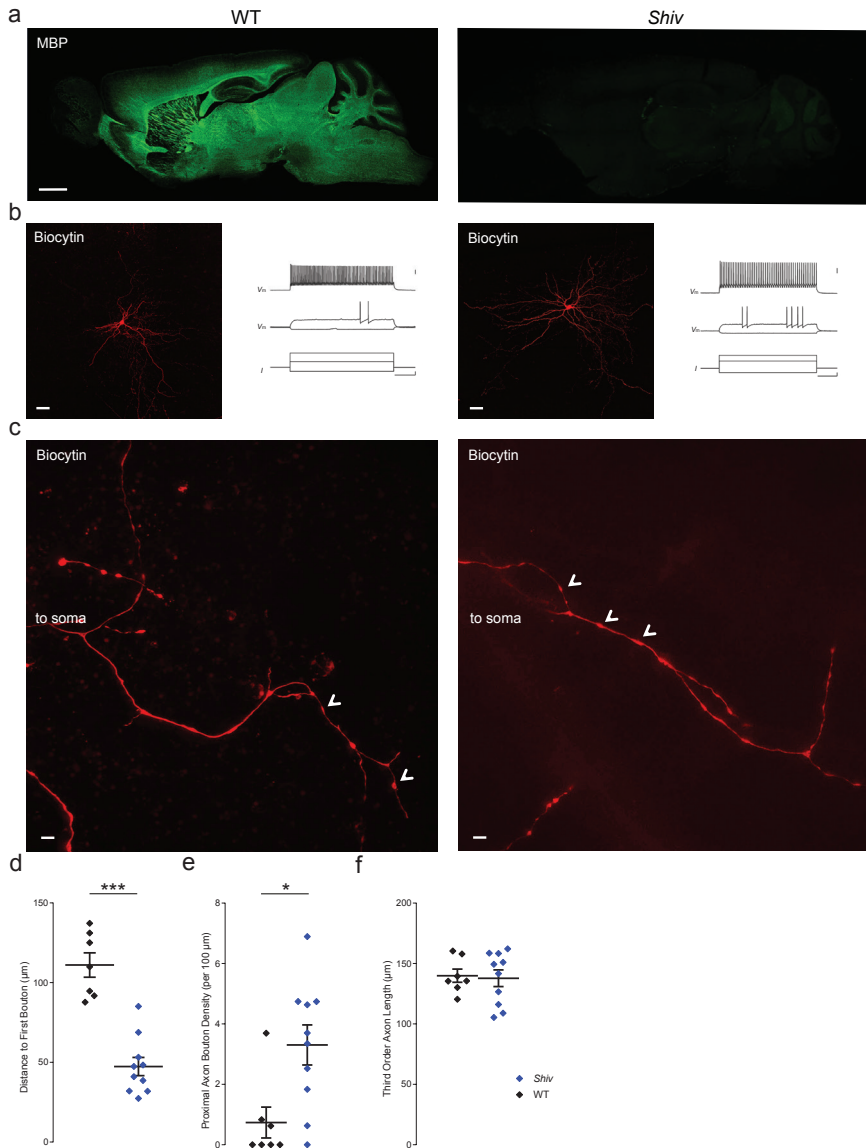


**Figure 3.6.** Altered PV+ axon morphology in myelin-deficient *Shiverer* mice. (a) Mid-sagittal section from *Shiverer* mice (*Shiv*) demonstrates the absence of MBP expression, whereas WT mice show extensive myelination (green). Scale bar, 1 mm. (b) Maximum projection confocal images of representative biocytin-filled PV+ cells (red) from the mPFC with a corresponding fast-spiking AP train in WT (left) and *Shiverer* (right) mice. Scale bars are 20 mV, 100 ms, and 100 pA from top to bottom, respectively. (c) High-resolution SIM images of biocytin-labelled axons, centered on the third branch order; showing morphological evidence of *en passant* boutons (arrowheads) in WT (left) and *Shiverer* (right). Scale bar, 10  $\mu$ m. (d) *Shiverer* mice (blue) have a significantly more proximal bouton onset, and (e) higher number of boutons on the proximal axon compared to WT mice (black). (f) Cumulative axonal length (through 3rd order axon branches) is unchanged ( $P = 0.827$ ). *Shiverer*.  $n = 10$  cells; WT:  $n = 7$  cells. Bars represent means  $\pm$  s.e.m. \*\*\* $P < 0.001$ ; \* $P = 0.013$ ; Unpaired two-tailed Student's *t*-test.

A recent study<sup>216</sup> reported a large contribution of GABAergic interneurons to the total myelin content of primary somatosensory cortex using array tomography and scanning electron microscopy. Our findings considerably extend these results by demonstrating that the contribution of GABAergic interneuron myelination is region-dependent, with the mPFC exhibiting a lower, and the hippocampus a higher, relative fraction of interneuron myelination. In the CA1 subregion of the hippocampus, nearly 80% of myelin in stratum pyramidale and radiatum originates from GABAergic interneurons, which is contributed almost exclusively by PV+ interneurons. This finding could suggest a particularly important contribution of interneuron myelination in hippocampal function. Alternatively, the high proportion of myelin contributed by GABAergic interneurons may simply reflect the limited myelination of CA1 pyramidal neurons. Regardless, in light of the predominant contribution of interneuron myelination to the total myelin content of the hippocampus, experience-dependent or neuropathological alterations of hippocampal myelination are likely to involve PV+ interneurons. Conversely, the relatively lower contribution of interneuron myelination in the prefrontal versus somatosensory cortex is at least in part, if not entirely, due to a more limited extent of myelination per PV+ interneuron. Notably however, our analysis was performed entirely during early adulthood for which it remains unknown whether the relative contribution of cerebral cortex interneuron myelination is neurodevelopmentally regulated.

In addition to PV+ interneuron myelination, we also find a small, but consistent, contribution of cortical myelin arising from axons of SOM+ interneurons. The contribution of SOM+ interneuron myelination is similar in mPFC and SI, but somewhat higher in CA1 consistent with the limited myelination of hippocampal principle cells.<sup>5</sup> SOM+ interneurons are a heterogeneous group of GABAergic cells with relatively lower firing rates than PV+ interneurons.<sup>221</sup> A precise quantification of the proportion of SOM+ interneurons that are myelinated, and whether they exhibit a similarly biased topography of proximal myelination as PV+ cells, remains to be determined.

Although the majority of our PV+ interneuron reconstructions exhibited a basket cell morphology, we also recovered fast-spiking PV+ bistratified, shrub, and chandelier cells in the CA1 subregion of the hippocampus, all of which had myelinated axons. Although these observations require further replication to be considered conclusive, they nevertheless suggest that PV+ interneuron myelination is likely to extend beyond the classical basket cell subtype. Moreover, they also highlight the question of whether each PV+ interneuron subtype has a unique topography and function of axonal myelination.

Using axonal reconstructions, we find that PV+ interneuron myelination has a spatially-biased topography with internodes occurring predominantly on axonal segments of low branch order. In particular, the first internode is typically positioned ~30  $\mu\text{m}$  from the soma, directly following the location of action potential initiation (~25  $\mu\text{m}$  from the soma) within the axon initial segment.<sup>222,223</sup> Interestingly, none of the cells showed exceptionally long distances to myelin onset (>60  $\mu\text{m}$ ), as has recently been shown for a subset of SI pyramidal cells.<sup>215</sup> In most instances, the first axonal branch point occurs immediately following the first internode at ~45  $\mu\text{m}$  from the soma. This stereotyped sequence of axon initial segment – internode – branch point raises the question of whether the first internode and branch point function to modulate action potential generation in PV+ interneurons, as has been previously suggested for cerebellar Purkinje cells<sup>224</sup> and SI layer V pyramidal cells.<sup>225</sup>

Low-order axonal branches of PV+ interneurons contain myelinated and unmyelinated segments interspersed with branch points. Notably, we observed a correlation between the inter-branch distance and the probability of that segment being myelinated, in which axonal segments connecting branch points in close proximity were less likely to contain internodes. Given that the observed minimum internode length is ~10  $\mu\text{m}$ , there appears to be a critical threshold distance of uninterrupted axon required for an internode to be stably established, beyond which shorter axonal segments remain unmyelinated. Notably, this mechanism could also account for the high proportion of PV+ interneurons that have their first internode located proximal to the first axonal branch point.

The functional significance of cerebral cortex interneuron myelination remains at present largely unknown. Considering that mouse cerebral cortex PV+ interneurons exhibit a total axonal length of ~20 to 30 mm<sup>47</sup> (see also [Supplementary Fig 3.4c](#)), only ~1-2% of the total axonal length is myelinated. Notably however, the proximally biased distribution of internodes along PV+ interneuron axons observed consistently in both mouse and human might be an efficient mechanism to ensure that a high proportion of APs pass through myelinated segments, thereby potentially enhancing conduction velocity, fidelity and metabolic support. In addition, the most distally located internodes were nearly always followed by morphological evidence of en-passant boutons, raising the question of whether myelination is functionally related to the establishment and/or maintenance of boutons. Therefore, we examined myelin-deficient *Shiverer* mice and indeed found that in the absence of myelin, the proximal axon exhibited a higher density and proximally ectopic localization of en-passant boutons. Accordingly, PV+ interneuron axonal myelination might function in part to inhibit synapse formation along the proximal axon. By limiting synapse formation on the proximal axon, myelination could facilitate PV+ interneurons in achieving synchronous inhibition of their postsynaptic targets, given that *en passant* boutons have been suggested to attenuate axonal conduction velocity.<sup>223</sup> Therefore, in addition to facilitating action potential propagation through the classical mechanisms

mediated by increased axonal diameter and membrane resistance, myelin may also function to enhance conduction velocity by limiting synapse formation along the proximal axon.

Compared to glutamatergic pyramidal neurons, the relatively short conduction delays observed in PV+ interneurons are thought to result from their faster membrane time constant, lower AP threshold, and small aspiny dendritic morphology.<sup>47,226–230</sup> Moreover, PV+ interneurons are highly energy demanding<sup>205</sup>, for which myelin provides axonal metabolic support.<sup>36–38</sup> However, more distal myelination of PV+ interneurons might be limited by the apparently strict biophysical threshold of a minimum caliber (~300 nm) for oligodendrocytes to successfully ensheath axonal segments. Spatially-restricted proximal myelination of fast-spiking PV+ interneurons might therefore be an efficient mechanism to enhance conduction velocity, AP fidelity and metabolic support, while also limiting the formation of lower conductivity *en passant* synapses, together in the service of coordinating rapid, temporally-synchronous GABA release across the entire axonal tree.

An interesting outstanding question is whether direct synaptic contacts from PV+ interneurons onto oligodendrocyte precursor cells regulate interneuron myelination<sup>194</sup>, and how their intercellular interactions during early waves of neural migration might shape interneuron myelination.<sup>231</sup> Especially interesting is the possible relevance of how the distance-dependence of the contact between oligodendrocyte progenitor cells and PV+ interneurons<sup>194</sup> might be related to the proximally-biased topography of PV+ interneuron myelination. Moreover, the recent demonstration of a wide diversity of myelinating oligodendrocyte subtypes classified by single-cell RNA sequencing raises the question of whether individual oligodendrocytes have constraints in the repertoire of neuronal cell types that they are capable of ensheathing.<sup>232</sup> Furthermore, recent studies demonstrating that axonal myelination of pyramidal neurons is highly dynamic and experience-dependent<sup>208</sup> also raise the question of the extent to which interneuron myelination has similar, or perhaps distinct, mechanisms of developmental and experience-dependent plasticity.

Using acute surgically resected tissue, we also confirmed that interneuron myelination extends to the human neocortex, with quantitative parameters largely similar to mouse neocortex. This is particularly notable given that our findings might have been influenced by factors not present in rodent studies, such as advanced age, confounding by surgical indication, or medication. Given the putative role of both GABAergic interneurons and myelination in disorders of the brain, the confirmation of PV+ interneuron myelination in the human neocortex provides additional support for its potential pathophysiological relevance.

In summary, we find that PV+ interneurons in the mouse and human cerebral cortex are frequently myelinated. Internodes along PV+ interneuron axons have

a spatially-biased proximal topography, are correlated with axonal morphology, and exhibit quantitative differences between cortical subregions. Moreover, we demonstrate that in the absence of myelin, PV<sup>+</sup> interneurons acquire a higher density and ectopic localization of *en passant* boutons. Together, these findings suggest that myelination is an important feature governing the function of cerebral cortex interneurons.

## Methods

### Mice

All experiments were approved by the Dutch Ethical Committee and in accordance with the Institutional Animal Care and Use Committee (IACUC) guidelines. All mouse lines were obtained from Jackson Laboratory:

Pvalb <sup>tm1(cre)Arbr</sup> /J mice (PV::cre) <sup>233</sup>	strain #008069
Sst <sup>tm2.1(cre)Zjh</sup> /J (SOM::cre) <sup>234</sup>	strain #013044
Gad2 <sup>tm2(cre)Zjh</sup> /J (GAD2::cre) <sup>235</sup>	strain #010802
Gt(ROSA)26Sor <sup>tm14(CAG-tdTomato)Hze</sup> /J (Ai14) <sup>235</sup>	strain #007908
B6;C3Fe.SWV-Mbp <sup>shi</sup> /J ( <i>Shiverer</i> ) <sup>236</sup>	strain #001428
C57BL/6J (WT)	strain #000664

All lines were backcrossed for more than 10 generations in C57BL/6J. Lines were crossed to obtain heterozygous PV::cre x heterozygous Ai14 (PV::cre;Ai14), SOM::cre x Ai14 (SOM::cre;Ai14) and GAD2::cre x Ai14 mice (GAD2::cre;Ai14). Heterozygous B6;C3Fe.SWV-Mbp<sup>shi</sup> mice were crossed to obtain homozygous and heterozygous *Shiverer* mice and wildtype littermates. For global myelination quantifications and viral labeling, mice were used from 8 to 12 weeks of age. For electrophysiological recordings, mice were used from 5 to 8 weeks of age. Mice were group-housed and maintained on a 12 h light/dark cycle with *ad libitum* access to food and water. All experiments were approved by the Dutch Ethical Committee and in accordance with the Institutional Animal Care and Use Committee (IACUC) guidelines.

### Human Brain Tissue

Neocortical tissue was obtained from 3 patients undergoing tumor resection surgery at the Department of Neurosurgery (Erasmus University Medical Center, Rotterdam, The Netherlands). All procedures regarding human tissue were performed with the approval of the Medical Ethical Committee of the Erasmus University Medical Center. Written informed consent of each patient was provided in accordance with the Helsinki Declaration.

Patient #1 was a 54-year old female presenting with a WHO grade 4 glioblastoma in the right temporo-occipital lobe. She had no significant psychiatric or past medical history, and no history of epilepsy or seizures. Patient received no anti-epileptic or cytostatic medication.

Patient #2 was a 69-year old male presenting with a hemangiopericytoma/solitary fibrous tumor on the posterior border of the left ventricle. He had no significant psychiatric or past medical history, and no history of epilepsy or seizures. Patient received no anti-epileptic or cytostatic medication.

Patient #3 was a 59-year old male presenting with a WHO grade 4 glioblastoma in the right temporal lobe. His psychiatric history was notably only for a single episode of depression which fully remitted. He had no history of epilepsy, but experienced a single tonic-clonic seizure 3 weeks prior to surgery, for which he was treated with sodium valproate (1000 mg daily). Patient received no cytostatic medication.

## **Mouse Viral Labeling**

Heterozygous PV::cre mice were used for viral-mediated cell-type specific labelling, which was performed using cre-dependent adeno-associated virus (AAV) expression with AAV5/EF1a-DIO-mCherry or AAV5/Flex-eGFP (University of Pennsylvania Viral Vector Core). Virus was diluted to  $\sim 5 \times 10^{11}$  GC/ml in phosphate-buffered saline (PBS) to achieve sparse labelling.

Anesthesia was induced using 5% isoflurane, and subsequently maintained with 2% isoflurane during surgery. Body temperature was maintained at 37°C. Bupivacaine hydrochloride (2.5 mg/ml), Rimadyl (50 mg/ml), and Temgesic (0.3 mg/ml) were administered subcutaneously. Mice were placed into the stereotaxic frame (Stoelting) using stub ear bars for head fixation. Longitudinal scalp incision of 1-2 cm length was made to reveal the skull, and a craniotomy was performed overlying the site of injection at the following coordinates (in mm):

mPFC: +2 bregma, 0.5 lateral, 2 vertical

SI: -1 bregma, 2 lateral, 0.5 vertical

CA1: -1.5 bregma, 1 lateral, 1.5 vertical

A borosilicate glass micropipette was slowly lowered to the target site and remained in place for 5 min before the start of injection. Virus injection was controlled by a manual syringe pump (0.5  $\mu$ l per location, infusion speed 0.05  $\mu$ l/min). At the conclusion of the injection, the micropipette was maintained in place for another 5 min and then slowly withdrawn. After surgery, mice were allowed to recover for 3-4 weeks before analysis.

## Electrophysiology

### Mouse Recordings

Anesthesia was induced using 5% isoflurane and mice were transcardially perfused with 20 ml of ice-cold, NMDG-based cutting solution containing (in mM): 93 N-methyl-d-glucamine (NMDG), 93 HCl, 30 NaHCO<sub>3</sub>, 25 D-glucose, 20 HEPES, 5 Na-ascorbate, 2 thiourea, 10 MgCl<sub>2</sub>, 3 Na-pyruvate, 2.5 KCl, 1.25 NaH<sub>2</sub>PO<sub>4</sub> and 0.5 CaCl<sub>2</sub> (300 mOsm, pH 7.4) oxygenated with 95% O<sub>2</sub>/5% CO<sub>2</sub> before decapitation. After decapitation, the brain was quickly dissected in the same ice-cold cutting solution. For each brain region examined, coronal slices (300 μm) were cut with a vibrating slicer (Microm HM 650V, Thermo Scientific) and incubated in cutting solution at 37 °C for 30 seconds, followed by oxygenated (95% O<sub>2</sub>/5% CO<sub>2</sub>) artificial cerebrospinal fluid (aCSF) at 37 °C for 45 min. ACSF contained (in mM) 127 NaCl, 25 NaHCO<sub>3</sub>, 25 D-glucose, 2.5 KCl, 1.25 NaH<sub>2</sub>PO<sub>4</sub>, 1.5 MgSO<sub>4</sub> and 1.6 CaCl<sub>2</sub>. Slices were then allowed to recover at room temperature for at least 1 h before recordings.

In *Shiverer* and wildtype mice, interneurons were visualized using infrared differential interference contrast microscopy. In PV::cre;Ai14 mice, PV+ interneurons were visualized by native tdTomato fluorescence using an RFP filter (Semrock, Rochester, NY, USA). Whole-cell recordings were made using borosilicate glass pipettes (3.5–5.5 MΩ resistance) with intracellular solution containing (in mM) 120 K-gluconate, 10 KCl, 10 HEPES, 10 K-phosphocreatine, 4 ATP-Mg, 0.4 GTP, and 5 mg/ml biocytin (pH was adjusted to 7.4 using KOH, and osmolarity measured 285–290 mOsm).

Recordings were performed in aCSF at near-physiological temperatures (32–33 °C) using HEKA EPC10 quattro amplifiers and Patchmaster software (40 or 200 kHz sampling rates depending on the total recording length to avoid memory limits during acquisition). Series resistance was typically <25 MΩ and fully compensated for bridge balance and capacitance; recordings in which the series resistance exceeded 25 MΩ were not included in the pooled averages. No correction was made for liquid junction potential. Data analysis was performed offline using Igor Pro v6 (Wavemetrics).

Basic physiological characteristics were determined from voltage responses to square-wave current pulses of 500 ms duration, ranging from –100 pA to +300 pA, and delivered in 20 pA intervals. Input resistance was determined by the slope of the linear regression through the voltage-current curve. Single action potential (AP) characteristics were obtained from the first elicited action potential. AP threshold was defined as the inflection point at the foot of the regenerative upstroke. AP amplitude was defined as the voltage difference between the threshold and peak voltage. AP

half-width was measured at half of the peak amplitude. AP rise time was quantified as duration from 10% to 90% of the peak amplitude. The fast after-hyperpolarizing potential (fAHP) was measured as the peak hyperpolarizing deflection following AP initiation. AP frequency was determined from a 500 ms square-wave current pulse of +300 pA.

## **Human Recordings**

*Ex vivo* recordings of human neocortex were performed using tissue requiring surgical resection in order to access the location of the tumor. Immediately following resection, the neocortical tissue block was directly transferred to oxygenated (95% O<sub>2</sub>/5% CO<sub>2</sub>) ice-cold cutting solution and transported to the electrophysiology laboratory. The time between tissue resection and slicing was always <10 min. Tissue slices were used for electrophysiological recordings only when no infiltrating tumor cells were detectable in the slice. Whole-cell recordings and electrophysiological analyses were performed identically similar to mouse tissue.

In total, we recorded from 20 cells (patient #1: 4 cells; patient #2: 14 cells; patient #3: 4 cells), of which 13 cells (65%; (patient #1: 3 cells; patient #2: 8 cells; patient #3: 2 cells) were successfully biocytin-filled and reconstructed.

## **Fluorescence Immunohistochemistry**

### **Mouse Tissue**

Deep anesthesia was induced by intraperitoneal injection of pentobarbital, and mice were transcardially perfused with saline followed by 4% paraformaldehyde (PFA). Brains were dissected and post-fixed in 4% PFA for 2 h at room temperature. Brains were transferred into 10% sucrose phosphate buffer (PB 0.1 M, pH 7.3) and stored overnight at 4°C. Embedding was performed in a 12% gelatin/10% sucrose block, with fixation in 10% paraformaldehyde/30% sucrose solution (PB 0.1 M, pH 7.3) for 2 h at room temperature and immersed in 30% sucrose (PB 0.1 M, pH 7.3) at 4°C overnight. Forty micrometer coronal and sagittal sections were collected serially (rostral to caudal) using a freezing microtome (Leica, Wetzlar, Germany; SM 2000R) and stored in 0.1 M PB. Free-floating sections were incubated in sodium citrate (10 mM) at 80 °C for 30 min and rinsed with PBS (pH 7.3). Sections were pre-incubated with a blocking PBS buffer containing 0.5% Triton X-100 and 10% normal horse serum (NHS; Invitrogen, Bleiswijk, The Netherlands) for 1 h at room temperature. Sections were incubated in a mixture of primary antibodies in PBS buffer containing 0.4% Triton X-100 and 2% NHS for 72 h at 4°C.

The following primary antibodies were used: rabbit anti-mCherry (1:500, Millipore, Abcam, ab167453), mouse anti-PV (1:1000, Swant, 235), and goat anti-MBP (1:300, Santa Cruz, C-16, sc-13914). We additionally confirmed the specificity of the anti-MBP antibody using both western blot analysis and immunofluorescence labeling in tissue from MBP-deficient *Shiverer* mice (Supplementary Fig. 3.9).

For recovery of biocytin-labelled cells following electrophysiological recordings, slices were incubated overnight at 4°C in 4% PFA. Slices were then rinsed at room temperature in 0.1 M PB, incubated for 12 h at 4°C in 10% sucrose (0.1 M PB), and overnight at 4°C in 30% sucrose (0.1 M PB). Sections were serially recut at 40 µm using a freezing microtome (Leica, Wetzlar, Germany; SM 2000R) and stored in 0.1 M PB at 4°C.

Sections were washed with PBS, and incubated with corresponding Alexa-conjugated secondary antibodies (1:300, Invitrogen) and cyanine dyes (1:300, Sanbio, Uden, The Netherlands) in PBS buffer containing 0.4% Triton X-100, 2% NHS for 2 h at room temperature. For biocytin-labelled cells, streptavidin-A488 (1:300, Jackson) was used. For some experiments, nuclear staining was performed using DAPI (1:10.000, Invitrogen). Sections were washed with PB 0.1 M and mounted on slides, cover slipped with Vectashield H1000 fluorescent mounting medium (Vector Labs, Peterborough, UK) and sealed.

## Human Tissue

Three-hundred µm electrophysiology slices were incubated overnight at 4°C in 4% PFA. Slices were then rinsed at room temperature in 0.1 M PB, incubated for 12 h at 4°C in 10% sucrose (0.1 M PB), and overnight at 4°C in 30% sucrose (0.1 M PB). Forty µm sections were collected serially using a freezing microtome (Leica, Wetzlar, Germany; SM 2000R) and stored in 0.1 M PB. Sections were extensively washed and pre-incubated with a blocking PBS buffer containing 0.5% Triton X-100 and 5% bovine serum albumin (BSA; Sigma-Aldrich, The Netherlands) for 1 h at room temperature. Next, sections were incubated in a mixture of primary antibodies in PBS buffer containing 0.5% Triton X-100 and 1% BSA for 72h at 4°C. The following primary antibodies were used: mouse anti-PV (1:1000, Sigma, P3088, clone Parv-19) and goat anti-MBP (1:300, Santa Cruz, C-16, sc-13914).

Sections were extensively washed with PBS (>2 h), and incubated with corresponding Alexa-conjugated secondary antibodies (1:300, Invitrogen), cyanine dyes (1:300, Sanbio, Uden, The Netherlands) and streptavidin-A488 (1:300, Jackson) in PBS buffer containing 0.5% Triton X-100 and 1% BSA for 5 h at room temperature. Nuclear staining was performed using DAPI (1:10.000, Invitrogen, Bleiswijk). Sections were washed with PB 0.1 M and mounted on slides, cover slipped with Vectashield H1000 fluorescent mounting medium (Vector Labs, Peterborough, UK) and sealed.

## Confocal Imaging and Analysis

Confocal imaging was performed using a Zeiss LSM 700 microscope (Carl Zeiss) equipped with Plan-Apochromat 10x/0.45 and 63x/1.4 (oil immersion) objectives. Alexa488, Cy3, Alexa647, and Alexa405 or DAPI were imaged using excitation wavelengths of 488, 555, 639 and 405nm, respectively.

Quantification of region-dependent myelination was performed in the prelimbic region of the mPFC (bregma: +2.10 till +1.54 mm), somatosensory cortex layers (bregma: -0.82 till -1.22 mm) and dorsal hippocampal CA1 (bregma: -1.58 till -1.94 mm) by obtaining z-stack images (1064 x 1064 pixels) at 63x magnification (1.4 NA; oil immersion) with 1x digital zoom at a step size of 1  $\mu$ m. Stacks were randomly sampled across all layers of mPFC, somatosensory cortex and hippocampal CA1 based on DAPI nuclear labeling, using a 100 x 100  $\mu$ m counting frame. Immunofluorescent co-localization of MBP and tdTomato was manually-counted by two independent raters (J. S. and D. B.) using NIH ImageJ (version 1.41). Co-localization was defined as the circumferential bordering of a tdTomato-labelled axon by an MBP<sup>+</sup> myelin signal. At least three z-stacks were analysed per mouse per region per layer.

Analogous to previous reports<sup>43,237,238</sup>, a small fraction of cells in the SOM::cre;Ai14 mice (~10%) had expression of PV in medial prefrontal and somatosensory cortex. Due to the difficulty in performing axonal triple co-localizations (MBP/SOM/PV), and the bona fide endogenous co-expression of PV and SOM in hippocampal bistratified and oriens-lacunosum moleculare cells<sup>239</sup>, we have reported the corresponding double co-localizations (MBP/SOM and MBP/PV). The MBP/SOM double co-localizations reported in Fig. 3.1 therefore likely represent an minor overestimation of the actual frequency of SOM<sup>+</sup> interneuron axonal myelination.

For analysis of myelination along virus-labelled PV<sup>+</sup> axons, overview images were obtained at 10x with 1x digital zoom. Individual labelled cells distributed over layers LII-LVI in mPFC and SI, and dorsal hippocampal CA1 stratum oriens, pyramidale and radiatum were categorized and examined at 63x with 1x digital zoom to confirm labelling with the PV antibody. Confocal z-stack images (2128 x 2128 pixels) were obtained at 63x magnification with 1x digital zoom at a step size of 2  $\mu$ m along the full z-axis extent of the section. Axons were identified as the thinnest, smoothest, and most highly branched processes originating from either the soma or primary dendrite. In addition, axons seemed to branch at more obtuse  $\geq 90^\circ$  angles from one another, often turning back toward the soma, whereas dendrites branched at smaller angles ( $< 90^\circ$ ), continuing a trajectory away from the soma. PV<sup>+</sup> cells were considered to be myelinated when they exhibited at least one myelinated internode. If the axon exited the slice before 50  $\mu$ m, cells were excluded from further analysis.

Axonal reconstructions of mouse and human biocytin-filled cells were obtained at 63x magnification (5320 x 5320 pixels) with 1x digital zoom and a step size of 0.5  $\mu\text{m}$ . Pixel dwell was kept at  $>1.5 \mu\text{s}$  for optimal subsequent co-localization identification. Images were transferred to NeuroLucida 360 software (v2.6; MBF Bioscience) and reconstructed using interactive tracing with the Directional Kernels method. Reconstructed soma, axon and myelin segments were analyzed with NeuroLucida Explorer (MBF Bioscience).

The distance to first myelin was defined as the distance along the axon from the soma, or in the case of dendrite-originating axons the distance from the originating dendrite, to the initial point of MBP immunofluorescence. Myelin segments that exited a slice were removed from subsequent analysis. Identification and reconstruction of axonal myelination was performed blind to electrophysiological (fast-spiking versus non-fast-spiking) and cell-type (PV+ versus non-PV) identity. No spatial corrections were made for tissue shrinkage.

### **Structured Illumination Microscopy (SIM)**

Imaging was performed using a Zeiss Elyra PS1 system. 3D-SIM data was acquired using a 63x 1.4NA oil objective. 488, 561 and 642 100mW diode lasers were used to excite the fluorophores together with respectively a BP 495-575 + LP 750, BP 570-650 + LP 75 or LP 655 emission filter. For 3D-SIM imaging, a grating was present in the light path, and modulated in 5 phases and 5 rotations, and multiple z-slices with an interval of 110 nm were recorded on an Andor iXon DU 885, 1002x1004 EMCCD camera. Raw images were reconstructed using Zen (Zeiss).

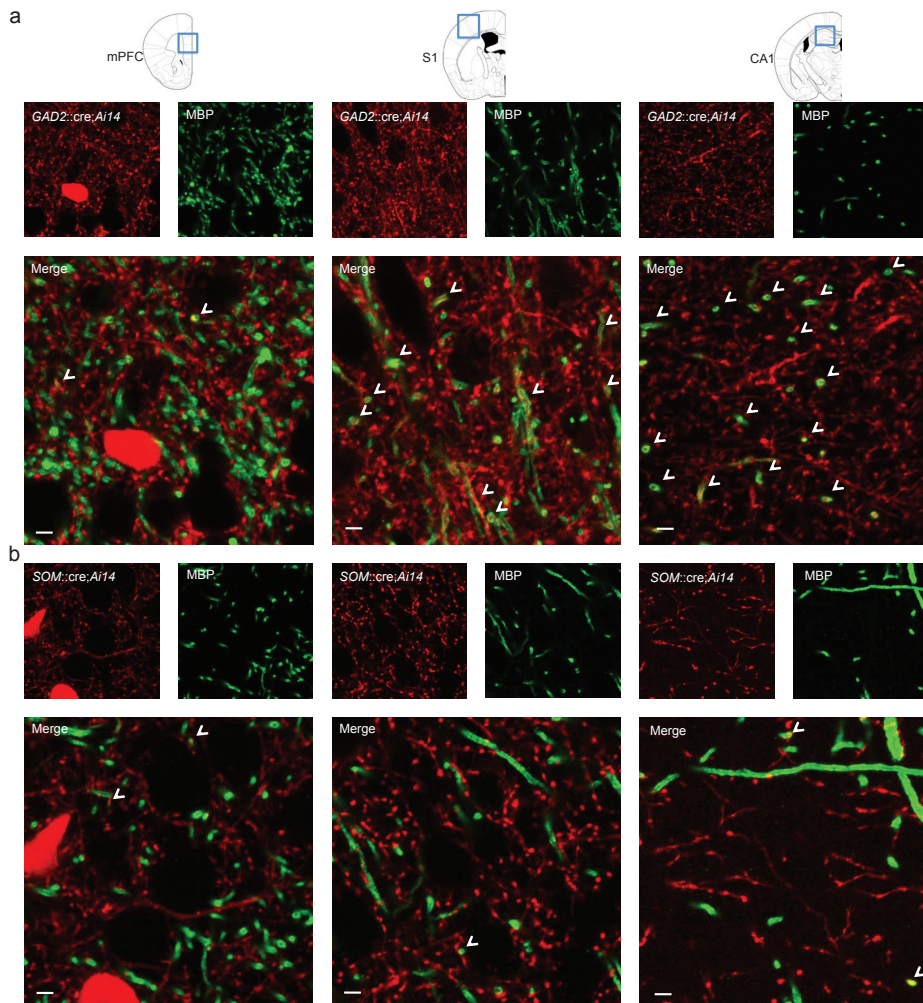
For axonal bouton quantifications, SIM images were obtained from proximal axons of biocytin-filled cells up till the 3rd branch order. *En passant* bouton density, as well as proximal axonal lengths were quantified using NeuroLucida 360 (v2.6; MBF Bioscience).

### **Western Blotting**

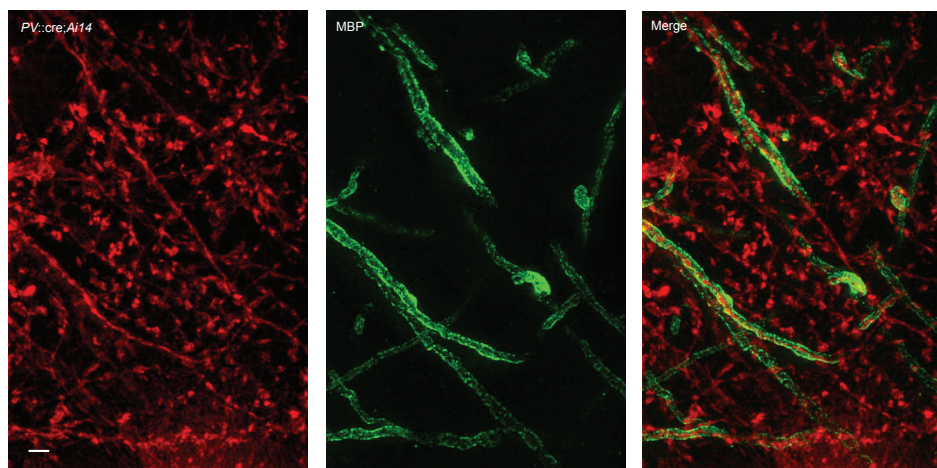
Adult homozygous Shiverer mice and WT littermates were anesthetized using isoflurane, sacrificed by decapitation, and snap frozen in liquid nitrogen. Protein lysates were prepared by homogenization of cortical brain samples in lysis buffer (10 mM Tris-HCL pH 6.8, 2.5% SDS, 2 mM EDTA) and adjusted to a concentration of 1 mg/ml. Western blots were probed with primary antibodies against MBP (C-16, sc-13914, 1:500, Santa Cruz) and beta-actin (MAB1501R, 1:10000, Chemicon), and complementary secondary antibodies (goat anti-mouse and donkey anti-goat, 1:5000, AffiniPure). Blots were imaged using a LI-COR Odyssey Scanner with Odyssey 3.0 software.

## Statistical Analysis

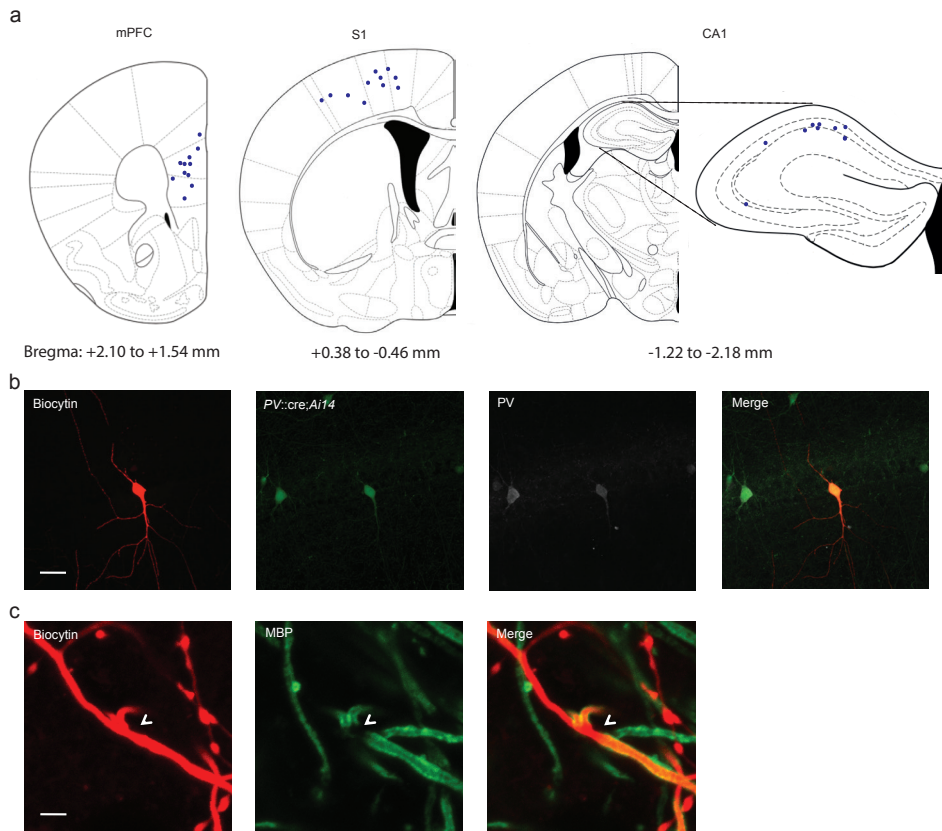
Statistical analysis was performed using IBM SPSS (version 21). Sample sizes were chosen based on previous publications utilizing similar methods. Hypothesis testing was performed using unpaired two-tailed Student's *t*-test or analysis of variance (ANOVA) followed by Tukey's *post hoc* test. All data are expressed as mean  $\pm$  standard error. Significance threshold was set at  $P < 0.05$ . Throughout the paper exact *P*-values values are provided except when  $P < 0.001$ .



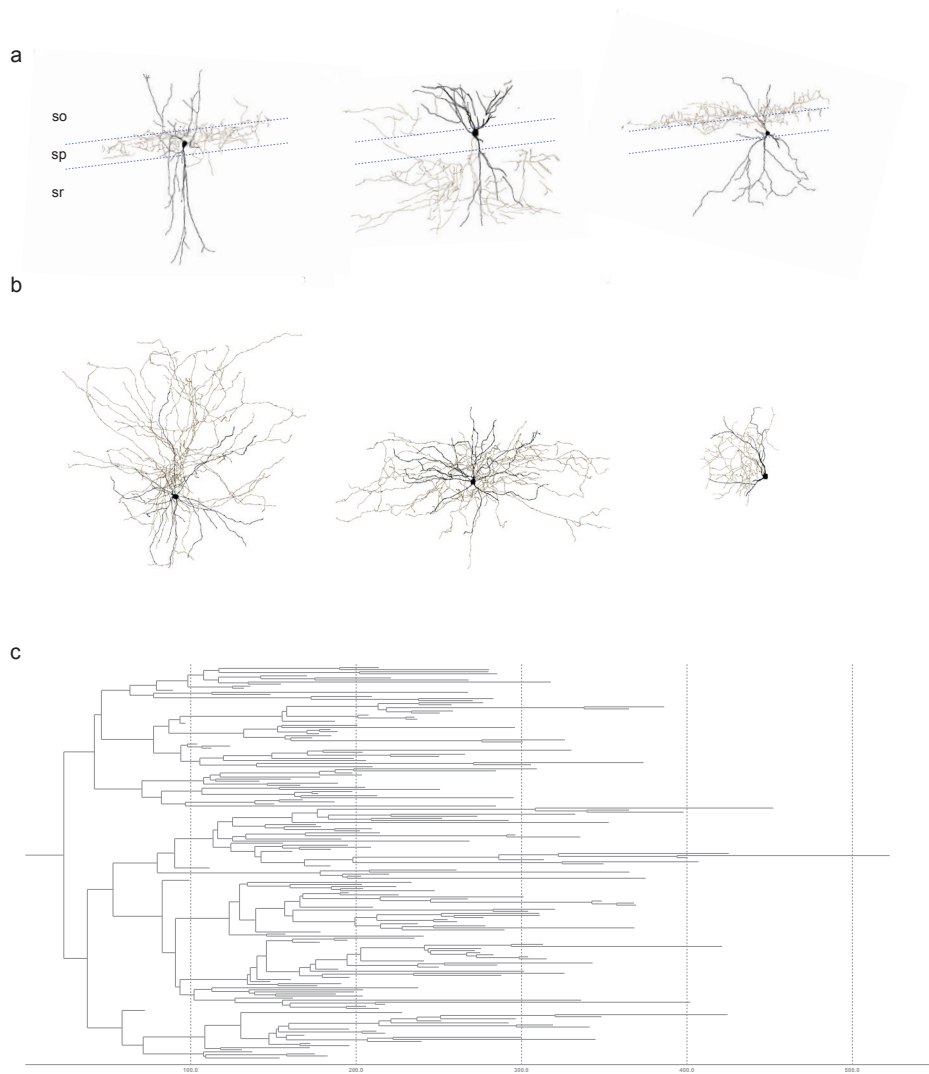
**Supplementary Figure 3.1.** Cell type-specific interneuron myelination. (a) Representative co-localization (arrowheads) between GAD2::cre;Ai14 (red) and MBP (green) in each respective brain region. Scale bars are 5  $\mu$ m. (b) Representative co-localization (arrowheads) between SOM::cre;Ai14 (red) and MBP (green) in each respective brain region. Scale bars are 5  $\mu$ m.



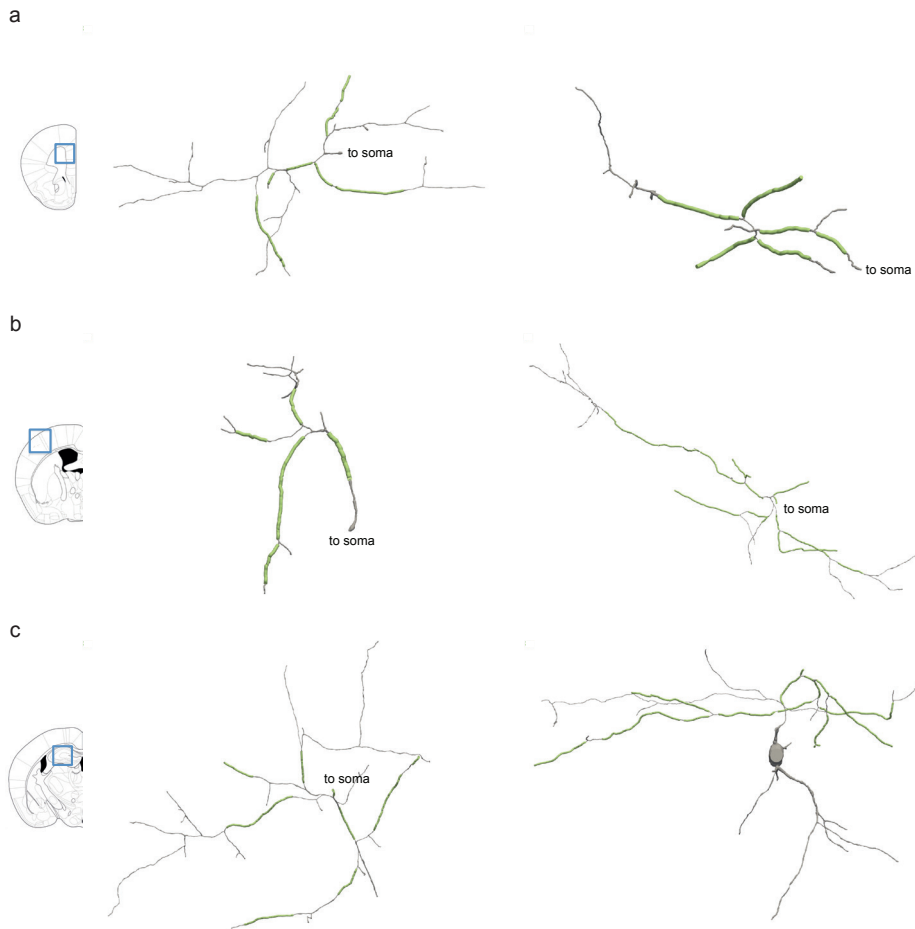
**Supplementary Figure 3.2.** PV<sup>+</sup> interneuron myelination. High-resolution maximum projection SIM image demonstrating PV::cre;Ai14-labeled axons (red) co-localized with MBP (green) in layer II-III of S1. Scale bar, 1  $\mu$ m.



**Supplementary Figure 3.3.** Single-cell reconstructions. **(a)** Location of biocytin-labeled cells are illustrated with black circles in mPFC ( $n = 11$  cells), S1 ( $n = 11$  cells), and hippocampus ( $n = 9$  cells). Coordinates delineate the rostrocaudal extent of recorded cells (Paxinos and Franklin 2001). Note that some cells in each region fall outside strict regional boundaries. **(b)** Confocal images of triple co-localizations of biocytin (red), PV::cre;Ai14 (green) and PV (grey) in a hippocampal fast-spiking interneuron from CA1 stratum pyramidale. Scale bar; 50  $\mu\text{m}$ . **(c)** Confocal image of co-localization of biocytin (red) and MBP (green), showing an unmyelinated branch point (arrowhead). Scale bar; 2  $\mu\text{m}$ .

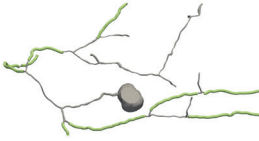


**Supplementary Figure 3.4.** Reconstructions showing representative examples of distinct morphological subtypes of fast-spiking PV+ interneurons. **(a)** Hippocampal CA1 subtypes showing a classical basket cell with its axon restricted to pyramidal cell layer (left), a bistratified cell with its axon projecting to both stratum oriens and stratum radiatum (middle), and a chandelier cell (right), showing typical perpendicular bouton cartridges. **(b)** Cortical subtypes showing a classic basket cell (left), horizontally-elongated cell (HEC, middle), and shrub cell (right). All subtypes exhibited myelination. Soma and dendrite in black, axon in brown. **(c)** Dendrogram of a full axonal reconstruction from a mPFC layer V basket cell, exemplifying total axonal length. Axon in grey. Horizontal axis,  $\mu\text{m}$ . SO Stratum oriens; SP Stratum pyramidale; SR Stratum radiatum.

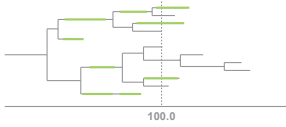


**Supplementary Figure 3.5.** Additional examples of mouse PV<sup>+</sup> axonal myelination. (a-c) Reconstructions of representative axonal segments from two independent fast-spiking PV<sup>+</sup> cells in mPFC (a), S1 (b), and dorsal CA1 (c). Note the myelinated segments interspersed with axonal branch points, often with relatively shorter intervening unmyelinated segments. Branches that lead towards the soma are indicated.

a



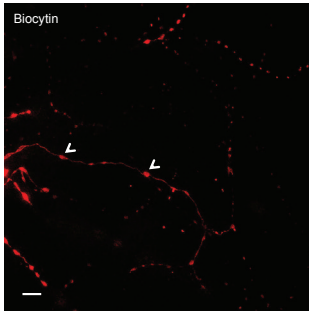
b



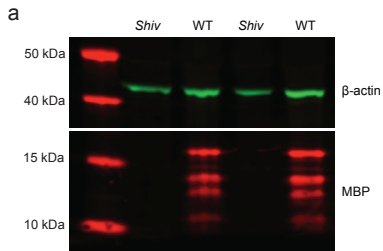
**Supplementary Figure 3.6.** Rare example of PV+ interneuron (mPFC) with an onset of myelination beyond first-order branches. Occasionally, myelin onset occurs beyond the first branch point, and rarely beyond the second branch point, as depicted here. Reconstruction in (a) and dendrogram in (b). Notice the unusual proximal first branch point at  $\sim 20 \mu\text{m}$  from the soma. Soma and axon in grey, myelin in green. Horizontal axis,  $\mu\text{m}$ .



**Supplementary Figure 3.7.** Additional examples of human fast-spiking interneuron axonal myelination. **(a)** Human fast-spiking interneuron with extensive myelination of the primary axon but predominantly unmyelinated secondary branches. Note the axonal branching before onset of myelination. **(b)** Myelinated axons of human fast-spiking interneuron with large unmyelinated segments ( $\sim 50\text{-}70\ \mu\text{m}$ ) in between myelinated segments. Branches leading back to the soma are indicated. Soma and axon are shown in grey, and myelinated internodes are shown in green.



**Supplementary Figure 3.8.** High-resolution maximum projection SIM image of the biocytin-filled axon (red) taken from the only unmyelinated PV+ interneuron identified in the experiment shown in Fig. 3.2. Notably, in the absence of myelination, *en passant* boutons are found on the proximal axon (arrowheads). Scale bar, 10  $\mu$ m.



**Supplementary Figure 3.9.** *Shiverer* mice lack all isoforms of MBP. (a) Western blot probed with the MBP antibody confirmed the absence of all MBP isoforms (red) in cortical lysates from *Shiverer* (Shiv) mice.  $\beta$ -actin (green) is shown as loading control.

	<b>mPFC</b>	<i>n</i> = 11	<b>SI</b>	<i>n</i> = 11	<b>CAI</b>	<i>n</i> = 9
	<b>Average</b>	<b>s.e.</b>	<b>Average</b>	<b>s.e.</b>	<b>Average</b>	<b>s.e.</b>
RMP (mV)	-71.87	1.13	-70.49	1.45	-68.66	1.55
Ri (M $\Omega$ )	125.44	11.84	93.61	7.75	116.38	13.81
AP Threshold (mV)	-36.90	2.94	-37.78	1.65	-40.13	1.70
AP Amplitude (mV)	81.24	2.69	87.32	1.66	98.10	2.85
AP Frequency (Hz)	124.18	9.57	111.82	12.44	90.44	9.72
AP HalfWidth (ms)	0.37	0.02	0.27	0.01	0.28	0.01
AP RiseTime (ms)	0.19	0.01	0.14	0.00	0.16	0.01
fAHP Amplitude (mV)	-21.45	0.85	-20.37	0.75	-18.79	1.33

**Supplementary Table 3.1.** Passive membrane properties and single AP characteristics of fast-spiking PV+ interneurons from mouse mPFC, SI, and CAI. AP frequency was quantified as the mean AP frequency during a 500 ms, 300 pA square-wave current pulse. AP, action potential. fAHP, fast after-hyperpolarization. Ri, input resistance. RMP, resting membrane potential.

<b>Internode Length (<math>\mu</math>m)</b>	<b>Ex vivo Biocytin Labeling</b>	<b>In vivo Viral Labeling</b>		<b>P</b>	
	<b>Average</b>	<b>s.e.</b>	<b>Average</b>		<b>s.e.</b>
mPFC	23.3	1.5	22.7	1.9	0.811
SI	26.0	1.1	27.5	4.3	0.627
CAI	33.7	2.4	32.0	4.2	0.733

**Supplementary Table 3.2.** Methodological comparison of internode length between genetically-encoded viral labeling and intracellular biocytin labeling. *P*-values are based on Student's *t*-test.

	<b>Non-Fast-Spiking</b>	<i>n</i> = 3	<b>Fast-Spiking</b>	<i>n</i> = 10	<i>P</i>
	<b>Average</b>	<b>s.e.</b>	<b>Average</b>	<b>s.e.</b>	
RMP (mV)	-64.35	4.42	-64.78	2.07	0.923
Ri (M $\Omega$ )	238.30	99.19	151.10	20.67	0.187
AP Threshold (mV)	-36.70	2.74	-40.30	1.48	0.268
AP Amplitude (mV)	86.80	1.63	92.93	2.67	0.254
AP Frequency (Hz)	54.67	5.82	121.60	12.32	0.015
AP HalfWidth (ms)	0.73	0.22	0.30	0.01	0.002
AP RiseTime (ms)	0.79	0.34	0.52	0.13	0.381
fAHP Amplitude (mV)	-24.00	4.76	-23.12	0.76	0.751

**Supplementary Table 3.3.** Passive membrane properties and single AP characteristics of non-fast-spiking and fast-spiking human interneurons. AP frequency was quantified as the mean AP frequency during a 500 ms, 300 pA square-wave current pulse. AP, action potential. fAHP, fast after-hyperpolarization. Ri, input resistance. RMP, resting membrane potential. P-values are based on Student's t-test.





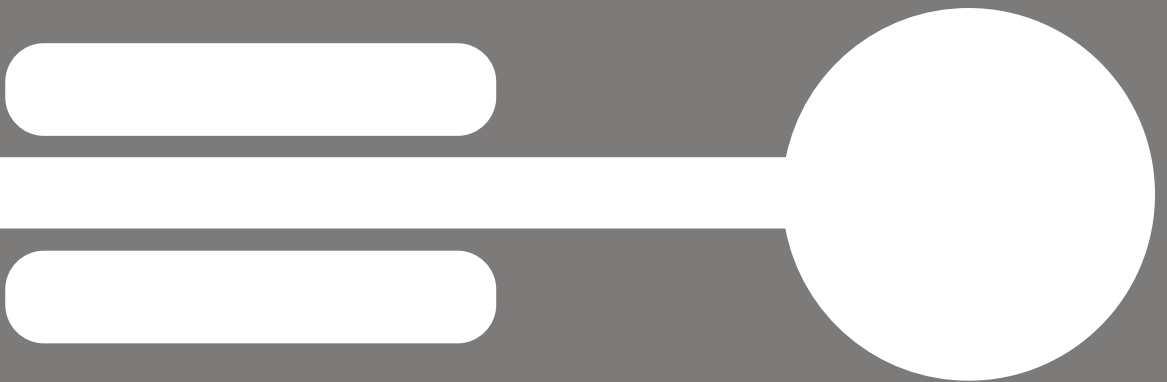
# Activity-Dependent Myelination of Parvalbumin Interneurons mediated by Axonal Morphological Plasticity

## Chapter 4

J. Stedehouder<sup>1\*</sup>, D. Brizee<sup>1\*</sup>, G. Shpak<sup>1</sup>, S.A. Kushner<sup>1</sup>

1. Department of Psychiatry, Erasmus MC Rotterdam, The Netherlands

\*These authors contributed equally



## Abstract

Axonal myelination of neocortical pyramidal neurons is dynamically modulated by neuronal activity. Recent studies have shown that a substantial proportion of neocortical myelin content is contributed by fast-spiking, parvalbumin (PV)-positive interneurons. However, it remains unknown whether the myelination of PV+ interneurons is also modulated by intrinsic activity. Here, we utilized cell-type specific Designer Receptors Exclusively Activated by Designer Drugs (DREADDs) in adult male and female mice to activate a sparse population of medial prefrontal cortex PV+ interneurons. Using single-cell axonal reconstructions, we find that DREADD-stimulated PV+ interneurons exhibit a nearly two-fold increase in total length of myelination, predominantly mediated by a parallel increase of axonal arborization and number of internodes. In contrast, the distribution of axonal inter-branch segment distance and myelin internode length were not significantly altered. Topographical analysis revealed that myelination of DREADD-stimulated cells extended to higher axonal branch orders, while retaining a similar inter-branch distance threshold for myelination. Together, our results demonstrate that chemogenetically-induced neuronal activity increases the myelination of neocortical PV+ interneurons mediated at least in part by an elaboration of their axonal morphology.

## Introduction

Myelination functions critically to enable complex neuronal function, including learning and cognition. Recent studies have shown that a substantial fraction of myelination in the cerebral cortex is localized to fast-spiking, parvalbumin-positive (PV) interneurons.<sup>216,240</sup> PV+ interneuron myelination is topographically-biased towards the proximal axon and constrained by local axonal morphology, including branch points and *en passant* boutons.<sup>240</sup>

In addition, recent studies have shown that myelination is activity-dependent.<sup>25,27</sup> Optogenetic neuronal stimulation selectively increases oligodendrogenesis and myelination in mice<sup>19</sup>, and neuronal activity biases axonal selection and myelin topography in zebrafish<sup>241,242</sup>. Complex motor skill learning requires the production of new oligodendrocytes<sup>33</sup>, monocular deprivation leads to both oligodendrogenesis and reduced internode length<sup>22</sup>, and social isolation negatively influences oligodendrocyte morphological complexity with a concomitant reduction of internode density and g-ratio.<sup>209</sup>

An important outstanding question is whether PV+ interneuron myelination is similarly dependent upon neuronal activity. In the present study, we utilize cell-specific Designer Receptor Exclusively Activated by Designer Drug (DREADD) technology to confirm that activity-dependent myelination extends to PV+ interneurons in the adult brain. Electrophysiological recordings with single cell labeling of manipulated cells permitted the coordinated examination of axonal morphology and myelin topography, revealing an activity-dependent enhancement of PV+ interneuron myelination that could be largely explained by an elaboration of axonal arborization with a parallel increase of internode number.

## Results

### Chemogenetic activation increases parvalbumin interneuron myelination

We utilized *in vivo* cell-specific expression of activating Designer Receptor Exclusively Activated by Designer Drug (DREADD)<sup>243</sup>, followed by *ex vivo* whole-cell electrophysiology and single-cell axonal reconstructions (Fig. 4.1a). Adult PV::cre mice<sup>233</sup> received bilateral stereotactic injections in the medial prefrontal cortex (mPFC), utilizing adeno-associated viruses (AAV) with cre-dependent expression of unilateral hM3Dq-mCherry and contralateral GFP (Fig. 4.1b,c). Four weeks post-transduction, mice were given intraperitoneal administrations of clozapine n-oxide (CNO; 1 mg/kg, twice daily) for 14 consecutive days. Viral transduction was highly specific for PV+ cells with a similarly high cell-type specificity of hM3Dq-

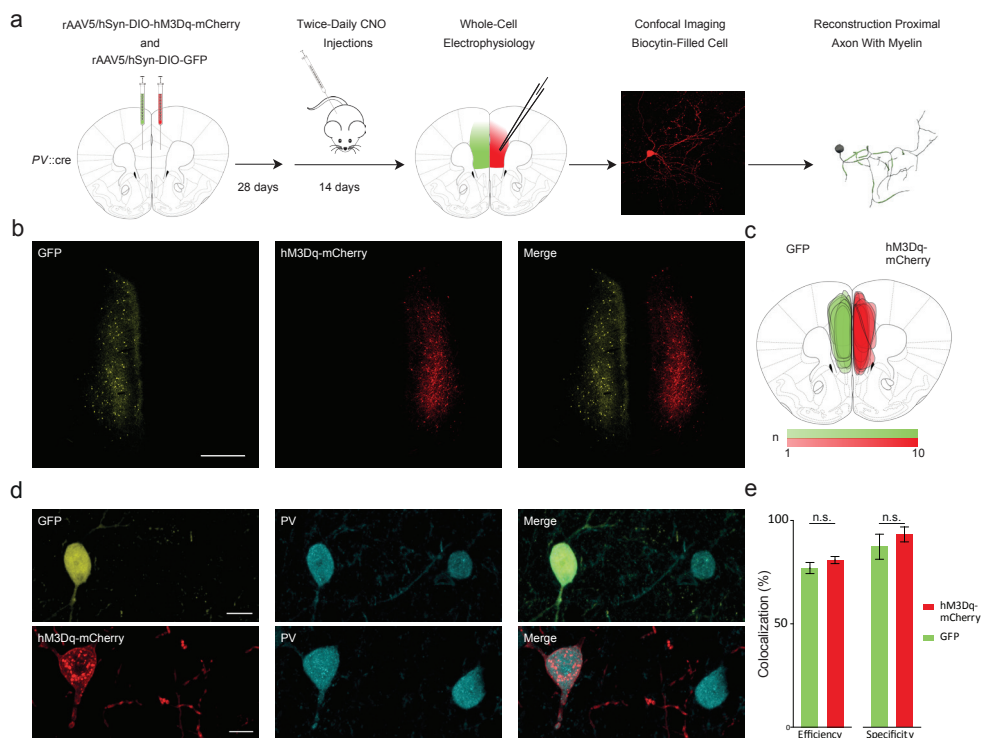


**Figure 4.1.** PV<sup>+</sup> interneuron-specific DREADD expression. (a) Experimental design. Adult PV::cre mice were virally transduced with pseudorandomly assigned unilateral hM3Dq-mCherry and contralateral GFP. Twenty-eight days post-surgery, mice were injected twice daily with 1 mg/kg CNO intraperitoneally for 14 days. One day after the last injection, mice were sacrificed and labeled cells were electrophysiologically recorded in whole-cell configuration. Biocytin-filled cells were imaged and axons were reconstructed including myelination. (b) Representative low-magnification confocal image of a bilateral injection of hM3Dq-mCherry (red) and GFP (yellow) at +2.1 mm from Bregma. Scale bar, 500  $\mu$ m. (c) Schematic projection of injection areas from  $n = 10$  mice for hM3Dq-mCherry (red) and GFP (green), with color intensity indicating number of mice. (d) Top: Maximum projection confocal image of co-localized GFP (yellow) and PV (cyan) immunofluorescence. Scale bar, 10  $\mu$ m. Bottom: Maximum projection confocal image of co-localized hM3Dq-mCherry (red) and PV (cyan) immunofluorescence. Scale bar, 10  $\mu$ m. (e) Quantification of colocalization between hM3Dq-mCherry (red), GFP (green) and PV immunofluorescence. Transduction efficiency was similarly high for both vectors [ $P(\text{GFP}+|\text{PV}+)$ :  $77.0 \pm 2.7\%$ ,  $P(\text{hM3Dq-mCherry}+|\text{PV}+)$ :  $80.9 \pm 1.7\%$ ;  $t_{(3)} = 1.218$ ,  $P = 0.290$ ]. Transduction specificity was also similarly high [ $P(\text{PV}+|\text{GFP}+)$ :  $87.6 \pm 6.1\%$ ,  $P(\text{PV}+|\text{hM3Dq-mCherry}+)$ :  $93.5 \pm 3.6\%$ ;  $t_{(4)} = 0.844$ ,  $P = 0.446$ ].  $n = 3$  mice. Unpaired two-tailed Student's  $t$ -tests in (e). Bars represent mean  $\pm$  s.e.m. n.s. non-significant.

mCherry and GFP vectors (Fig. 4.1d,e). Sixteen hours after the last intraperitoneal CNO injection, *ex vivo* whole-cell recordings with *post hoc* biocytin labeling were performed in hM3Dq-mCherry<sup>+</sup> cells and contralateral GFP<sup>+</sup> cells from mPFC layer V (Fig. 4.2a,b). hM3Dq-mCherry<sup>+</sup> and GFP<sup>+</sup> cells exhibited subthreshold membrane potential oscillations, a suprathreshold high-frequency non-adapting pattern of action potential firing, and a large amplitude fast after-hyperpolarization, consistent with a fast-spiking, PV<sup>+</sup> interneuron identity. No differences were observed between hM3Dq-mCherry<sup>+</sup> and GFP<sup>+</sup> cells in baseline membrane properties or single action potential characteristics (Fig. 4.2c-j).

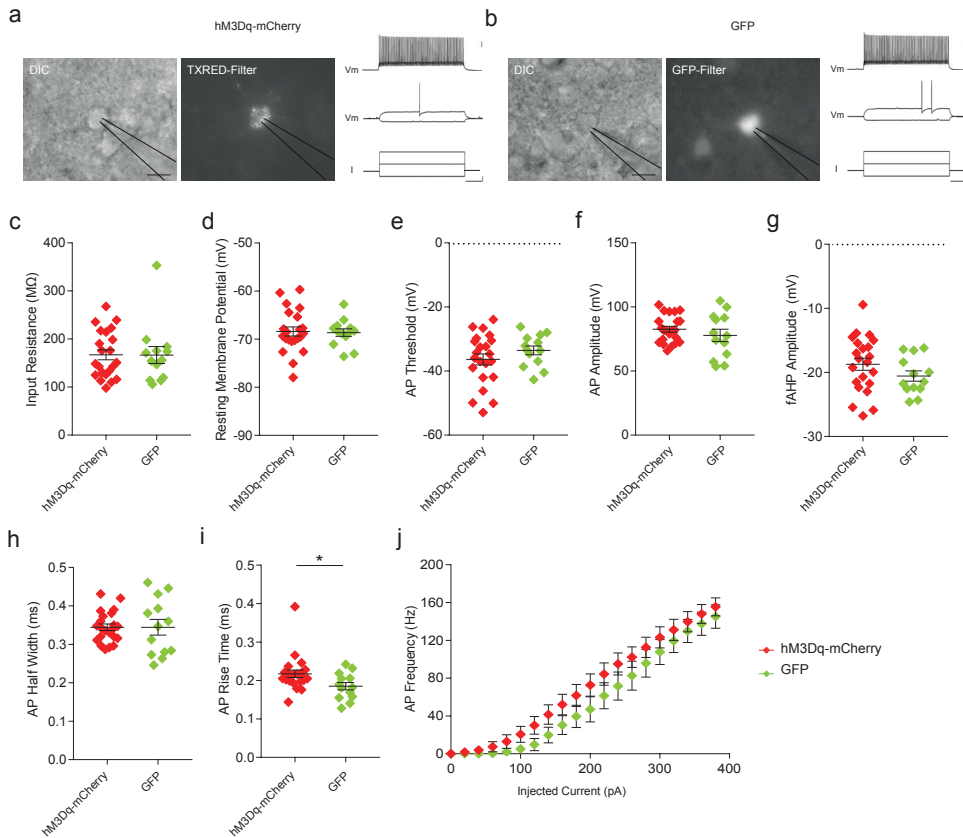


**Figure 4.2.** Fluorescence-targeted whole-cell electrophysiological recordings from hM3Dq-mCherry and contralateral GFP cells. **(a,b)** Representative differential interference contrast (DIC) and epifluorescence images of hM3Dq-mCherry+ (a) and GFP+ (b) cells exhibiting a fast-spiking action potential (AP) train. Scale bars are 15  $\mu$ m (left) and 20 mV, 100 pA and 100 ms from top to bottom (right). **(c-j)** In the absence of CNO, hM3Dq-mCherry+ ( $n = 23$ ; red diamonds) and GFP+ cells ( $n = 13$ ; green diamonds) were electrophysiologically similar: (c) input resistance (hM3Dq-mCherry:  $167.1 \pm 10.5 \text{ M}\Omega$ ; GFP:  $166.7 \pm 17.6 \text{ M}\Omega$ ;  $U = 153.000$ ,  $P = 0.749$ ), (d) resting membrane potential (hM3Dq-mCherry:  $-68.4 \pm 1.0 \text{ mV}$ ; GFP:  $-68.6 \pm 0.8 \text{ mV}$ ;  $t_{(33)} = -0.182$ ,  $P = 0.857$ ), (e) AP threshold (hM3Dq-mCherry:  $-36.4 \pm 1.7 \text{ mV}$ ; GFP:  $-33.6 \pm 1.4 \text{ mV}$ ;  $t_{(33)} = 1.124$ ,  $P = 0.269$ ), (f) AP amplitude (hM3Dq-mCherry:  $82.6 \pm 2.3 \text{ mV}$ ; GFP:  $77.8 \pm 4.8 \text{ mV}$ ;  $t_{(33)} = -0.918$ ,  $P = 0.371$ ), (g) fast after-hyperpolarization (hM3Dq-mCherry:  $-18.7 \pm 0.9 \text{ mV}$ ; GFP:  $-20.6 \pm 0.8 \text{ mV}$ ;  $t_{(33)} = -1.340$ ,  $P = 0.189$ ), (h) AP half-width (hM3Dq-mCherry:  $0.34 \pm 0.01 \text{ ms}$ ; GFP:  $0.34 \pm 0.02 \text{ ms}$ ;  $t_{(33)} = 0.001$ ,  $P = 0.999$ ). (i) A small increase of AP rise time was observed in hM3Dq-mCherry+ cells (hM3Dq-mCherry:  $0.22 \pm 0.01 \text{ ms}$ ; GFP:  $0.19 \pm 0.01 \text{ M}\Omega$ ;  $U = 202.500$ ,  $P = 0.041$ ). (j) Evoked AP firing was unchanged between hM3Dq-mCherry+ and GFP+ cells ( $F_{(19,570)} = 0.988$ ,  $P = 0.473$ ; repeated measures ANOVA). Unpaired two-tailed Student's  $t$ -tests in (d) through (h). Mann-Whitney two-tailed  $U$ -test for (c) and (i) owing to non-normality. Black bars represent mean  $\pm$  s.e.m. AP action potential; fAHP fast after-hyperpolarization; Vm membrane voltage; I current injection.

To determine the influence of DREADD receptor activation on PV+ interneurons, we performed *ex vivo* electrophysiological recordings of hM3Dq-mCherry+ and GFP+ cells in the presence of CNO (Fig. 4.3a). Local application of CNO resulted in membrane depolarization followed by a robust increase in firing frequency of hM3Dq-mCherry+ cells (Fig. 4.3b). Similarly, bath application of CNO (5  $\mu$ M) induced

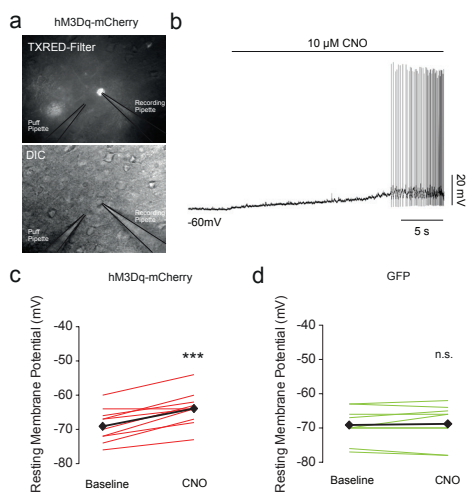
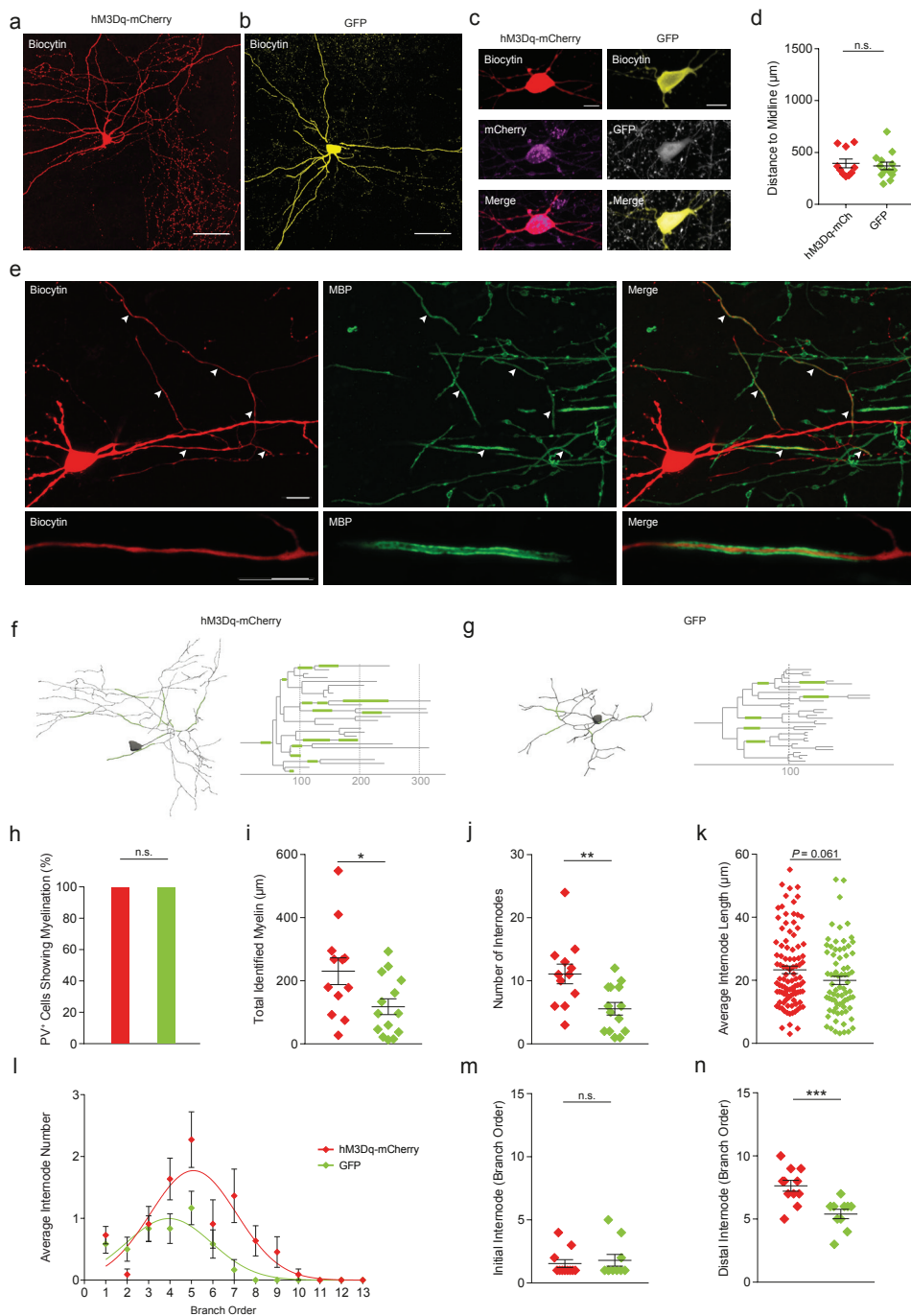


**Figure 4.3.** Ex vivo characterization of CNO-dependent DREADD stimulation. (a) Experimental overview. A puff pipette was used for local application of CNO. (b) Local CNO (10  $\mu$ M) application elicited strong membrane depolarization with a fast-spiking AP train. (c,d) Bath application of 5  $\mu$ M CNO induced a  $\sim$ 5mV depolarization of hM3Dq-mCherry+ cells (red; baseline:  $-69.09 \pm 1.43$  mV; CNO:  $63.90 \pm 1.59$  mV;  $t_{(8)} = -5.963$ ,  $P < 0.001$ ;  $n = 9$  cells), while CNO had no effect on GFP+ cells (green; baseline:  $-69.11 \pm 1.67$  mV; CNO:  $-68.78 \pm 1.94$  mV;  $t_{(8)} = -0.555$ ,  $P = 0.594$ ;  $n = 9$  cells). Black lines indicate means. Paired Student's two-tailed  $t$ -test in (c) and (d). \*\*\*  $P < 0.001$ . n.s. non-significant.

a  $\sim$ 5 mV membrane depolarization in hM3Dq-mCherry+ cells (Fig. 4.3c), while no changes were observed in GFP+ cells (Fig. 4.3d). Therefore, CNO administration selectively increased activity in hM3Dq-mCherry+ cells.

We next sought to examine whether DREADD-mediated activation of PV+ interneurons modulates their myelination. Therefore, we performed NeuroLucida reconstructions of proximal axons of biocytin-labelled hM3Dq-mCherry+ (Fig.

**Figure 4.4.** DREADD-activated cells have increased myelination. (a,b) Maximum projection confocal images of representative biocytin-filled hM3Dq-mCherry+ (a, red) and GFP+ (b, yellow) cells. Scale bars are 50  $\mu$ m. (c) Left: *Post hoc* confirmation demonstrating that putative hM3Dq-mCherry+ biocytin-labeled cells (red) were hM3Dq-mCherry+ (purple). Right: *Post hoc* confirmation that putative GFP+ biocytin-labeled cells (yellow) were GFP+ (grey). Scale bars are 10  $\mu$ m. (d) Reconstructed cells were located at similar cortical depths (hM3Dq-mCherry [red diamonds]:  $394.5 \pm 42.3$   $\mu$ m; GFP [green diamonds]:  $369.8 \pm 36.5$   $\mu$ m;  $U = 61.000$ ,  $P = 0.832$ ). (e) Top: Low-magnification confocal image of a biocytin-labeled PV+ interneuron (red), with myelinated internodes revealed by MBP immunofluorescence (green). Arrowheads indicate myelinated internodes belonging to the biocytin-labeled cell. Scale bar, 10  $\mu$ m. Bottom: High-magnification confocal maximum projection image of a biocytin-labeled (red), myelinated (MBP; green) axonal segment. Scale bar 5  $\mu$ m. (f,g) Proximal axonal reconstruction (left) with indicated segmental myelination of hM3Dq-mCherry+ (f) and GFP+ (g) cells shown in (a) and (b) respectively, with their corresponding schematic dendrogram representation (right). Soma and axon in grey, myelin in green. Horizontal axis,  $\mu$ m. (h) All examined hM3Dq-mCherry+ (red,  $n = 12$ ) and GFP+ cells (green,  $n = 14$ ) show myelination. (i) hM3Dq-mCherry+ cells show a higher total amount of myelin per cell, compared to GFP+ cells. hM3Dq-mCherry:  $230.3 \pm 42.4$   $\mu$ m myelin/cell; GFP:  $117.9 \pm 25.1$   $\mu$ m myelin/cell;  $t_{(24)} = 2.359$ ,  $P = 0.027$ . (j) hM3Dq-mCherry+ cells show a greater number of internodes per cell, compared to GFP+ cells (hM3Dq-mCherry:  $10.4 \pm 1.3$  internodes/cell; GFP:  $5.6 \pm 1.0$  internodes/cell;  $t_{(24)} = 3.008$ ,  $P = 0.006$ ). (k) Internode length is similar between hM3Dq-mCherry+ and GFP+ cells (hM3Dq-mCherry:  $23.2 \pm 1.2$   $\mu$ m,  $n = 99$  internodes; GFP:  $19.9 \pm 1.3$   $\mu$ m,  $n = 75$  internodes;  $t_{(172)} = 1.888$ ,  $P = 0.061$ ). (l) hM3Dq-mCherry+ cells have an increased number of internodes beginning from 4th branch order axonal segments distally ( $F_{(12,240)} = 2.890$ ,  $P < 0.001$ , repeated measures ANOVA). (m) hM3Dq-mCherry+ and GFP+ cells have a similar myelination onset (hM3Dq-mCherry:  $1.7 \pm 0.4$ ; GFP:  $1.9 \pm 0.5$ ;  $U = 89.000$ ,  $P = 0.574$ ). (n) In contrast, the most distal branch order showing myelination is located further along the axon in hM3Dq-mCherry+ cells (hM3Dq-mCherry:  $7.6 \pm 0.4$ ; GFP:  $5.3 \pm 0.3$ ;  $t_{(21)} = 4.387$ ,  $P < 0.001$ ). \*\*\* $P < 0.001$ , \*\* $P < 0.01$ , \* $P < 0.05$ , n.s. non-significant. Unpaired Student's two-tailed  $t$ -test in (i), (j), (k) and (n); Mann-Whitney two-tailed  $U$  test in (d) and (m) owing to non-normality. Black bars represent mean  $\pm$  s.e.m.



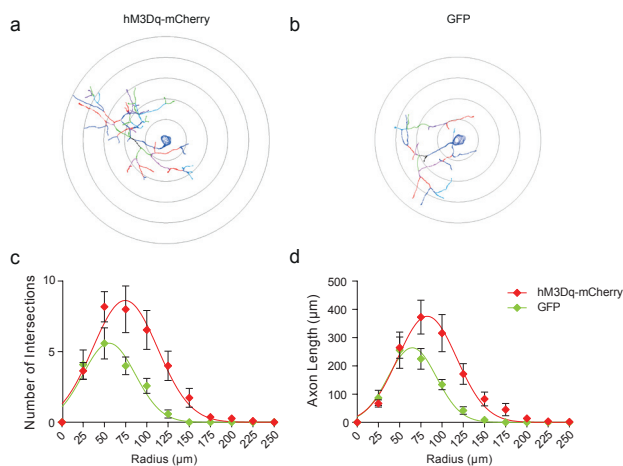


**Figure 4.5.** Sholl analysis reveals activity-dependent enhancement of proximal axonal complexity in PV+ interneurons. (a,b) Representative Sholl analysis for hM3Dq-mCherry+ (a) and GFP+ (b) cell axons. Radial spacing, 25  $\mu\text{m}$ . Colors indicate distinct centrifugal branch orders. (c,d) Number of intersections per Sholl (c;  $F_{(10,210)} = 4.073$ ,  $P < 0.001$ , repeated measures ANOVA) and axonal length per Sholl (d;  $F_{(6,60)} = 3.664$ ,  $P = 0.004$ , repeated measures ANOVA) were significantly increased in hM3Dq-mCherry+ cells (red diamonds) compared to GFP+ cells (green diamonds). Black bars represent s.e.m.

4.4a,c,f) and GFP+ cells (Fig. 4.4b,c,g) including myelination (Fig. 4.4e). hM3Dq-mCherry+ and GFP+ cells were located at a similar depth within the mPFC (Fig. 4.4d). Consistent with previous findings in PV+ interneurons<sup>240</sup>, all reconstructed hM3Dq-mCherry+ and GFP+ cells exhibited axonal myelination (hM3Dq-mCherry: 14/14 cells, 100%; GFP: 12/12 cells, 100%) (Fig. 4.4h). Notably however, hM3Dq-mCherry+ cells exhibited an increase of total length of axonal myelination per neuron (Fig. 4.4i), driven primarily by an increase in the number of internodes (Fig. 4.4j). Internode length showed a trend towards longer internodes in hM3Dq-mCherry+ cells but was statistically unchanged (Fig. 4.4k). Topographical analysis of axonal reconstructions revealed that the enhanced myelination of hM3Dq-mCherry+ cells occurred along 4th – 9th axonal branch order segments (Fig. 4.4l), for which hM3Dq-mCherry+ cells exhibited a significantly higher axonal branch order of distal myelination compared to GFP+ cells (Fig. 4.4n) while the initial onset of myelination was unchanged (Fig. 4.4m). Together, these data show that chemogenetic activation of PV+ interneurons enhances their myelination through an increased number and more distally extended distribution of axonal internodes.

## Cell-specific activation results in axon morphology changes

We next sought to explore whether changes in axonal morphology might underlie the observed increase in total myelination on DREADD-stimulated PV+ interneurons. Therefore, we reconstructed the axon of each cell, beginning from the axon initial segment until the occurrence of a string of *en passant* boutons ( $\geq 3$  consecutive boutons on a single axonal branch located within 15  $\mu\text{m}$ ) on each terminal branch. Consistently, DREADD-stimulated PV+ interneurons had a significantly more elaborated axonal morphology compared to GFP+ controls (Fig. 4.5a,b; 4.6a,b). Using Sholl analysis, hM3Dq-mCherry+ cells exhibited a greater

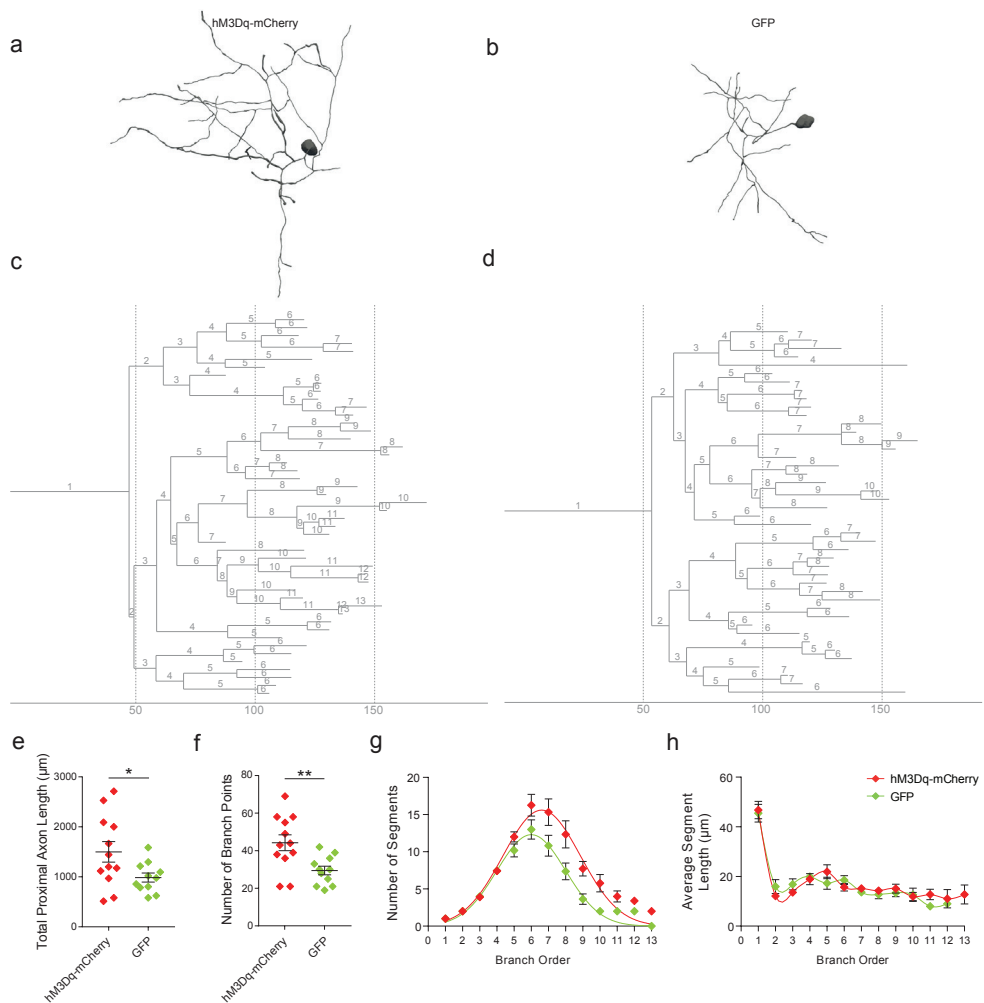


**Figure 4.6.** Branch structure analysis. (a,b) Representative proximal axon reconstruction from hM3Dq-mCherry+ (a) and GFP+ (b) cells. (c,d) Corresponding axonal dendrogram of hM3Dq-mCherry+ and GFP+ cells shown in (a) and (b). Branch orders are centrifugally designated. Horizontal axis,  $\mu\text{m}$ . (e) Total proximal axon length is greater in hM3Dq-mCherry+ (red diamonds) compared to GFP+ cells (green diamonds; hM3Dq-mCherry:  $1499.9 \pm 205.9 \mu\text{m}$ ; GFP:  $985.4 \pm 90.9 \mu\text{m}$ ;  $t_{(21)} = 2.214$ ,  $P = 0.038$ ). (f) hM3Dq-mCherry+ cells have a greater number of branch points compared to GFP+ cells (hM3Dq-mCherry:  $44.3 \pm 4.2$ ; GFP:  $29.5 \pm 2.3$ ;  $t_{(21)} = 3.003$ ,  $P = 0.007$ ). (g) hM3Dq-mCherry+ cells exhibited an increased number of axonal segments on higher order ( $\geq 5$ th branch order) axonal segments ( $F_{(12,252)} = 3.428$ ,  $P < 0.001$ ), while (h) inter-branch point distance remained unchanged ( $F_{(11,44)} = 0.712$ ,  $P < 0.721$ ). \*\* $P < 0.01$ ; \* $P < 0.05$ . n.s. non-significant. Unpaired Student's two-tailed  $t$ -test in (e) and (f). Repeated measures ANOVA in (g) and (h). Black bars represent mean  $\pm$  s.e.m.

number of intersections and longer axonal length compared to GFP+ cells (Fig. 4.5c,d). Moreover, branch structure analysis (Fig. 4.6a-d) also confirmed that hM3Dq-mCherry+ cells had a longer axonal length (Fig. 4.6e) as well as an increased number of branch points (Fig. 4.6f), beginning from the 5th branch order distally (Fig.

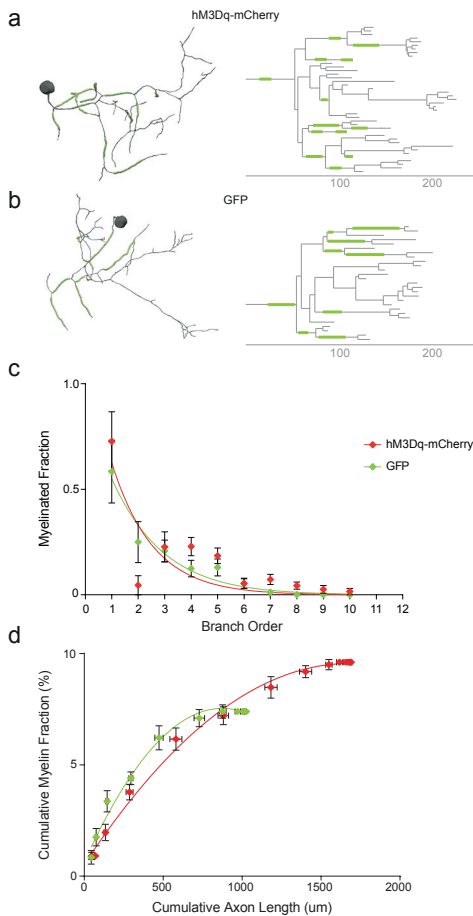


**Figure 4.7.** Enhanced segmental myelination is proportional to the elaboration of axonal morphology. (a-b) Representative PV+ interneuron reconstruction (left) and corresponding axonal dendrogram (right) for hM3Dq-mCherry+ (a) and GFP+ cells (b). Myelinated segments are shown in green. Horizontal axis,  $\mu\text{m}$ . (c) Both hM3Dq-mCherry+ cells (red diamonds) and GFP+ cells (green diamonds) exhibit a decreasing myelination fraction over increasing branch order ( $F_{(12,252)} = 23.823$ ,  $P < 0.001$ , repeated measures ANOVA, main effect of branch order). hM3Dq-mCherry+ cells have a similar proportion of myelinated segments as GFP+ cells across the entire axonal arbor ( $F_{(12,252)} = 1.206$ ,  $P = 0.279$ , repeated measures ANOVA). (d) Consistent with the elaboration of their axonal arborization, hM3Dq-mCherry+ cells contain myelinated segments on more distally extended axonal segments. Black bars represent mean  $\pm$  s.e.m.

4.6g). The average inter-branch point distance also remained unchanged (Fig. 4.6h). Together these data indicate that PV+ interneurons exhibit a robust and highly specific activity-dependent elaboration of their axonal morphology following *in vivo* stimulation in the adult neocortex.

### Activity-driven myelin increases are proportional to axonal morphology changes

Given that DREADD-stimulated PV+ interneurons exhibit increased myelination and altered axonal morphology, we examined whether the increase in myelination was proportional to the change in axonal complexity. For each cell, we examined the proportion of axonal segments per branch order that contained internodes

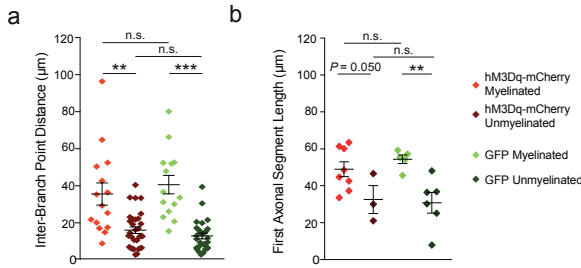


**Figure 4.8.** The inter-branch distance threshold for segmental myelination remains unchanged. (a) Quantification of inter-branch point distance for myelinated versus unmyelinated segments (2nd-5th branch order). Myelinated axonal segments for hM3Dq-mCherry+ (red diamonds) and GFP+ cells (green diamonds) are significantly longer than unmyelinated axonal segments (brown and dark green, respectively; hM3Dq-mCherry:  $t_{(83)} = 3.554$ ,  $P = 0.002$ ; GFP:  $t_{(71)} = 5.949$ ,  $P < 0.001$ ). Length of neither myelinated, nor unmyelinated, segments differed between hM3Dq-mCherry+ or GFP+ cells (hM3Dq-mCherry myelinated:  $36.2 \pm 5.3 \mu\text{m}$ ; hM3Dq-mCherry unmyelinated:  $16.6 \pm 1.6 \mu\text{m}$ ; GFP myelinated:  $41.0 \pm 4.3 \mu\text{m}$ ; GFP+ unmyelinated:  $13.5 \pm 1.7 \mu\text{m}$ ).  $n = 3$  cells per region. n.s. non-significant,  $t_{(36)} = -0.699$ ,  $P = 0.489$  for myelinated and  $t_{(118)} = 1.325$ ,  $P = 0.188$  for unmyelinated segments, respectively. (b) The first axonal branch point was located closer to the soma when it arose before, rather than after, the first myelinated internode in both hM3Dq-mCherry+ and GFP+ cells. hM3Dq-mCherry:  $t_{(11)} = 2.202$ ,  $P = 0.050$ ; GFP:  $t_{(11)} = 4.025$ ,  $P = 0.002$ . n.s. non-significant,  $t_{(14)} = -1.342$ ,  $P = 0.201$  for myelinated and  $t_{(7)} = 0.188$ ,  $P = 0.856$  for unmyelinated segments, respectively. \*\*\* $P < 0.001$ ; \*\* $P < 0.01$ . Unpaired Student's two-tailed  $t$ -tests in (a) and (b). Black bars represent mean  $\pm$  s.e.m.

(myelination fraction). Both hM3Dq-mCherry+ and GFP+ cells showed a progressively decreasing myelination fraction with increasing branch order (Fig. 4.7a-c). Moreover, hM3Dq-mCherry+ cells exhibit a similar myelination fraction extending to the distal limit of GFP+ cells (Fig. 4.7c), beyond which hM3Dq-mCherry+ cells exhibit additional myelinated segments along their extended axonal length (Fig. 4.7d). Together, these data suggest that the activity-dependent increase in myelination of PV+ interneurons is predominantly mediated by the elaboration of axon morphology.

## Myelination is restricted by axonal distance between branch points

Previous studies have reported that proximal axon myelination most commonly occurs on uninterrupted axonal segments of at least  $\sim 15 \mu\text{m}$ .<sup>240</sup> Therefore, we examined whether activity-induced myelination changed these requirements. We quantified inter-branch point distances from the soma up to 5th order axonal segments, including whether these segments contained an internode. Unmyelinated inter-branch point segments were consistently shorter than corresponding myelinated segments in both GFP+ cells and hM3Dq-mCherry+ cells (Fig. 4.8a). Overall, inter-branch segments  $>40 \mu\text{m}$  were frequently myelinated (91.6%), while inter-branch segments  $<15 \mu\text{m}$  tended to be unmyelinated (96.2%). An analogous dichotomy was

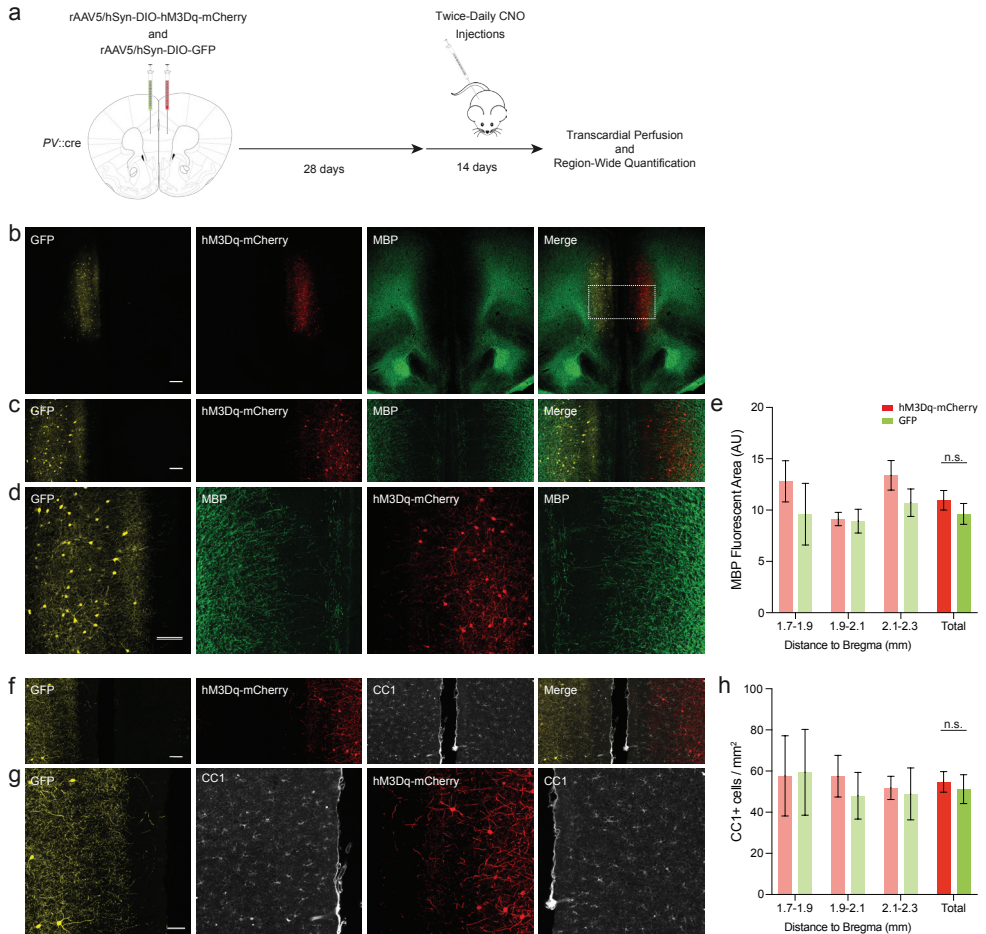


**Figure 4.9.** No observed changes in oligodendrocyte density or total myelin content. **(a)** Experimental design. Adult PV::cre mice received pseudorandomly assigned unilateral stereotactic injections of cre-dependent hM3Dq-mCherry and contralateral GFP virus in mPFC. Twenty-eight days post-surgery, mice received twice daily intraperitoneal administration of 1 mg/kg CNO for 14 days. One day later, mice were sacrificed for immunofluorescence labeling. **(b)** Confocal overview images of myelin (MBP; green) labeling from GFP (yellow) and hM3Dq-mCherry (red) transduced hemispheres; white box indicates quantified region. Scale bar, 250  $\mu$ m **(c)** Zoomed-in confocal images of the boxed area in **(b)**. Scale bar, 50  $\mu$ m **(d)** High magnification image of myelin (MBP; green) within the GFP (yellow) and hM3Dq-mCherry (red) transduced hemispheres. Scale bar, 50  $\mu$ m. **(e)** MBP fluorescent area is similar between GFP and hM3Dq-mCherry transduced hemispheres ( $t_{(3)} = 0.908, P = 0.431; n = 4$  mice). **(f)** Confocal overview image of CCI+ oligodendrocytes (grey) in GFP (yellow) and hM3Dq-mCherry (red) transduced hemispheres. Scale bar, 50  $\mu$ m **(g)** Higher magnification confocal image of CCI+ oligodendrocytes (grey) in GFP (yellow) and hM3Dq-mCherry (red) transduced hemispheres. Scale bar, 50  $\mu$ m. **(h)** The density of CCI+ oligodendrocytes was similar between hemispheres ( $t_{(7)} = 0.693, P = 0.511; n = 2$  mice). Paired Student's two-tailed t-test in **(e)** and **(h)**. Black bars represent mean  $\pm$  s.e.m. n.s. non-significant

also evident in the location of the first axonal branch point, which was positioned closer to the soma when it arose before, compared to after, the first internode of both hM3Dq-mCherry+ and GFP cells+ (Fig. 4.8b). These findings suggest that the activity-driven increase of PV+ interneuron myelination is proportional to increase in total axonal length, while maintaining a similar topography of axonal morphology and myelination.

## **No alterations in total myelin content or oligodendrocyte number**

Prior studies using optogenetic and chemogenetic pyramidal cell activation have demonstrated substantial increases in total myelin content and oligodendrocyte lineage cell density.<sup>19,20</sup> Therefore, we sought to examine the cell-type specificity of the activity-dependent changes in PV+ axonal myelination by quantifying both total myelin content and oligodendrocyte density in the surrounding volume. We performed immunofluorescent stainings for myelin (MBP) and mature oligodendrocytes (CCI) in hM3Dq-mCherry+ and GFP+ transduced areas (Fig. 4.9a). In contrast to previous studies involving pyramidal cell stimulation, we did not find evidence for changes of total myelin content (Fig. 4.9b-e) or oligodendrocyte density (Fig. 4.9f-h) between hM3Dq-mCherry+ and GFP+ transduced areas. Accordingly, the observed activity-dependent changes in PV+ axonal morphology and myelination appear likely to be cell autonomous.

## **Discussion**

In the present paper, we examined whether *in vivo* activity-dependent myelination occurs in neocortical fast-spiking, PV+ interneurons. Utilizing cell-specific chemogenetic activation followed by single-cell reconstructions of PV+ interneurons in the adult mouse mPFC, we found that *in vivo* stimulation of PV+ interneuron activity induced a ~50% increase in proximal axonal length with a proportional increase in myelination. These findings add to the understanding of dynamic myelination, but our results suggest that, at least for PV+ interneurons, this is mediated significantly by activity-dependent plasticity of axonal morphology.

Employing single-cell reconstructions allowed us to comprehensively document the position of each myelinated segment along the axon, in contrast to previous studies using larger-scale analyses.<sup>19</sup> We found that stimulated cells exhibited increased myelination of more distal axon segments (branch order  $\geq 4$ ), while myelination did not differ on more proximal branch orders. Furthermore, due to bilateral transfection with either DREADDs or GFP, we could reconstruct cells from both hemispheres under similar conditions, thereby minimizing possible experience-dependent variation. Finally, our studies were performed in adult mice, thereby

reducing the likelihood of neurodevelopmental interactions. As a corollary, whether activity-dependent PV+ myelination is regulated similarly during neurodevelopment is an important question that remains to be determined.

A limitation of the current study is that we could not follow the evolution of axonal and myelination changes longitudinally over time. Therefore, the time course of the observed changes of axonal morphology and myelination remain unknown, as well as a definitive confirmation that the changes in axonal morphology precede the increase in myelination. Moreover, it remains unknown which specific axonal parameters govern the increase of PV+ interneuron myelination. Our findings suggest that a substantial proportion of the increase in myelination is mediated by an activity-induced elaboration of PV+ interneuron axonal arborization<sup>244</sup> which is subsequently myelinated. Another candidate is axon diameter, which has been shown to change rapidly upon neuronal activity in CA3 pyramidal cells<sup>245</sup> and has been demonstrated to function as a critical biophysical threshold permissive for myelination.<sup>246,247</sup> Lastly, an activity-dependent modulation of vesicular release probability could also be an important determinant, as axonal vesicular release has been shown to regulate the differentiation to myelinating oligodendrocytes of oligodendrocyte progenitor cells in close proximity to unmyelinated axonal segments.<sup>242,248</sup> The increase of axonal myelination appears to result from the addition of internodes, since the distribution of internode length is largely preserved (Fig. 4.4k). In line with previous findings,<sup>240</sup> we also find that the pattern of myelination along axons of stimulated PV+ interneurons is constrained by a similar inter-branch segment length threshold (Fig. 4.8). This suggests that although neuronal activity can dynamically modulate axonal morphology, there is yet no evidence for activity-dependent plasticity of the fundamental biophysical parameters dictating the eligibility of myelination at a given axonal segment.

Given previous reports that cell-type specific stimulation of cortical pyramidal neurons resulted in observable changes of total myelin content and oligodendrocyte density, we similarly assessed the cell-type specificity following chemogenetic activation of PV+ interneurons. Notably however, we did not find changes in oligodendrocyte density or overall myelin labeling. We suggest two possibilities for the absence of an observable difference of these metrics. First, given that PV+ interneurons contribute only a small minority of the total myelin content in the mPFC<sup>240</sup>, and that virally-labeled cells constitute only a subset of PV+ interneurons within the transduced areas, the possibility exists that changes in the number of oligodendrocytes due to PV+ activation might have been too small to be observed using volumetric quantification. Moreover, with regard to total myelin content, the limitation of a volumetric quantification might therefore also be considered likely on the basis of the demonstrated increase of myelination per chemogenetically-activated PV+ interneuron (Fig. 4.4). The second non-mutually exclusive possibility is predicated upon the established function of PV+ interneurons as strong modulators

of local network activity.<sup>47</sup> In this scenario, PV+ interneuron-mediated inhibition of principal cell firing might lead to reductions in myelination of an equivalent magnitude as the increase in myelination of PV+ interneurons.

Together, we identify a novel form of activity-dependent myelination mediated by axonal morphological plasticity of PV+ interneurons. These findings contribute to the increasing evidence demonstrating the dynamic plasticity of adult neocortical myelination and axonal morphology.

## Methods

### Mice

All experiments were approved by the Dutch Ethical Committee and in accordance with the Institutional Animal Care and Use Committee (IACUC) guidelines. Mouse lines were obtained from Jackson Laboratory:

Pvalb <sup>tm1(cre)Arbr/J</sup> mice (PV::cre) <sup>233</sup>	strain #008069
C57BL/6J (WT)	strain #000664

All lines were backcrossed for more than 10 generations in C57BL/6J. Adult mice of both genders were used from 8-12 weeks of age. Mice were group-housed in same-sex groups of two to four mice and maintained on a 12 h light/dark cycle with *ad libitum* access to food and water. After surgery, mice were single-housed until further experiments.

### Viral Labeling and CNO injections

Heterozygous PV::cre mice were used for viral-mediated cell-type specific labelling, performed using adeno-associated virus (AAV) expression with cre-dependent AAV5/hSyn-DIO-hM3Dq-mCherry and AAV5/hSyn-DIO-GFP (University of Pennsylvania Viral Vector Core). Virus was diluted to  $\sim 5 \times 10^{11}$  GC/ml in phosphate-buffered saline (PBS) to achieve sparse labelling. hM3Dq-mCherry and GFP control injections were counterbalanced between the left and right hemisphere. All mice showed successful bilateral virus expression with no contralateral contamination.

Anesthesia was induced using 5% isoflurane (O<sub>2</sub> flow of 0.5 L/min), and subsequently maintained with 1-2% isoflurane during surgery. Body temperature was maintained at 37°C. Mice were placed into a custom-made stereotaxic frame using a mouth bar (Stoelting) for head fixation. Analgesia was provided systemically by subcutaneous Temgesic injection (buprenorphine 0.5 mg/kg) and locally by xylocaine spray (100 mg/mL; AstraZeneca) directly applied on the skull. To access the brain, a longitudinal scalp incision of  $\sim 1$  cm length was made to reveal the skull, and a small

craniotomy (<1 mm) was performed overlying the injection sites at the following coordinates (in mm):

mPFC: +1.75 bregma,  $\pm 0.35$  lateral, -1.9 dorsoventral

Mice used for electrophysiological recordings received 1  $\mu$ L in a 1/2 dilution. Virus was aspirated in a borosilicate glass micropipette, which was slowly lowered to the target site. Virus injection was controlled by an automated syringe pump (infusion speed 0.1  $\mu$ L/min). At the conclusion of the injection, the micropipette was maintained in place for another 5 min and then slowly withdrawn. The surgical wound was closed with skin-glue (Derma+flex). Mice were left to recover for 28 days to allow expression of hM3Dq-mCherry and GFP protein. To optimize the bilateral virus injection symmetry necessary for consequent bilateral electrophysiology, we took particular care at a few key points: 1) Mouse skulls were always carefully vertically leveled based on bregma and lambda, 2) glass micropipettes were always checked to run properly before injections, and were carefully cleaned to remove excess virus particles, 3) drill holes were kept as small as possible (<1 mm), and 4) mice were left to recover for exactly 28 days before starting clozapine n-oxide (CNO) injections to minimize expression variations between mice.

After 28 days of recovery, mice were injected intraperitoneally with CNO (Sigma) 1 mg/kg twice daily (at ~9:00h and ~18:00h) for 14 consecutive days. Mice displayed no weight loss over the injection period (day 1:  $26.2 \pm 1.5$  g; day 14:  $24.8 \pm 1.1$  g;  $P = 0.458$ ; Paired two-tailed *t*-test) or overt behavioral abnormalities under CNO administration.

## Electrophysiology

The next morning after the last CNO injection, mice were anesthetized using 5% isoflurane and decapitated in ice-cold, NMDG-based cutting solution containing (in mM): 93 N-methyl-d-glucamine (NMDG), 93 HCl, 30 NaHCO<sub>3</sub>, 25 D-glucose, 20 HEPES, 5 Na-ascorbate, 2 thiourea, 10 MgCl<sub>2</sub>, 3 Na-pyruvate, 2.5 KCl, 1.25 NaH<sub>2</sub>PO<sub>4</sub> and 0.5 CaCl<sub>2</sub> (300 mOsm, pH 7.4) oxygenated with 95% O<sub>2</sub>/5% CO<sub>2</sub>. Coronal slices (300  $\mu$ m) were cut with a vibrating slicer (Microm HM 650V, Thermo Scientific) and incubated in cutting solution at 37 °C for 8 min, followed by oxygenated (95% O<sub>2</sub>/5% CO<sub>2</sub>) artificial cerebrospinal fluid (aCSF) at 37 °C for another 10 min. ACSF contained (in mM) 127 NaCl, 25 NaHCO<sub>3</sub>, 25 D-glucose, 2.5 KCl, 1.25 NaH<sub>2</sub>PO<sub>4</sub>, 1.5 MgSO<sub>4</sub> and 1.6 CaCl<sub>2</sub>. Slices were then allowed to recover at room temperature for at least 1 h before recordings.

PV+ interneurons from the prelimbic region layer V of the mPFC were visualized by mCherry or GFP fluorescence using a TXRED or GFP filter (Semrock, Rochester, NY, USA), respectively. Importantly, GFP+ control cells were recorded from contralateral hemispheres of the same coronal slices as recorded hM3Dq-

mCherry+ cells, and cells were recorded from equal distances from the midline (Fig. 4.4d). To minimize variation in proportion of missing axon due to slicing, cells were consistently patched at a depth of 20-50  $\mu\text{m}$  from the slice surface. Whole-cell recordings were made using borosilicate glass pipettes (3.5–5.5  $\text{M}\Omega$  resistance) with intracellular solution containing (in mM) 120 K-gluconate, 10 KCl, 10 HEPES, 10 K-phosphocreatine, 4 ATP-Mg, 0.4 GTP, and 5 mg/ml biocytin (pH was adjusted to 7.4 using KOH, and osmolarity measured 285-290 mOsm). All recorded mCherry+ and GFP+ cells had a fast-spiking phenotype, with subthreshold membrane potential oscillations, suprathreshold high-frequency, non-adapting firing patterns, and large amplitude fast after-hyperpolarizations. Cells were filled for at least 25 min. for proper biocytin spreading.

Recordings were performed in aCSF at near-physiological temperatures ( $33 \pm 1^\circ\text{C}$ ) using HEKA EPC10 quattro amplifiers and Patchmaster software (40 kHz). Series resistance was typically  $<25 \text{M}\Omega$  and fully compensated for bridge balance and capacitance. No correction was made for liquid junction potential. Data analysis was performed offline using Igor Pro v6 (Wavemetrics).

Basic physiological characteristics were determined from voltage responses to square-wave current pulses of 500 ms duration, ranging from  $-100 \text{pA}$  to  $+300 \text{pA}$ , and delivered in 20  $\text{pA}$  intervals. Input resistance was determined by the slope of the linear regression through the voltage-current curve. Single action potential (AP) characteristics were obtained from the first elicited action potential. AP threshold was defined as the inflection point at the foot of the regenerative upstroke. AP amplitude was defined as the voltage difference between the threshold and peak voltage. AP half-width was measured at half of the peak amplitude. AP rise time was quantified as duration from 10% to 90% of the peak amplitude. The fast after-hyperpolarizing potential (fAHP) amplitude was measured as the hyperpolarizing deflection from AP threshold following AP initiation.

Local application of CNO was performed at a concentration of 10  $\mu\text{M}$  (in 0.9% NaCl) through a borosilicate glass pipette (3.5–5.5  $\text{M}\Omega$  resistance). The pipette was backfilled with CNO and positioned at a distance of  $\sim 20 \mu\text{m}$  from the recorded soma within the same focal plane. A total of 50  $\mu\text{L}$  CNO (10  $\mu\text{M}$ ) was applied over 250 ms at a fixed rate of 200  $\mu\text{L}/\text{sec}$ .

## Immunofluorescence

For recovery of biocytin-labelled cells following electrophysiological recordings, 300  $\mu\text{m}$  slices were incubated overnight at  $4^\circ\text{C}$  in fresh 4% paraformaldehyde (PFA). Slices were extensively rinsed at room temperature in PBS, and stained in PBS buffer containing 0.4% Triton X-100, 2% normal horse serum (NHS; Invitrogen,

Bleiswijk, The Netherlands) and streptavidin-conjugated secondary antibody 488 (1:300, Jackson; for hM3Dq-mCherry+ cells) or streptavidin-Cy3 (1:300; Invitrogen; for GFP+ cells) for 5 h at room temperature. Slices were washed with PBS and PB 0.1 M and mounted on slides, cover slipped with 200  $\mu$ l Mowiol (Sigma), sealed, and immediately imaged for full axonal morphology (see Confocal Microscopy). To avoid excessive thinning or drying of 300  $\mu$ m sections, cells were mounted, imaged and returned to PB 0.1 M directly after imaging.

After full cell imaging, 300  $\mu$ m slices were extensively washed in PB 0.1 M and PBS, and subsequently incubated overnight at 4°C in 30% sucrose (0.1 M PB). Sections were then carefully recut at 40  $\mu$ m using a freezing microtome (Leica, Wetzlar, Germany; SM 2000R) and stored serially in 0.1 M PB at 4°C. Forty  $\mu$ m sections were washed with PBS and pre-incubated with a blocking PBS buffer containing 0.5% Triton X-100 and 10% NHS for 1 h at room temperature. Sections were incubated in PBS buffer containing 0.4% Triton X-100 and 2% NHS for 72 h at 4°C and goat anti-MBP (1:300, Santa Cruz, C-16, sc-13914). Then, sections were washed with PBS, and incubated with corresponding Alexa-conjugated secondary antibodies (1:300, Invitrogen) and cyanine dyes (1:300, Sanbio, Uden, The Netherlands) in PBS buffer containing 0.4% Triton X-100, 2% NHS for 5 h at room temperature. For biocytin, streptavidin-A488 (1:300, Jackson) and streptavidin-Cy3 (1:300, Invitrogen) were again used. Nuclear staining was performed using DAPI (1:10,000, Invitrogen). Sections were washed with PB 0.1 M and mounted on slides, cover slipped with Vectashield H1000 fluorescent mounting medium (Vector Labs, Peterborough, UK), sealed and imaged.

An independent group of mice received CNO injections for 14 days prior to transcardial perfusion using 4% PFA. Brains were resected, placed in 4% PFA for post-fixation (2 h) at room temperature, and subsequently stored in 10% sucrose solution (0.1 M PB) overnight at 4°C. The next day brains were embedded in gelatin (12% gelatin (Sigma-Aldrich)/10% sucrose), post-fixed (10% PFA/30% sucrose) for 2 h at room temperature, and then stored in 30% sucrose solution overnight at 4°C. Coronal sections were made on a freezing microtome in 40  $\mu$ m and collected in 0.1 M PB. Subsequently, slices were similarly stained as described above for recut electrophysiology slices. The following primary antibodies were used:

- rabbit anti-mCherry (1:500, Millipore, Abcam, ab167453)
- chicken anti-GFP (1:2000, Aves)
- mouse anti-PV (1:1000, Swant, 235)
- goat anti-MBP (1:300, Santa Cruz, C-16, sc-13914)
- mouse anti-CCI (1:100, Merck, ab-7)

## Confocal Imaging and Analysis

Confocal imaging was performed using a Zeiss LSM 700 microscope (Carl Zeiss) equipped with Plan-Apochromat 10x/0.45, 20x/0.8 and 63x/1.4 (oil immersion) objectives. DAPI, Alexa488, Cy3 and Alexa647, and were imaged using excitation wavelengths of 405, 488, 555, 639 nm, respectively.

Reconstructions of biocytin-filled cells were obtained from 300  $\mu\text{m}$  slices at 63x magnification with 1x digital zoom and a z-step size of 0.5  $\mu\text{m}$ . For axonal myelin reconstructions, recut and restained 40  $\mu\text{m}$  slices were imaged at 63x magnification with 1x digital zoom and a z-step size of 0.5  $\mu\text{m}$ . All images were transferred to NeuroLucida 360 software (v2.8; MBF Bioscience) and reconstructed using interactive tracing with the Directional Kernels method. Reconstructed soma, axon and myelin segments were analyzed with NeuroLucida Explorer (MBF Bioscience). Axons were easily identified as the thinnest, smoothest, and most highly branched processes originating from either the soma or primary dendrite. In addition, axons seemed to branch at more obtuse  $\geq 90^\circ$  angles from one another, often turning back toward the soma, whereas dendrites branched at smaller angles ( $< 90^\circ$ ), continuing a trajectory away from the soma. All reconstructed cells showed a classical basket cell morphology<sup>249</sup>, which is in line with a recent study showing absence of chandelier cells beyond mPFC layer II<sup>250</sup>.

Myelinated axonal segments were defined as the circumferential bordering of a streptavidin-labelled axon by an MBP+ myelin signal. Myelin segments that exited a slice were removed from subsequent analysis. No spatial corrections were made for tissue shrinkage.

Transduction efficiency and specificity, as well as oligodendrocyte number, were measured in transduced regions in the prelimbic area of the mPFC (Bregma: +2.30 till +1.70 mm) of brain slices from transcardially perfused mice. Stacked confocal images were obtained at 20x with 1x digital zoom and a z-step size of 3  $\mu\text{m}$ . A 467  $\mu\text{m} \times 467 \mu\text{m} \times 12 \mu\text{m}$  counting frame was established for manual counting using the multi-point tool in Fiji image analysis software (version 2.0.0). Colocalization with PV was defined as a mCherry- or GFP-labeled soma overlapping with PV+ soma signal.

## Statistical Analysis

Statistical analysis was performed using IBM SPSS (version 23). All data sets were examined using Shapiro-Wilk test for normality. Data sets with normal distributions were analysed for significance using unpaired or paired Student's two-tailed *t*-test or repeated measures analysis of variance (ANOVA) measures followed by Tukey's

---

*post hoc* test. Data sets with non-normal distributions were analysed using Mann-Whitney *U* test. Significance threshold was set at  $P < 0.05$ , and throughout the paper exact P-values values are provided except when  $P < 0.001$ . All data are expressed as mean  $\pm$  standard error. On basis of previously published data sets<sup>240</sup>, we chose similar sample sizes for all experiments performed. Results are the combination of three animal cohorts that showed similar results.





# References



## References

1. Boullerne, A. I. The history of myelin. *Exp. Neurol.* **283**, 431–445 (2016).
2. Deiters, O. F. K. *Untersuchungen über Gehirn und Rückenmark des Menschen und der Säugethiere.* (1865).
3. Cajal, S. R. y. *Histologie du système nerveux de l'homme et des vertèbres.* (1911).
4. Debanne, D. Information processing in the axon. *Nat. Rev. Neurosci.* **5**, 304–316 (2004).
5. Debanne, D., Campanac, E., Bialowas, A., Carlier, E. & Alcaraz, G. Axon physiology. *Physiol. Rev.* **91**, (2011).
6. Young, J. Z. The giant nerve fibres and epistellar body of cephalopods. *Q. J. Microsc. Sci.* **78**, 367–386 (1936).
7. Tasaki, I. The electro-saltatory transmission of the nerve impulse and the effect of narcosis upon the nerve fiber. *Am. J. Physiol.* **127**, 211–227 (1939).
8. Huxley, A. F. & Stampfli, R. Evidence for saltatory conduction in peripheral myelinated nerve fibers. *J. Physiol.* 315–339 (1949).
9. Nave, K.-A. & Werner, H. B. Myelination of the Nervous System: Mechanisms and Functions. *Annu. Rev. Cell Dev. Biol.* **30**, 503–533 (2014).
10. Rasband, M. N. & Peles, E. The nodes of Ranvier: Molecular assembly and maintenance. *Cold Spring Harb. Perspect. Biol.* **8**, 1–16 (2016).
11. Olivares, R., Montiel, J. & Aboitiz, F. Species differences and similarities in the fine structure of the mammalian corpus callosum. *Brain. Behav. Evol.* **57**, 98–105 (2001).
12. Tomassy, G. S. et al. Distinct profiles of myelin distribution along single axons of pyramidal neurons in the neocortex. *Science* **344**, 319–24 (2014).
13. Hildebrand, C., Remahl, S., Persson, H. & Bjartmar, C. Myelinated nerve fibres in the CNS. *Prog. Neurobiol.* **40**, 319–384 (1993).
14. Michalski, J.-P. & Kothary, R. Oligodendrocytes in a nutshell. *Front. Cell. Neurosci.* **9**, 340 (2015).
15. O'Kusky, J. & Colonnier, M. A laminar analysis of the number of neurons, glia, and synapses in the visual cortex (area 17) of adult macaque monkeys. *J. Comp. Neurol.* **210**, 278–290 (1982).
16. Yeung, M. S. Y. et al. Dynamics of oligodendrocyte generation and myelination in the human brain. *Cell* **159**, 766–774 (2014).
17. Young, K. M. et al. Oligodendrocyte dynamics in the healthy adult CNS: evidence for myelin remodeling. *Neuron* **77**, 873–85 (2013).
18. Hughes, E. G., Orthmann-Murphy, J. L., Langseth, A. J. & Bergles, D. E. Myelin remodeling through experience-dependent oligodendrogenesis in the adult somatosensory cortex. *Nat. Neurosci.* **21**, 696–706 (2018).
19. Gibson, E. M. et al. Neuronal activity promotes oligodendrogenesis and adaptive myelination in the mammalian brain. *Science* **344**, 1252304 (2014).
20. Mitew, S. et al. Pharmacogenetic stimulation of neuronal activity increases myelination in an axon-specific manner. *Nat. Commun.* **9**, 1–16 (2018).
21. Makinodan, M. A Critical period for social experience-dependent oligodendrocyte maturation and myelination. *Science*. **337**, 1357 (2012).
22. Etxebarria, A. et al. Dynamic modulation of myelination in response to visual stimuli alters optic nerve conduction velocity. *J. Neurosci.* **36**, 6937–6948 (2016).
23. Purger, D., Gibson, E. M. & Monje, M. Myelin plasticity in the central nervous system. *Neuropharmacology* **110**, 563–573 (2016).
24. Gibson, E. M., Geraghty, A. C. & Monje, M. Bad wrap: Myelin and myelin plasticity in health and disease. *Dev. Neurobiol.* **78**,

- 123–135 (2018).
25. Fields, R. D. A new mechanism of nervous system plasticity: activity-dependent myelination. *Nat. Rev. Neurosci.* **16**, 756–767 (2015).
  26. de Faria, O., Pama, E. A. C., Evans, K., Luzhynskaya, A. & Káradóttir, R. T. Neuroglial interactions underpinning myelin plasticity. *Dev. Neurobiol.* **78**, 93–107 (2018).
  27. Chang, K.-J., Redmond, S. A. & Chan, J. R. Remodeling myelination: implications for mechanisms of neural plasticity. *Nat. Neurosci.* **19**, 190–197 (2016).
  28. Mount, C. W. & Monje, M. Wrapped to adapt: Experience-dependent myelination. *Neuron* **95**, 743–756 (2017).
  29. Tomassy, G. S., Dershowitz, L. B. & Arlotta, P. Diversity matters: A revised guide to myelination. *Trends Cell Biol.* **26**, 135–147 (2016).
  30. Saab, A. S. & Nave, K. A. Myelin dynamics: protecting and shaping neuronal functions. *Curr. Opin. Neurobiol.* **47**, 104–112 (2017).
  31. Kondiles, B. R. & Horner, P. J. Myelin plasticity, neural activity, and traumatic neural injury. *Dev. Neurobiol.* **78**, 108–122 (2018).
  32. Xiao, L. et al. Rapid production of new oligodendrocytes is required in the earliest stages of motor-skill learning. *Nat. Neurosci.* **19**, 1210–1217 (2016).
  33. McKenzie, I. A. et al. Motor skill learning requires active central myelination. *Science*. **346**, 318–322 (2014).
  34. Nishiyama, A., Komitova, M., Suzuki, R. & Zhu, X. Polydendrocytes (NG2 cells): multifunctional cells with lineage plasticity. *Nat. Rev. Neurosci.* **10**, 9–22 (2009).
  35. Hughes, E. G., Kang, S. H., Fukaya, M. & Bergles, D. E. Oligodendrocyte progenitors balance growth with self-repulsion to achieve homeostasis in the adult brain. *Nat. Neurosci.* **16**, 668–76 (2013).
  36. Lee, Y. et al. Oligodendroglia metabolically support axons and contribute to neurodegeneration. *Nature* **487**, 443–8 (2012).
  37. Fünfschilling, U. et al. Glycolytic oligodendrocytes maintain myelin and long-term axonal integrity. *Nature* **485**, 517–21 (2012).
  38. Saab, A. S. et al. Oligodendroglial NMDA receptors regulate glucose import and axonal energy metabolism. *Neuron* **91**, 119–32 (2016).
  39. Devinsky, O. et al. Epilepsy. *Nat. Rev. Dis. Prim.* **4**, 18024 (2018).
  40. Brohan, J. & Goudra, B. G. The Role of GABA Receptor Agonists in Anesthesia and Sedation. *CNS Drugs* **31**, 845–856 (2017).
  41. Roland, P. E. Space-time dynamics of membrane currents evolve to shape excitation, spiking, and inhibition in the cortex at small and large scales. *Neuron* **94**, 934–942 (2017).
  42. Markram, H. et al. Reconstruction and simulation of neocortical microcircuitry. *Cell* **163**, 456–492 (2015).
  43. Jiang, X. et al. Principles of connectivity among morphologically defined cell types in adult neocortex. *Science* **350**, aac9462 (2015).
  44. Tasic, B. et al. Adult mouse cortical cell taxonomy revealed by single cell transcriptomics. *Nat. Neurosci.* **19**, 335–46 (2016).
  45. Letzkus, J. J., Wolff, S. B. E. & Lüthi, A. Disinhibition, a circuit mechanism for associative learning and memory. *Neuron* **88**, 264–276 (2015).
  46. Inde, Z. et al. Initiation of behavioral response to antidepressants by cholecystokinin neurons of the dentate gyrus. *Neuron* **95**, 564–76 (2017).
  47. Hu, H., Gan, J. & Jonas, P. Interneurons. Fast-spiking, parvalbumin+ GABAergic interneurons: from cellular design to microcircuit function. *Science* **345**,

- 1255263 (2014).
48. Kim, Y. et al. Brain-wide maps reveal stereotyped cell-type-based cortical architecture and subcortical sexual dimorphism. *Cell* **171**, 456–469.e22 (2017).
  49. Packer, A. M. & Yuste, R. Dense, unspecific connectivity of neocortical parvalbumin-positive interneurons: a canonical microcircuit for inhibition? *J. Neurosci.* **31**, 13260–71 (2011).
  50. Sohal, V. S., Zhang, F., Yizhar, O. & Deisseroth, K. Parvalbumin neurons and gamma rhythms enhance cortical circuit performance. *Nature* **459**, 698–702 (2009).
  51. Cardin, J. A. et al. Driving fast-spiking cells induces gamma rhythm and controls sensory responses. *Nature* **459**, 663–7 (2009).
  52. Sauer, J. F., Strüber, M. & Bartos, M. Impaired fast-spiking interneuron function in a genetic mouse model of depression. *Elife* **4**, e04979 (2015).
  53. Marín, O. Interneuron dysfunction in psychiatric disorders. *Nat. Rev. Neurosci.* **13**, 107–20 (2012).
  54. Cooper, E. C. Ankyrin-G isoform imbalance and interneuronopathy link epilepsy and bipolar disorder. Ankyrin-G isoform imbalance and interneuronopathy link epilepsy and bipolar disorder. *Mol. Psychiatry* **22**, 1464–72 (2017).
  55. Peñagarikano, O. et al. Absence of CNTNAP2 leads to epilepsy, neuronal migration abnormalities, and core autism-related deficits. *Cell* **147**, 235–46 (2011).
  56. Barrett, L. F. & Simmons, W. K. Interoceptive predictions in the brain. *Nat. Rev. Neurosci.* **16**, 419–429 (2015).
  57. Pitkow, X. & Angelaki, D. E. Inference in the brain: statistics flowing in redundant population codes. *Neuron* **94**, 943–953 (2017).
  58. Kahn, R. S. et al. Schizophrenia. *Nat. Rev. Dis. Prim.* **1**, 15067 (2015).
  59. Jablensky, A. The diagnostic concept of schizophrenia: its history, evolution, and future prospects. *Dialogues Clin Neurosci* **12**, 271–287 (2010).
  60. Carlsson, A. The current status of the dopamine hypothesis of schizophrenia. *Neuropsychopharmacology* **1**, 179–86 (1988).
  61. Berke, J. D. What does dopamine mean? *Nat. Neurosci.* **21**, 787–793 (2018).
  62. Abi-Dargham, A. Schizophrenia: overview and dopamine dysfunction. *J. Clin. Psychiatry* **75**, e31 (2014).
  63. Kapur, S. Psychosis as a state of aberrant salience: A framework linking biology, phenomenology and pharmacology in schizophrenia. *Am. J. Psychiatry* **160**, 13–23 (2003).
  64. Insel, T. R. Rethinking schizophrenia. *Nature* **468**, 187–93 (2010).
  65. Marín, O. Developmental timing and critical windows for the treatment of psychiatric disorders. *Nat. Med.* **22**, 1229–1238 (2016).
  66. Krol, A., Wimmer, R. D., Halassa, M. M. & Feng, G. Thalamic reticular dysfunction as a circuit endophenotype in neurodevelopmental disorders. *Neuron* **98**, 282–295 (2018).
  67. Horrobin, D. F. Schizophrenia: The illness that made us human. *Med. Hypotheses* **50**, 269–288 (1998).
  68. van Os, J. & Kapur, S. Schizophrenia. *Lancet* **374**, 635–45 (2009).
  69. Coyle, J. T. Glutamate and schizophrenia: beyond the dopamine hypothesis. *Cell. Mol. Neurobiol.* **26**, 365–84 (2006).
  70. Gonzalez-Burgos, G., Cho, R. Y. & Lewis, D. A. Alterations in cortical network oscillations and parvalbumin neurons in schizophrenia. *Biol. Psychiatry* **77**, 1031–1040 (2015).
  71. Fitzsimmons, J., Kubicki, M. & Shenton, M. E. Review of functional and anatomical brain connectivity findings in schizophrenia. *Curr. Opin. Psychiatry*

- 26**, 172–87 (2013).
72. Lewis, D. A., Curley, A. A., Glausier, J. R. & Volk, D. W. Cortical parvalbumin interneurons and cognitive dysfunction in schizophrenia. *Trends Neurosci.* **35**, 57–67 (2012).
  73. Gonzalez-Burgos, G., Hashimoto, T. & Lewis, D.A. Alterations of cortical GABA neurons and network oscillations in schizophrenia. *Curr. Psychiatry Rep.* **12**, 335–44 (2010).
  74. Hashimoto, T. et al. Alterations in GABA-related transcriptome in the dorsolateral prefrontal cortex of subjects with schizophrenia. *Mol. Psychiatry* **13**, 147–61 (2008).
  75. Thompson, M., Weickert, C. S., Wyatt, E. & Webster, M. J. Decreased glutamic acid decarboxylase(67) mRNA expression in multiple brain areas of patients with schizophrenia and mood disorders. *J. Psychiatr. Res.* **43**, 970–7 (2009).
  76. Woo, T.-U. W., Walsh, J. P. & Benes, F. M. Density of glutamic acid decarboxylase 67 messenger RNA-containing neurons that express the N-methyl-D-aspartate receptor subunit NR2A in the anterior cingulate cortex in schizophrenia and bipolar disorder. *Arch. Gen. Psychiatry* **61**, 649–57 (2004).
  77. Impagnatiello, F. A decrease of reelin expression as a putative vulnerability factor. *PNAS* **95**, 15718–15723 (1998).
  78. Guidotti, A. et al. Decrease in reelin and glutamic acid decarboxylase67 (GAD67) expression in schizophrenia and bipolar disorder: a postmortem brain study. *Arch. Gen. Psychiatry* **57**, 1061–9 (2000).
  79. Curley, A. A. et al. Cortical deficits of glutamic acid decarboxylase 67 expression in schizophrenia: clinical, protein, and cell type-specific features. *Am. J. Psychiatry* **168**, 921–9 (2011).
  80. Akbarian, S. et al. Gene expression for glutamic acid decarboxylase is reduced without loss of neurons in prefrontal cortex of schizophrenics. *Arch. Gen. Psychiatry* **52**, 258–66 (1995).
  81. Volk, D. W., Austin, M. C., Pierri, J. N., Sampson, A. R. & Lewis, D. A. Decreased glutamic acid decarboxylase67 messenger RNA expression in a subset of prefrontal cortical gamma-aminobutyric acid neurons in subjects with schizophrenia. *Arch. Gen. Psychiatry* **57**, 237–45 (2000).
  82. Hashimoto, T. et al. Gene expression deficits in a subclass of GABA neurons in the prefrontal cortex of subjects with schizophrenia. *J. Neurosci.* **23**, 6315–26 (2003).
  83. Hashimoto, T. et al. Conserved regional patterns of GABA-related transcript expression in the neocortex of subjects with schizophrenia. *Am. J. Psychiatry* **165**, 479–89 (2008).
  84. Mellios, N. et al. Molecular determinants of dysregulated GABAergic gene expression in the prefrontal cortex of subjects with schizophrenia. *Biol. Psychiatry* **65**, 1006–14 (2009).
  85. Fung, S. J. et al. Expression of interneuron markers in the dorsolateral prefrontal cortex of the developing human and in schizophrenia. *Am. J. Psychiatry* **167**, 1479–88 (2010).
  86. Glausier, J. R., Fish, K. N. & Lewis, D. A. Altered parvalbumin basket cell inputs in the dorsolateral prefrontal cortex of schizophrenia subjects. *Mol. Psychiatry* **19**, 30–6 (2014).
  87. Woo, T. U., Miller, J. L. & Lewis, D. A. Schizophrenia and the parvalbumin-containing class of cortical local circuit neurons. *Am. J. Psychiatry* **154**, 1013–5 (1997).
  88. Beasley, C. L., Zhang, Z. J., Patten, I. & Reynolds, G. P. Selective deficits in prefrontal cortical GABAergic neurons in schizophrenia defined by the presence of calcium-binding proteins. *Biol. Psychiatry* **52**, 708–15 (2002).
  89. Tooney, P. A. & Chahl, L. A. Neurons

- expressing calcium-binding proteins in the prefrontal cortex in schizophrenia. *Prog. Neuro-Psychopharmacology Biol. Psychiatry* **28**, 273–278 (2004).
90. Pantazopoulos, H., Woo, T.-U.W., Lim, M. P., Lange, N. & Berretta, S. Extracellular matrix-glia abnormalities in the amygdala and entorhinal cortex of subjects diagnosed with schizophrenia. *Arch. Gen. Psychiatry* **67**, 155–66 (2010).
  91. Donato, F., Rompani, S. B. & Caroni, P. Parvalbumin-expressing basket-cell network plasticity induced by experience regulates adult learning. *Nature* **504**, 272–6 (2013).
  92. Brown, J. A. et al. Inhibition of parvalbumin-expressing interneurons results in complex behavioral changes. *Mol. Psychiatry* **20**, 1499–507 (2015).
  93. Frankle, W. G., Cho, R. Y., Prasad, K. M., Mason, N. S. & Ph, D. In Vivo Measurement of GABA Transmission in healthy subjects and schizophrenia patients. *Am. J. Psy.* **172**, 1148–59. (2015).
  94. Hormuzdi, S. G. et al. Impaired electrical signaling disrupts gamma frequency oscillations in connexin 36-deficient mice. *Neuron* **31**, 487–95 (2001).
  95. Traub, R. D. et al. Gap junctions between interneuron dendrites can enhance synchrony of gamma oscillations in distributed networks. *J. Neurosci.* **21**, 9478–86 (2001).
  96. Whittington, M. A., Traub, R. D. & Jefferys, J. G. Synchronized oscillations in interneuron networks driven by metabotropic glutamate receptor activation. *Nature* **373**, 612–5 (1995).
  97. Senkowski, D. & Gallinat, J. Dysfunctional prefrontal gamma-band oscillations reflect working memory and other cognitive deficits in schizophrenia. *Biol. Psychiatry* **77**, 1010–1019 (2015).
  98. Uhlhaas, P.J. & Singer, W. Oscillations and neuronal dynamics in schizophrenia: The search for basic symptoms and translational opportunities. *Biol. Psychiatry* **77**, 1001–1009 (2014).
  99. Pocklington, A. J. et al. Novel Findings from CNVs implicate inhibitory and excitatory signaling complexes in schizophrenia. *Neuron* **86**, 1203–1214 (2015).
  100. Karayiort et al. Schizophrenia susceptibility associated with interstitial deletions of chromosome 22q11. *Proc. Natl. Acad. Sci. U. S. A.* **92**, 7612–6 (1995).
  101. Lindsay, E. A. et al. Schizophrenia and chromosomal deletions within 22q11.2. *Am. J. Hum. Genet.* **56**, 1502–3 (1995).
  102. Ellegood, J. et al. Neuroanatomical phenotypes in a mouse model of the 22q11.2 microdeletion. *Mol. Psychiatry* **19**, 99–107 (2014).
  103. Chun, S. et al. Specific disruption of thalamic inputs to the auditory cortex in schizophrenia models. *Science* **344**, 1178–82 (2014).
  104. Sigurdsson, T., Stark, K. L., Karayiorgou, M., Gogos, J.A. & Gordon, J.A. Impaired hippocampal–prefrontal synchrony in a genetic mouse model of schizophrenia. *Nature* **464**, 763–767 (2010).
  105. Meechan, D.W., Tucker, E. S., Maynard, T. M. & LaMantia, A.-S. Diminished dosage of 22q11 genes disrupts neurogenesis and cortical development in a mouse model of 22q11 deletion/DiGeorge syndrome. *Proc. Natl. Acad. Sci. U. S. A.* **106**, 16434–45 (2009).
  106. Rosen, A. M., Spellman, T. & Gordon, J. a. Electrophysiological endophenotypes in rodent models of schizophrenia and psychosis. *Biol. Psychiatry* **77**, 1041–1049 (2015).
  107. White, T. et al. Global white matter abnormalities in schizophrenia: a multisite diffusion tensor imaging study. *Schizophr. Bull.* **37**, 222–32 (2011).
  108. Alvarado-Alanis, P. et al. Abnormal white matter integrity in antipsychotic-naïve first-episode psychosis patients assessed by a DTI principal component analysis. *Schizophr. Res.* **162**, 14–21

- (2015).
109. Cheung, V. et al. A diffusion tensor imaging study of structural dysconnectivity in never-medicated, first-episode schizophrenia. *Psychol. Med.* **38**, 877–85 (2008).
  110. Liu, X. et al. A combined DTI and structural MRI study in medicated-naïve chronic schizophrenia. *Magn. Reson. Imaging* **32**, 1–8 (2014).
  111. Sun, H. et al. Two patterns of white matter abnormalities in medication-naïve patients with first-episode schizophrenia revealed by diffusion tensor imaging and cluster analysis. *JAMA psychiatry* **72**, 678–86 (2015).
  112. Yao, L. et al. Association of white matter deficits with clinical symptoms in antipsychotic-naïve first-episode schizophrenia: an optimized VBM study using 3T. *MAGMA* **27**, 283–90 (2014).
  113. Wang, Q. et al. White-matter microstructure in previously drug-naïve patients with schizophrenia after 6 weeks of treatment. *Psychol. Med.* **43**, 2301–9 (2013).
  114. Filippi, M. et al. Patterns of brain structural changes in first-contact, antipsychotic drug-naïve patients with schizophrenia. *Am. J. Neuroradiol.* **35**, 30–37 (2013).
  115. Gasparotti, R. et al. Reduced fractional anisotropy of corpus callosum in first-contact, antipsychotic drug-naïve patients with schizophrenia. *Schizophr. Res.* **108**, 41–8 (2009).
  116. Guo, W. et al. Right lateralized white matter abnormalities in first-episode, drug-naïve paranoid schizophrenia. *Neurosci. Lett.* **531**, 5–9 (2012).
  117. Pérez-Iglesias, R. et al. White matter defects in first episode psychosis patients: a voxelwise analysis of diffusion tensor imaging. *Neuroimage* **49**, 199–204 (2010).
  118. Mandl, R. C. W. et al. Altered white matter connectivity in never-medicated patients with schizophrenia. *Hum. Brain Mapp.* **34**, 2353–65 (2013).
  119. Melicher, T. et al. White matter changes in first episode psychosis and their relation to the size of sample studied: a DTI study. *Schizophr. Res.* **162**, 22–8 (2015).
  120. Lener, M. S. et al. White matter abnormalities in schizophrenia and schizotypal personality disorder. *Schizophr. Bull.* **41**, 300–10 (2015).
  121. Lyu, H. et al. Regional white matter abnormalities in drug-naïve, first-episode schizophrenia patients and their healthy unaffected siblings. *Aust. N. Z. J. Psychiatry* **49**, 246–54 (2015).
  122. Do, K. Q., Cuenod, M. & Hensch, T. K. Targeting oxidative stress and aberrant critical period plasticity in the developmental trajectory to schizophrenia. *Schizophr. Bull.* **41**, 835–46 (2015).
  123. Hermoye, L. et al. Pediatric diffusion tensor imaging: normal database and observation of the white matter maturation in early childhood. *Neuroimage* **29**, 493–504 (2006).
  124. Lebel, C., Walker, L., Leemans, A., Phillips, L. & Beaulieu, C. Microstructural maturation of the human brain from childhood to adulthood. *Neuroimage* **40**, 1044–55 (2008).
  125. Lebel, C. et al. Diffusion tensor imaging of white matter tract evolution over the lifespan. *Neuroimage* **60**, 340–52 (2012).
  126. Miller, D. J. et al. Prolonged myelination in human neocortical evolution. *Proc. Natl. Acad. Sci. U. S. A.* **109**, 16480–5 (2012).
  127. Tkachev, D. et al. Oligodendrocyte dysfunction in schizophrenia and bipolar disorder. *Lancet* **362**, 798–805 (2003).
  128. Hakak, Y. et al. Genome-wide expression analysis reveals dysregulation of myelination-related genes in chronic

- schizophrenia. *Proc. Natl. Acad. Sci. U. S. A.* **98**, 4746–51 (2001).
129. Barley, K., Dracheva, S. & Byne, W. Subcortical oligodendrocyte- and astrocyte-associated gene expression in subjects with schizophrenia, major depression and bipolar disorder. *Schizophr. Res.* **112**, 54–64 (2009).
130. Katsel, P., Davis, K. L., Gorman, J. M. & Haroutunian, V. Variations in differential gene expression patterns across multiple brain regions in schizophrenia. *Schizophr. Res.* **77**, 241–52 (2005).
131. Aberg, K., Saetre, P., Jareborg, N. & Jazin, E. Human QKI, a potential regulator of mRNA expression of human oligodendrocyte-related genes involved in schizophrenia. *Proc. Natl. Acad. Sci. U. S. A.* **103**, 7482–7 (2006).
132. Schmitt, A. et al. Altered thalamic membrane phospholipids in schizophrenia: a postmortem study. *Biol. Psychiatry* **56**, 41–5 (2004).
133. Matthews, P. R., Eastwood, S. L. & Harrison, P. J. Reduced myelin basic protein and actin-related gene expression in visual cortex in schizophrenia. *PLoS One* **7**, e38211 (2012).
134. Aston, C., Jiang, L. & Sokolov, B. P. Microarray analysis of postmortem temporal cortex from patients with schizophrenia. *J. Neurosci. Res.* **77**, 858–866 (2004).
135. Harris, L. W. et al. Gene expression in the prefrontal cortex during adolescence: implications for the onset of schizophrenia. *BMC Med. Genomics* **2**, 28 (2009).
136. Hof, P. R., Haroutunian, V., Copland, C., Davis, K. L. & Buxbaum, J. D. Molecular and cellular evidence for an oligodendrocyte abnormality in schizophrenia. *Neurochem. Res.* **27**, 1193–200 (2002).
137. Hof, P. R. et al. Loss and altered spatial distribution of oligodendrocytes in the superior frontal gyrus in schizophrenia. *Biol. Psychiatry* **53**, 1075–85 (2003).
138. Mauney, S. A., Pietersen, C. Y., Sonntag, K.-C. & Woo, T.-U. W. Differentiation of oligodendrocyte precursors is impaired in the prefrontal cortex in schizophrenia. *Schizophr. Res.* **169**, 374–80 (2015).
139. Uranova, N. A. et al. Ультраструктурная патология миелиновых волокон при шизофрении. *Zhurnal Nevrol. i psikhiatrii Im. S.S. Korsakova / Minist. Zdr. i meditsins* **9**, 63–69 (2013).
140. Uranova, N. A. et al. The role of oligodendrocyte pathology in schizophrenia. *Int. J. Neuropsychopharmacol.* **10**, 537–545 (2007).
141. Vostrikov, V. M., Uranova, N. A., Rakhmanova, V. I. & Orlovskaya, D. D. [Lowered oligodendroglial cell density in the prefrontal cortex in schizophrenia]. *Zh. Nevrol. Psikhiatr. Im. S. S. Korsakova* **104**, 47–51 (2004).
142. Uranova, N. A., Vostrikov, V. M., Orlovskaya, D. D. & Rakhmanova, V. I. Oligodendroglial density in the prefrontal cortex in schizophrenia and mood disorders: A study from the Stanley Neuropathology Consortium. *Schizophr. Res.* **67**, 269–275 (2004).
143. Schmitt, A. et al. Stereologic investigation of the posterior part of the hippocampus in schizophrenia. *Acta Neuropathol.* **117**, 395–407 (2009).
144. Kerns, D. et al. Gene expression abnormalities and oligodendrocyte deficits in the internal capsule in schizophrenia. *Schizophr. Res.* **120**, 150–8 (2010).
145. Williams, M. R. et al. Neuropathological changes in the nucleus basalis in schizophrenia. *Eur. Arch. Psychiatry Clin. Neurosci.* **263**, 485–95 (2013).
146. Byne, W., Tatusov, A., Yiannoukos, G., Yong, G. S. & Marcus, S. Effects of mental illness and aging in two thalamic nuclei. *Schizophr. Res.* **106**, 172–81 (2008).

147. Williams, M. R. et al. Neuropathological changes in the substantia nigra in schizophrenia but not depression. *Eur. Arch. Psychiatry Clin. Neurosci.* **264**, 285–96 (2014).
148. Williams, M. R. et al. Astrocyte decrease in the subgenual cingulate and callosal genu in schizophrenia. *Eur. Arch. Psychiatry Clin. Neurosci.* **263**, 41–52 (2013).
149. Chambers, J. S. & Perrone-Bizzozero, N. I. Altered myelination of the hippocampal formation in subjects with schizophrenia and bipolar disorder. *Neurochem. Res.* **29**, 2293–302 (2004).
150. Bernstein, H.-G. et al. Increased density of prohibitin-immunoreactive oligodendrocytes in the dorsolateral prefrontal white matter of subjects with schizophrenia suggests extraneuronal roles for the protein in the disease. *Neuromolecular Med.* **14**, 270–80 (2012).
151. Williams, M. R., Harb, H., Pearce, R. K. B., Hirsch, S. R. & Maier, M. Oligodendrocyte density is changed in the basolateral amygdala in schizophrenia but not depression. *Schizophr. Res.* **147**, 402–403 (2013).
152. Miyakawa, T., Sumiyoshi, S., Deshimaru, M., Suzuki, T. & Tomonari, H. Electron microscopic study on schizophrenia. Mechanism of pathological changes. *Acta Neuropathol.* **20**, 67–77 (1972).
153. Uranova, N. A., Vikhreva, O. V., Rachmanova, V. I. & Orlovskaya, D. D. Ultrastructural alterations of myelinated fibers and oligodendrocytes in the prefrontal cortex in schizophrenia: A postmortem morphometric study. *Schizophr. Res. Treatment* **2011**, 1–13 (2011).
154. Toritsuka, M., Makinodan, M. & Kishimoto, T. Social experience-dependent myelination: An implication for psychiatric disorders. *Neural Plast.* **2015**, 465345 (2015).
155. Duncan, L. E. et al. Pathway analyses implicate glial cells in schizophrenia. *PLoS One* **9**, e89441 (2014).
156. Goudriaan, A. et al. Specific glial functions contribute to schizophrenia susceptibility. *Schizophr. Bull.* **40**, 925–35 (2014).
157. Xu, K., Schadt, E. E., Pollard, K. S., Roussos, P. & Dudley, J. T. Genomic and network patterns of schizophrenia genetic variation in human evolutionary accelerated regions. *Mol. Biol. Evol.* **32**, 1148–1160 (2015).
158. Chavarria-Siles, I. et al. Myelination-related genes are associated with decreased white matter integrity in schizophrenia. *Eur. J. Hum. Genet.* **24**, 381–6 (2016).
159. Ripke, S. et al. Biological insights from 108 schizophrenia-associated genetic loci. *Nature* **511**, 421–7 (2014).
160. McGee, A. W., Yang, Y., Fischer, Q. S., Daw, N. W. & Strittmatter, S. M. Experience-driven plasticity of visual cortex limited by myelin and Nogo receptor. *Science* **309**, 2222–2226 (2005).
161. Somogyi, P. & Soltész, I. Immunogold demonstration of GABA in synaptic terminals of intracellularly recorded, horseradish peroxidase-filled basket cells and clutch cells in the cat's visual cortex. *Neuroscience* **19**, 1051–65 (1986).
162. DeFelipe, J. & Jones, E. G. Vertical organization of gamma-aminobutyric acid-accumulating intrinsic neuronal systems in monkey cerebral cortex. *J. Neurosci.* **5**, 3246–60 (1985).
163. DeFelipe, J., Hendry, S. H. & Jones, E. G. A correlative electron microscopic study of basket cells and large GABAergic neurons in the monkey sensory-motor cortex. *Neuroscience* **17**, 991–1009 (1986).
164. Takasu, N., Nakatani, T., Arikuni, T. & Kimura, H. Immunocytochemical localization of gamma-aminobutyric acid in the hypoglossal nucleus of the

- macaque monkey, *Macaca fuscata*: a light and electron microscopic study. *J. Comp. Neurol.* **263**, 42–53 (1987).
165. Ralston, D. D. & Milroy, A. M. Inhibitory synaptic input to identified rubrospinal neurons in *Macaca fascicularis*: an electron microscopic study using a combined immuno-GABA-gold technique and the retrograde transport of WGA-HRP. *J. Comp. Neurol.* **320**, 97–109 (1992).
166. Jinno, S. et al. Neuronal diversity in GABAergic long-range projections from the hippocampus. *J. Neurosci.* **27**, 8790–804 (2007).
167. Peters, A. & Proskauer, C. C. Smooth or sparsely spined cells with myelinated axons in rat visual cortex. *Neuroscience* **5**, 2079–92 (1980).
168. De Biasi, S., Amadeo, A., Arcelli, P., Frassoni, C. & Spreafico, R. Postnatal development of GABA-immunoreactive terminals in the reticular and ventrobasal nuclei of the rat thalamus: a light and electron microscopic study. *Neuroscience* **76**, 503–15 (1997).
169. Conti, F. et al. Neuronal, glial, and epithelial localization of gamma-aminobutyric acid transporter 2, a high-affinity gamma-aminobutyric acid plasma membrane transporter, in the cerebral cortex and neighboring structures. *J. Comp. Neurol.* **409**, 482–94 (1999).
170. Gartner, U., Hartig, C. A. W., Brauer, K., Bru, G. & Arendt, T. Electron microscopic evidence for different myelination of rat septohippocampal fibres. *Neuroreport* **12**, 17–20 (2001).
171. Gartner, U., Brauer, K., Hartig, W., Bruckner, G. & Arendt, T. Different myelination of rat septohippocampal fibres as revealed by immunofluorescence double-labelling. *Brain Res.* **878**, 188–193 (2000).
172. Somogyi, P., Kisvárdy, Z. F., Martin, K. A. & Whitteridge, D. Synaptic connections of morphologically identified and physiologically characterized large basket cells in the striate cortex of cat. *Neuroscience* **10**, 261–94 (1983).
173. Freeman, S. A., Desmazières, A., Simonnet, J., Gatta, M. & Pfeiffer, F. Acceleration of conduction velocity linked to clustering of nodal components precedes myelination. *Proc. Natl. Acad. Sci. U. S. A.* **112**, E321–8 (2014).
174. Mize, R. R. Immunocytochemical localization of gamma-aminobutyric acid (GABA) in the cat superior colliculus. *J. Comp. Neurol.* **276**, 169–87 (1988).
175. Wouterlood, F. G., Härtig, W., Brückner, G. & Witter, M. P. Parvalbumin-immunoreactive neurons in the entorhinal cortex of the rat: localization, morphology, connectivity and ultrastructure. *J. Neurocytol.* **24**, 135–53 (1995).
176. Sawyer, S. F., Martone, M. E. & Groves, P. M. A GABA immunocytochemical study of rat motor thalamus: light and electron microscopic observations. *Neuroscience* **42**, 103–24 (1991).
177. Roberts. An electron microscopic study of GABAergic neurons and terminals in the central nucleus of the inferior colliculus of the rat. *Journal of neurocytology* **16**, 333–45 (1987).
178. Katsumaru, H., Kosaka, T., Heizmann, C. W. & Hama, K. Immunocytochemical study of GABAergic neurons containing the calcium-binding protein parvalbumin in the rat hippocampus. *Exp. Brain Res.* **72**, 347–62 (1988).
179. Kita, H., Kosaka, T. & Heizmann, C. W. Parvalbumin-immunoreactive neurons in the rat neostriatum: a light and electron microscopic study. *Brain Res.* **536**, 1–15 (1990).
180. Somogyi, P., Freund, T. F., Wu, J. Y. & Smith, A. D. The section-Golgi impregnation procedure. 2. Immunocytochemical demonstration of glutamate

- decarboxylase in Golgi-impregnated neurons and in their afferent synaptic boutons in the visual cortex of the cat. *Neuroscience* **9**, 475–90 (1983).
181. Chung, K. et al. Structural and molecular interrogation of intact biological systems. *Nature* **497**, 332–7 (2013).
182. Ong, W. Y., Yeo, T. T., Balcar, V. J. & Garey, L. J. A light and electron microscopic study of GAT-1-positive cells in the cerebral cortex of man and monkey. *J. Neurocytol.* **27**, 719–30 (1998).
183. Seress, L. et al. Distribution, morphological features, and synaptic connections of parvalbumin- and calbindin D28k-immunoreactive neurons in the human hippocampal formation. *J. Comp. Neurol.* **337**, 208–30 (1993).
184. Hinova-Palova, D. V. et al. Parvalbumin-immunoreactive neurons in the human claustrum. *Brain Struct. Funct.* **219**, 1813–30 (2014).
185. Sloper, J. J. & Powell, T. P. A study of the axon initial segment and proximal axon of neurons in the primate motor and somatic sensory cortices. *Philos. Trans. R. Soc. Lond. B. Biol. Sci.* **285**, 173–97 (1979).
186. Hendry, S. H., Houser, C. R., Jones, E. G. & Vaughn, J. E. Synaptic organization of immunocytochemically identified GABA neurons in the monkey sensory-motor cortex. *J. Neurocytol.* **12**, 639–60 (1983).
187. Brauer, K., Härtig, W., Gärtner, U., Brückner, G. & Arendt, T. Different myelination of rat septohippocampal fibres as revealed by immunofluorescence double-labelling. *Brain Res.* **878**, 188–93 (2000).
188. Aoki, C. & Pickel, V. M. Neuropeptide Y in cortex and striatum. Ultrastructural distribution and coexistence with classical neurotransmitters and neuropeptides. *Ann. N.Y. Acad. Sci.* **611**, 186–205 (1990).
189. Cipolloni, P. B. & Keller, A. Thalamocortical synapses with identified neurons in monkey primary auditory cortex: a combined Golgi/EM and GABA/peptide immunocytochemistry study. *Brain Res.* **492**, 347–55 (1989).
190. Mizukawa, K., McGeer, P. L., Vincent, S. R. & McGeer, E. G. The distribution of somatostatin-immunoreactive neurons and fibers in the rat cerebral cortex: light and electron microscopic studies. *Brain Res.* **426**, 28–36 (1987).
191. de Lima, A. D. & Morrison, J. H. Ultrastructural analysis of somatostatin-immunoreactive neurons and synapses in the temporal and occipital cortex of the macaque monkey. *J. Comp. Neurol.* **283**, 212–27 (1989).
192. DiFiglia, M. & Aronin, N. Ultrastructural features of immunoreactive somatostatin neurons in the rat caudate nucleus. *J. Neurosci.* **2**, 1267–74 (1982).
193. Hinova-Palova, D. V. et al. Neuropeptide Y immunoreactivity in the cat claustrum: A light- and electron-microscopic investigation. *J. Chem. Neuroanat.* **61–62**, 107–19 (2014).
194. Orduz, D. et al. Interneurons and oligodendrocyte progenitors form a structured synaptic network in the developing neocortex. *Elife* **4**, 1–20 (2015).
195. Zonouzi, M. et al. GABAergic regulation of cerebellar NG2 cell development is altered in perinatal white matter injury. *Nat. Neurosci.* **18**, 674–82 (2015).
196. Le Magueresse, C. & Monyer, H. GABAergic interneurons shape the functional maturation of the cortex. *Neuron* **77**, 388–405 (2013).
197. Hill, R. A., Patel, K. D., Medved, J., Reiss, A. M. & Nishiyama, A. NG2 cells in white matter but not gray matter proliferate in response to PDGF. *J. Neurosci.* **33**, 14558–66 (2013).
198. Lin, S. & Bergles, D. E. Synaptic signaling between GABAergic interneurons and

- oligodendrocyte precursor cells in the hippocampus. *Nat. Neurosci.* **7**, 24–32 (2004).
199. Fino, E., Packer, A. M. & Yuste, R. The logic of inhibitory connectivity in the neocortex. *Neuroscientist* **19**, 228–37 (2013).
  200. Hu, H., Gan, J. & Jonas, P. Fast-spiking, parvalbumin+ GABAergic interneurons: From cellular design to microcircuit function. *Science*. **345**, 1255263–1255263 (2014).
  201. Jadi, M. P., Margarita Behrens, M. & Sejnowski, T. J. Abnormal Gamma Oscillations in N-Methyl-D-Aspartate Receptor Hypofunction Models of Schizophrenia. *Biol. Psychiatry* **79**, 716–26 (2015).
  202. Yamazaki, Y. et al. Short- and long-term functional plasticity of white matter induced by oligodendrocyte depolarization in the hippocampus. *Glia* **62**, 1299–312 (2014).
  203. Pajevic, S., Basser, P. J. & Fields, R. D. Role of myelin plasticity in oscillations and synchrony of neuronal activity. *Neuroscience* **276**, 135–147 (2014).
  204. Salami, M., Itami, C., Tsumoto, T. & Kimura, F. Change of conduction velocity by regional myelination yields constant latency irrespective of distance between thalamus and cortex. *Proc. Natl. Acad. Sci. U. S. A.* **100**, 6174–9 (2003).
  205. Kann, O., Papageorgiou, I. E. & Draguhn, A. Highly energized inhibitory interneurons are a central element for information processing in cortical networks. *J. Cereb. Blood Flow Metab.* **34**, 1270–82 (2014).
  206. Inan, M. et al. Energy deficit in parvalbumin neurons leads to circuit dysfunction, impaired sensory gating and social disability. *Neurobiol. Dis.* **93**, 35–46 (2016).
  207. Kasthuri, N. et al. Saturated reconstruction of a volume of neocortex. *Cell* **162**, 648–661 (2015).
  208. Gibson, E. M. et al. Neuronal Activity promotes oligodendrogenesis and adaptive myelination in the mammalian brain. *Science*. **344**, 1252304 (2014).
  209. Makinodan, M., Rosen, K. M., Ito, S. & Corfas, G. A critical period for social experience-dependent oligodendrocyte maturation and myelination. *Science* **337**, 1357–60 (2012).
  210. Liu, J. et al. Impaired adult myelination in the prefrontal cortex of socially isolated mice. *Nat. Neurosci.* **15**, 1621–3 (2012).
  211. Kumar, J. et al. Shared white-matter dysconnectivity in schizophrenia and bipolar disorder with psychosis. *Psychol. Med.* **45**, 759–770 (2015).
  212. Barysheva, M., Jahanshad, N., Foland-Ross, L., Altshuler, L. L. & Thompson, P. M. White matter microstructural abnormalities in bipolar disorder: A whole brain diffusion tensor imaging study. *NeuroImage Clin.* **2**, 558–568 (2013).
  213. White, T. et al. Spatial characteristics of white matter abnormalities in schizophrenia. *Schizophr. Bull.* **39**, 1077–86 (2013).
  214. Rane, P. et al. Connectivity in autism: A review of MRI connectivity studies. *Harv. Rev. Psychiatry* **23**, 223–44 (2015).
  215. Tomassy, G. S. et al. Distinct profiles of myelin distribution along single axons of pyramidal neurons in the neocortex. *Science*. **344**, 319–324 (2014).
  216. Micheva, K. D. et al. A large fraction of neocortical myelin ensheathes axons of local inhibitory neurons. *Elife* **5**, e15784 (2016).
  217. Stedehouder, J. & Kushner, S. A. Myelination of parvalbumin interneurons: a parsimonious locus of pathophysiological convergence in schizophrenia. *Mol. Psychiatry* **22**, 4–12 (2017).
  218. Schain, A. J., Hill, R. A. & Grutzendler, J.

- Label-free in vivo imaging of myelinated axons in health and disease with spectral confocal reflectance microscopy. *Nat. Med.* **20**, 443–9 (2014).
219. Povysheva, N. V., Zaitsev, A. V., Gonzalez-Burgos, G. & Lewis, D. A. Electrophysiological Heterogeneity of Fast-Spiking Interneurons: Chandelier versus Basket Cells. *PLoS One* **8**, (2013).
  220. Povysheva, N. V et al. Parvalbumin-positive basket interneurons in monkey and rat prefrontal cortex. *J. Neurophysiol.* **100**, 2348–60 (2008).
  221. Urban-Ciecko, J. & Barth, A. L. Somatostatin-expressing neurons in cortical networks. *Nat. Rev. Neurosci.* **17**, 401–9 (2016).
  222. Li, T. et al. Action Potential Initiation in Neocortical Inhibitory Interneurons. *PLoS Biol.* **12**, e1001944 (2014).
  223. Hu, H. & Jonas, P. A supercritical density of Na(+) channels ensures fast signaling in GABAergic interneuron axons. *Nat. Neurosci.* **17**, 686–93 (2014).
  224. Clark, B. A., Monsivais, P., Branco, T., London, M. & Häusser, M. The site of action potential initiation in cerebellar Purkinje neurons. *Nat. Neurosci.* **8**, 137–139 (2005).
  225. Hamada, M. S. & Kole, M. H. P. Myelin loss and axonal ion channel adaptations associated with gray matter neuronal hyperexcitability. *J. Neurosci.* **35**, 7272–86 (2015).
  226. Brown, D. A., Higgins, A. J., Marsh, S. & Smart, T. G. Actions of GABA on mammalian neurones, axons, and nerve terminals. *Adv. Biochem. Psychopharmacol.* **29**, 321–6 (1981).
  227. McCormick, D. A., Connors, B. W., Lighthall, J. W. & Prince, D. A. Comparative electrophysiology of pyramidal and sparsely spiny stellate neurons of the neocortex. *J. Neurophysiol.* **54**, 782–806 (1985).
  228. Lacaille, J. C., Mueller, A. L., Kunkel, D. D. & Schwartzkroin, P. A. Local circuit interactions between oriens/alveus interneurons and CA1 pyramidal cells in hippocampal slices: electrophysiology and morphology. *J. Neurosci.* **7**, 1979–93 (1987).
  229. Beaulieu, C., Dyck, R. & Cynader, M. Enrichment of glutamate in zinc-containing terminals of the cat visual cortex. *Neuroreport* **3**, 861–4 (1992).
  230. Buonomano, D. V. Decoding temporal information: A model based on short-term synaptic plasticity. *J. Neurosci.* **20**, 1129–41 (2000).
  231. Voronova, A. et al. Migrating interneurons secrete fractalkine to promote oligodendrocyte formation in the developing mammalian brain. *Neuron* **94**, 500–516.e9 (2017).
  232. Marques, S. et al. Oligodendrocyte heterogeneity in the mouse juvenile and adult central nervous system. *Science* **352**, 1326–9 (2016).
  233. Hippenmeyer, S. et al. A developmental switch in the response of DRG neurons to ETS transcription factor signaling. *PLoS Biol.* **3**, e159 (2005).
  234. Taniguchi, H. et al. A resource of Cre driver lines for genetic targeting of GABAergic neurons in cerebral cortex. *Neuron* **71**, 995–1013 (2011).
  235. Madisen, L. et al. A toolbox of Cre-dependent optogenetic transgenic mice for light-induced activation and silencing. *Nat. Neurosci.* **15**, 793–802 (2012).
  236. Chernoff, G. F. Shiverer: an autosomal recessive mutant mouse with myelin deficiency. *J. Hered.* **72**, 128 (1981).
  237. Pala, A. & Petersen, C. C. H. In vivo measurement of cell-type-specific synaptic connectivity and synaptic transmission in layer 2/3 mouse barrel cortex. *Neuron* **85**, 68–75 (2015).
  238. Hu, H., Cavendish, J. Z. & Agmon, A. Not all that glitters is gold: off-target recombination in the somatostatin-IRES-Cre mouse line labels a subset of

- fast-spiking interneurons. *Front. Neural Circuits* **7**, 195 (2013).
239. Müller, C. & Remy, S. Dendritic inhibition mediated by O-LM and bistratified interneurons in the hippocampus. *Front. Synaptic Neurosci.* **6**, 23 (2014).
  240. Stedehouder, J. et al. Fast-spiking parvalbumin interneurons are frequently myelinated in the cerebral cortex of mice and humans. *Cereb. Cortex* **39**, 1–13 (2017).
  241. Hines, J. H., Ravanelli, A. M., Schwandt, R., Scott, E. K. & Appel, B. Neuronal activity biases axon selection for myelination in vivo. *Nat. Neurosci.* **18**, 683–9 (2015).
  242. Mensch, S. et al. Synaptic vesicle release regulates myelin sheath number of individual oligodendrocytes in vivo. *Nat. Neurosci.* **18**, 628–30 (2015).
  243. Armbruster, B. N., Li, X., Pausch, M. H., Herlitze, S. & Roth, B. L. Evolving the lock to fit the key to create a family of G protein-coupled receptors potently activated by an inert ligand. *Proc. Natl. Acad. Sci.* **104**, 5163–5168 (2007).
  244. Yamada, A. et al. Role of pre- and postsynaptic activity in thalamocortical axon branching. *Proc. Natl. Acad. Sci.* **107**, 7562–7567 (2010).
  245. Chéreau, R., Saraceno, G. E., Angibaud, J., Cattaert, D. & Nägerl, U. V. Superresolution imaging reveals activity-dependent plasticity of axon morphology linked to changes in action potential conduction velocity. *Proc. Natl. Acad. Sci.* **114**, 1401–1406 (2017).
  246. Lee, S. et al. A culture system to study oligodendrocyte myelination processes using engineered nanofibers. *Nat. Methods* **9**, 917–922 (2012).
  247. Bechler, M. E., Byrne, L. & French-Constant, C. CNS Myelin sheath lengths are an intrinsic property of oligodendrocytes. *Curr. Biol.* **25**, 2411–2416 (2015).
  248. Wake, H. et al. Nonsynaptic junctions on myelinating glia promote preferential myelination of electrically active axons. *Nat. Commun.* **6**, 7844 (2015).
  249. DeFelipe, J. et al. New insights into the classification and nomenclature of cortical GABAergic interneurons. *Nat. Rev. Neurosci.* **14**, 202–216 (2013).
  250. Miyamae, T., Chen, K., Lewis, D. A. & Gonzalez-Burgos, G. Distinct physiological maturation of parvalbumin-positive neuron subtypes in mouse prefrontal cortex. *J. Neurosci.* **37**, 4883–4902 (2017).
  251. Simons, M. & Nave, K.-A. Oligodendrocytes: Myelination and Axonal Support. *Cold Spring Harb. Perspect. Biol.* **8**, a020479 (2015).
  252. Stedehouder, J., Brizee, D., Shpak, G. & Kushner, S. A. Activity-dependent myelination of parvalbumin interneurons mediated by axonal morphological plasticity. *J. Neurosci.* **38**, 3631–3642 (2018).
  253. Duncan D. The importance of diameter as a factor in myelination. *Science.* **79**, 363 (1934).
  254. Goebbels, S. et al. A neuronal PI(3,4,5)P3-dependent program of oligodendrocyte precursor recruitment and myelination. *Nat. Neurosci.* **20**, 10–15 (2017).
  255. Auer, F., Vagionitis, S. & Czopka, T. Evidence for myelin sheath remodeling in the CNS revealed by in vivo imaging. *Curr. Biol.* **28**, 549–559.e3 (2018).
  256. Stedehouder, J., Brizee, D., Shpak, G. & Kushner, S. A. Activity-dependent myelination of parvalbumin interneurons mediated by axonal morphological plasticity. *J. Neurosci.* **38**, 3631–3642 (2018).
  257. Hanley, A. J. & McNeil, J. B. The Meaning and Use of the Area under a Receiver Operating Characteristic (ROC) Curve. *Radiology* **143**, 29–36 (1982).
  258. Jin, H. & Lu, Y. The ROC region of a regression tree. *Stat. Probab. Lett.* **79**, 936–942 (2009).
  259. Karube, F. Axon Branching and Synaptic

- Bouton phenotypes in GABAergic nonpyramidal cell subtypes. *J. Neurosci.* **24**, 2853–2865 (2004).
260. Nörenberg, A., Hu, H., Vida, I., Bartos, M. & Jonas, P. Distinct nonuniform cable properties optimize rapid and efficient activation of fast-spiking GABAergic interneurons. *Proc. Natl. Acad. Sci.* **107**, 894–899 (2010).
  261. Fu, C. et al. GABAergic interneuron development and function is modulated by the *Tsc1* gene. *Cereb. Cortex* **22**, 2111–2119 (2012).
  262. Normand, E. A. et al. Temporal and mosaic *Tsc1* deletion in the developing thalamus disrupts thalamocortical circuitry, neural function, and behavior. *Neuron* **78**, 895–909 (2013).
  263. Meikle, L. et al. A Mouse model of tuberous sclerosis: Neuronal loss of *Tsc1* causes dysplastic and ectopic neurons, reduced myelination, seizure activity, and limited survival. *J. Neurosci.* **27**, 5546–5558 (2007).
  264. Carson, R. P., Van Nielen, D. L., Winzenburger, P. A. & Ess, K. C. Neuronal and glia abnormalities in *Tsc1*-deficient forebrain and partial rescue by rapamycin. *Neurobiol. Dis.* **45**, 369–380 (2012).
  265. Markus, A., Zhong, J. & Snider, W. D. Raf and Akt mediate distinct aspects of sensory axon growth. *Neuron* **35**, 65–76 (2002).
  266. Sidorov, M. S. et al. Enhanced operant extinction and prefrontal excitability in a mouse model of Angelman Syndrome. *J. Neurosci.* **38**, 2671–2682 (2018).
  267. Wallace, M. L., Burette, A. C., Weinberg, R. J. & Philpot, B. D. Maternal loss of *Ube3a* produces an excitatory/inhibitory imbalance through neuron type-specific synaptic defects. *Neuron* **74**, 793–800 (2012).
  268. Judson, M. C. et al. Decreased axon caliber underlies loss of fiber tract integrity, disproportional reductions in white matter volume, and microcephaly in Angelman syndrome model mice. *J. Neurosci.* **37**, 7347–7361 (2017).
  269. Redmond, S. A. et al. Somatodendritic expression of *JAM2* inhibits oligodendrocyte myelination. *Neuron* **91**, 824–836 (2016).
  270. Chong, S. Y. C. et al. Neurite outgrowth inhibitor Nogo-A establishes spatial segregation and extent of oligodendrocyte myelination. *Proc. Natl. Acad. Sci. U. S. A.* **109**, 1299–304 (2012).
  271. Freeman, S. A. et al. Acceleration of conduction velocity linked to clustering of nodal components precedes myelination. *Proc. Natl. Acad. Sci. U. S. A.* **112**, E321–8 (2015).
  272. Strüber, M., Jonas, P. & Bartos, M. Strength and duration of perisomatic GABAergic inhibition depend on distance between synaptically connected cells. *Proc. Natl. Acad. Sci.* **112**, 201412996 (2015).
  273. Balia, M., Benamer, N. & Angulo, M. C. A specific GABAergic synapse onto oligodendrocyte precursors does not regulate cortical oligodendrogenesis. *Glia* **65**, 1821–1832 (2017).
  274. Markram, H. et al. Interneurons of the neocortical inhibitory system. *Nat. Rev. Neurosci.* **5**, 793–807 (2004).
  275. Fields, R. D. A new mechanism of nervous system plasticity: activity-dependent myelination. *Nat. Rev. Neurosci.* **16**, 756–67 (2015).
  276. Caputi, A., Melzer, S., Michael, M. & Monyer, H. The long and short of GABAergic neurons. *Curr. Opin. Neurobiol.* **23**, 179–186 (2013).
  277. Melzer, S. et al. Distinct corticostriatal GABAergic neurons modulate striatal output neurons and motor activity. *Cell Rep.* **19**, 1045–1055 (2017).
  278. Rock, C., Zurita, H., Wilson, C. & Apicella, A. J. An inhibitory corticostriatal pathway. *Elife* **5**, 1–17 (2016).
  279. Lee, A. T., Vogt, D., Rubenstein, J. L. & Sohal, V. S. A Class of GABAergic

- neurons in the prefrontal cortex sends long-range projections to the nucleus accumbens and elicits acute avoidance behavior. *J. Neurosci.* **34**, 11519–11525 (2014).
280. Dimou, L. & Simons, M. Diversity of oligodendrocytes and their progenitors. *Curr. Opin. Neurobiol.* **47**, 73–79 (2017).
  281. Judson, M. C. et al. GABAergic neuron-specific loss of Ube3a causes Angelman syndrome-like EEG abnormalities and enhances seizure susceptibility. *Neuron* **90**, 56–69 (2016).
  282. Longair, M. H., Baker, D. A. & Armstrong, J. D. Simple Neurite Tracer: Open source software for reconstruction, visualization and analysis of neuronal processes. *Bioinformatics* **27**, 2453–2454 (2018).
  283. Sanders F.K, Whitteridge, D. Conduction velocity and myelin thickness in regenerating nerve fibers. *J. Physiol.* **105**, 152–174 (1946).
  284. Hu, H. et al. Complementary Tuning of Na<sup>+</sup> and K<sup>+</sup> Channel Gating Underlies Fast and Energy-Efficient Action Potentials in GABAergic Interneuron Axons. *Neuron* **98**, 156–164.e6 (2018).
  285. Rasband, M. N. The axon initial segment and the maintenance of neuronal polarity. *Nat. Rev. Neurosci.* **11**, 552–562 (2010).
  286. Schmidt, H. et al. Axonal synapse sorting in medial entorhinal cortex. *Nature* **549**, 469–475 (2017).
  287. Larson, V. A. et al. Oligodendrocytes control potassium accumulation in white matter and seizure susceptibility. *Elife* **7**, 1–33 (2018).
  288. Chernoff, G. F. Shiverer: an autosomal recessive mutant mouse with myelin deficiency. *J. Hered.* **72**, 128 (1981)
  289. Battefeld, A., Klooster, J. & Kole, M. H. P. Myelinating satellite oligodendrocytes are integrated in a glial syncytium constraining neuronal high-frequency activity. *Nat. Commun.* **7**, 11298 (2016).
  290. Arvanitaki, A. Effects evoked in an axon by the activity of a contiguous one. *J. Neurophysiol.* **5**, 89–108 (1942).
  291. Katz, B. Y. B. & Schmitt, O. H. Electrical interaction between two adjacent nerve fibres. *J. Physiol.* **97**, 471–488 (1940).
  292. Anastassiou, C. A., Perin, R., Markram, H. & Koch, C. Ephaptic coupling of cortical neurons. *Nat. Neurosci.* **14**, 217–224 (2011).
  293. Han, K.-S. et al. Ephaptic Coupling Promotes Synchronous Firing of Cerebellar Purkinje Cells. *Neuron* **100**, 564–78 (2018).
  294. Anastassiou, C. A. & Koch, C. Ephaptic coupling to endogenous electric field activity: Why bother? *Curr. Opin. Neurobiol.* **31**, 95–103 (2015).
  295. Anastassiou, C. A., Perin, R., Buzsáki, G., Markram, H. & Koch, C. Cell type- and activity-dependent extracellular correlates of intracellular spiking. *J. Neurophysiol.* **114**, 608–623 (2015).
  296. Dudek, F. E., Yasumura, T. & Rash, J. E. ‘Non-synaptic’ mechanisms in seizures and epileptogenesis. *Cell Biol. Int.* **22**, 793–805 (1998).
  297. Goldwyn, J. H. & Rinzel, J. Neuronal coupling by endogenous electric fields: cable theory and applications to coincidence detector neurons in the auditory brain stem. *J. Neurophysiol.* **115**, 2033–2051 (2016).
  298. Jefferys, J. G. R., Group, N. & Kingdom, U. Nonsynaptic modulation of neuronal activity in the brain: electric currents and extracellular ions. *Physiol. Rev.* **75**, 689–723 (1995).
  299. Weiss. Field effects in the CNS play functional roles. *Front. Neural Circuits* **4**, 1–10 (2010).
  300. Binczak, S., Eilbeck, J. C. & Scott, A. C. Ephaptic coupling of myelinated nerve fibers. *Phys. D Nonlinear Phenom.* **148**, 159–174 (2001).
  301. Inan, M. & Anderson, S. A. The chandelier cell, form and function. *Curr. Opin.*

- Neurobiol.* **26**, 142–148 (2014).
302. Micu, I. et al. NMDA receptors mediate calcium accumulation in myelin during chemical ischaemia. *Nature* **439**, 988–992 (2006).
  303. Micu, I. et al. The molecular physiology of the axo-myelinic synapse. *Exp. Neurol.* **276**, 41–50 (2015).
  304. Micu, I., Plemel, J. R., Caprariello, A. V., Nave, K. A. & Stys, P. K. Axo-myelinic neurotransmission: A novel mode of cell signalling in the central nervous system. *Nat. Rev. Neurosci.* **19**, 49–57 (2018).
  305. Williamson, a. V., Mellor, J. R., Grant, a. L. & Randall, a. D. Properties of GABA(A) receptors in cultured rat oligodendrocyte progenitor cells. *Neuropharmacology* **37**, 859–873 (1998).
  306. Hamilton, N. B. et al. Endogenous GABA controls oligodendrocyte lineage cell number, myelination, and CNS internode length. *Glia* **65**, 309–321 (2017).
  307. Wake, H., Lee, P. R. & Fields, R. D. Control of local protein synthesis and initial events in myelination by action potentials. *Science* **333**, 1647–1651 (2011).
  308. Pinault, D. The thalamic reticular nucleus: Structure, function and concept. *Brain Research Reviews* **46**, (2004).
  309. Soliman, M. A., Aboharb, F., Zeltner, N. & Studer, L. Pluripotent stem cells in neuropsychiatric disorders. *Mol. Psychiatry* **22**, 1241–1249 (2017).
  310. Marissal, T. et al. Restoring wild type-like network dynamics and behaviour during adulthood in a mouse model of schizophrenia. *Nat. Neurosci.* **21**, 1412–20 (2018).
  311. Xu, B. et al. Elucidating the genetic architecture of familial schizophrenia using rare copy number variant and linkage scans. *Proc. Natl. Acad. Sci. U. S. A.* **106**, 16746–51 (2009).
  312. Xu, B. et al. De novo gene mutations highlight patterns of genetic and neural complexity in schizophrenia. *Nat. Genet.* **44**, 1365–9 (2012).
  313. Reich, D. S., Lucchinetti, C. F. & Calabresi, P. A. Multiple Sclerosis. *N. Engl. J. Med.* **378**, 169–180 (2018).
  314. Trapp, B. D. et al. Cortical neuronal densities and cerebral white matter demyelination in multiple sclerosis: a retrospective study. *Lancet Neurol.* **17**, 870–884 (2018).
  315. Rocca, M. A. et al. The hippocampus in multiple sclerosis. *Lancet Neurol.* **17**, 918–926 (2018).
  316. Di Filippo, M., Portaccio, E., Mancini, A. & Calabresi, P. Multiple sclerosis and cognition: synaptic failure and network dysfunction. *Nat. Rev. Neurosci.* **19**, 599–609 (2018).
  317. van Erp, T. G. M. et al. Subcortical brain volume abnormalities in 2028 individuals with schizophrenia and 2540 healthy controls via the ENIGMA consortium. *Mol. Psychiatry* **21**, 547–553 (2016).
  318. Nowogrodzki, A. The strongest scanners. *Nature*. **563**, 24–26 (2018).
  319. Köhler, W., Curiel, J. & Vanderver, A. Adulthood leukodystrophies. *Nat. Rev. Neurol.* **14**, 94–105 (2018).
  320. Pietersen, C. Y. et al. Molecular profiles of parvalbumin-immunoreactive neurons in the superior temporal cortex in schizophrenia. *J. Neurogenet.* **28**, 70–85 (2014).
  321. Bugiani, M., Vuong, C., Breur, M. & Knaap, M. S. Van Der. Vanishing white matter: a leukodystrophy due to astrocytic dysfunction. *Brain Pathology.* **28**, 408–421 (2018).
  322. Micheva, K. D. et al. Distinctive Structural and Molecular Features of Myelinated Inhibitory Axons in Human Neocortex. *eNeuro.* **5**, 1–12 (2018).



# Appendices



## Summary

Myelination is the insulating ensheathment of axons by oligodendrocytes to increase action potential propagation and provide metabolic support. GABAergic interneurons are a heterogeneous group of predominantly local, inhibitory cells. In schizophrenia, a major debilitating psychiatric disorder, both myelination as well as functioning of GABAergic interneurons have independently been suggested to be impaired. Whether GABAergic interneurons themselves show myelination, remains unknown. Here, we show that GABAergic myelination has been extensively observed throughout various brain areas and different species. This interneuron myelination appears highly specific for the subclass of fast-spiking, parvalbumin (PV)-expressing interneurons. Indeed, nearly every PV interneuron exhibits myelination on its proximal axons in the adult brain. Furthermore, PV interneuron myelination is dependent upon neuronal activity. Finally, axonal morphology is shown to be a major determinant for myelination of PV interneurons as well as other interneuron subclasses. Together, interneuron myelination presents a widespread novel phenomenon with interesting implications for brain functioning in health and disease.

---

## Samenvatting

Myelinisatie is de omwikkeling van axonen door oligodendrocyten met als doel actiepotentialen te versnellen en axonen te voorzien van metabole ondersteuning. GABAerge interneuronen zijn een heterogene groep van hoofzakelijk lokale, inhibitoire cellen. Er zijn verschillende aanwijzingen dat in schizofrenie, een invaliderende psychiatrische stoornis, zowel myelinisatie als het functioneren van GABAerge interneuronen zijn aangedaan. Tot op heden is het onduidelijk of GABAerge interneuronen zelf gemyeliniseerd zijn. Hier laten wij zien dat myelinisatie van GABAerge interneuronen wel degelijk veelvuldig wordt geobserveerd in verschillende hersengebieden en diersoorten. De myelinisatie van interneuronen is specifiek voor de subklasse van snel-vurende, parvalbumine-positieve (PV) interneuronen. Bijna alle PV interneuronen in het volwassen brein zijn gemyeliniseerd op het proximale deel van het axon. Tevens laten wij zien dat PV interneuron myelinisatie in het volwassen brein afhankelijk is van neuronale activiteit. Tot slot lijkt axonale morfologie een van de belangrijkste voorspellers voor myelinisatie van zowel PV interneuronen als andere interneuron subklassen. Samenvattend vormt interneuron myelinisatie een ruimschoots aanwezig, nieuw fenomeen met mogelijk interessante implicaties voor het functioneren van het brein in gezondheid en ziekte.



---

---

## **Curriculum Vitae**

Jeffrey Stedehouder was born 11 maart 1986 in Gouda, The Netherlands. He attained a BA degree in Egyptology and a BSc degree in Psychology from Leiden University in 2010, participating in the *Honours Class* as well as the *Honours Research Bachelor Project* under supervision of Prof. dr. Belle Derks. Afterwards, he attained his MSc degree in Neuroscience from the Erasmus University in 2012, during which he participated in the Exchange *Honours Master Programme* between Amsterdam and Rotterdam. From 2012 till 2018, he worked on his PhD thesis under supervision of Prof. dr. Steven Kushner at the Department of Psychiatry of the Erasmus MC in Rotterdam.

## Publications

### Present Thesis:

**Stedehouder J**, Brizee D, Slotman JA, Lehrer ML, Berson DM, Houtsmuller AB, Kushner SA. Axonal morphology governs cortical interneuron myelination. (*Manuscript under review*).

**Stedehouder J\***, Brizee D\*, Shpak G, Kushner SA. (2018). Activity-dependent myelination of parvalbumin interneurons mediated by axonal morphological plasticity. *Journal of Neuroscience*. 38(15):3631- 3642.  
Featured Article. *Journal of Neuroscience*. 38(15)

**Stedehouder J**, Couey JJ, Brizee D, Hosseini B, Slotman J, Dirven CMF, Shpak G, Houtsmuller AB, Kushner SA. (2017). Fast-spiking parvalbumin-positive interneurons are frequently myelinated in the cerebral cortex in mouse and human. *Cerebral Cortex*. 27(10):5001-5013.

**Stedehouder J**, Kushner SA. (2017). Myelination of parvalbumin interneurons. A parsimonious locus of convergence in Schizophrenia pathophysiology. *Molecular Psychiatry*. 22(1):4-12.

### Not in Thesis:

**Stedehouder J**, Mientjes E, Demmers J, Elgersma Y, Kushner SA. Laminin abnormalities in schizophrenia. (*Manuscript in preparation*).

**Stedehouder J**, Bouwen BLJ, Gao Z, Dirven CMF, Hoogendijk WJG, Kushner SA. Whole-cell electrophysiological recordings from a patient with bipolar disorder: A case study. (*Manuscript in preparation*).

Avagliano Trezza R\*, Sonzogni M\*, Bossuyt SNV\*, Izampela Zampeta F, Punt AM, Van den Berg M, Munshi ST, **Stedehouder J**, Kros JM, Williams M, Heussler H, De Vrij FMS, Mientjes E, Van Woerden GM, Kushner SA, Distel B\*, Elgersma Y\*. Angelman Syndrome-associated mutations reveal mechanism and importance of UBE3A targeting to the nucleus. (*Manuscript in revision*).

Markx S, Au E\*, Karayannis T\*, Wan Lai S\*, D'Amour J\*, Dilsiz P\*, **Stedehouder J**, Sosunov AA, Curley J, Levy R, Ellegood J, Stark K, Diamantopoulou A, Soldan SS, Purpura M, Benzer C, Jacobs LM, Goldman J, Dwork AJ, Strauss KA, Ananth M, Robison L, Peles E, Cherry SR, Henkelman M, Thanos PK, Winawer M, Lai W-S, Aoki C, Gan W, Fishell G, Froemke, Kushner SA, Talos DM, Karayiougou M, Gogos JA. Inhibition of overactive mTOR ameliorates core deficits in a mouse model of CNTNAP2-associated autism. (*Manuscript under review*).

---

Amin N, De Vrij F, Baghdadi M, Brouwer R, Van Rooij J, Jovanova O, Uitterlinden A, Hofman A, Janssen H, Darwish Murad S, Kraaij R, **Stedehouder J**, Van Den Hout MC, Kros LM, Van IJcken WF, Tiemeijer H, Kushner SA, Van Duijn, CM. (2018). A rare missense variant in RCL1 segregates with depression in extended families. *Molecular Psychiatry*. 23(5):1120-26.

Cover Image. *Molecular Psychiatry*. 23(5):1093

Schreiber J\*, Grimbergen L-A\*, Overwater I, Van der Vaart T, **Stedehouder J**, Schuhmacher AJ, Guerra C, Kushner SA, Jaarsma D, Elgersma Y. (2017). Mechanisms underlying cognitive deficits in a mouse model for Costello Syndrome are distinct from other RASopathy mouse models. *Scientific Reports*. 7(1):1256

Peter S\*, Ten Brinke MM\*, **Stedehouder J**, Reinelt CM, Wu B, Zhou, H, Zhou K, Boele HJ, Kushner SA, Lee, MG, Schmeisser, MJ, Boeckers, TM, Schonewille M, Hoebeek FE, De Zeeuw CI. (2016). Dysfunctional cerebellar Purkinje cells contribute to autism-like behaviour in Shank2-deficient mice. *Nature Communications*. 1(7):12627.

Derks B, **Stedehouder J**, Ito T. (2015). Social identity modifies face perception: An ERP study of social categorization. *Social, Affective, Cognitive Neuroscience*, 10(5):672-9.

\* These authors contributed equally

